PREDICTING SIZE EFFECTS AND DETERMINING LENGTH SCALES IN SMALL SCALE METALLIC VOLUMES

A Thesis

by

ABU NAYEEM MD. FARUK

Submitted to the Office of Graduate Studies of
Texas A&M University
in partial fulfillment of the requirements for the degree of

MASTER OF SCIENCE

May 2010

Major Subject: Civil Engineering

Predicting Size Effects and Determining Length Scales in Small Scale Metallic Volumes

PREDICTING SIZE EFFECTS AND DETERMINING LENGTH SCALES IN SMALL SCALE METALLIC VOLUMES

A Thesis

by

ABU NAYEEM MD. FARUK

Submitted to the Office of Graduate Studies of
Texas A&M University
in partial fulfillment of the requirements for the degree of

MASTER OF SCIENCE

Approved by:

Chair of Committee,	Rashid K. Abu Al-Rub
Committee Members,	Xin-Lin Gao
	Eyad Masad
Head of Department,	John Niedzwecki

May 2010

Major Subject: Civil Engineering

ABSTRACT

Predicting Size Effects and Determining Length Scales in Small Scale Metallic Volumes.

(May 2010)

Abu Nayeem Md. Faruk, B.Sc., Bangladesh University of Engineering & Technology

Chair of Advisory Committee: Dr. Rashid K. Abu Al-Rub

The purpose of this study is to develop an understanding of the behavior of metallic structures in small scales. Structural materials display strong size dependence, when deformed non-uniformly, into the inelastic range. This phenomenon is widely known as size effect. The primary focus of this study is on developing analytical models that predict some of the most commonly observed size effects in structural metals and validating them by comparing them with experimental results. A nonlocal, rate-dependent and gradient-dependent theory of plasticity on a thermodynamically consistent framework is adopted for this purpose.

The developed gradient plasticity theory is applied to study size effects observed in biaxial and thermal loading of thin films and indentation tests. One important intrinsic material property associated with this study is material length scale. The work also presents models for predicting length scales and discusses their physical interpretations. It is found that the proposed theory is successful for the interpretation of indentation size effects in micro/nano-hardness when using pyramidal or spherical indenters and gives sound interpretation of the size effects in thin films under biaxial or thermal loading.

ACKNOWLEDGEMENTS

I would like to thank my advisor, Dr. Rashid K. Abu Al-Rub, for the consistent guidance and support that he has given me throughout the course of this research. I would also like to thank my committee members, Dr. Gao and Dr. Masad, for they have been kind enough to be a part of this work.

Thanks also go to my friends and colleagues, and the faculty and staff of the department of Civil Engineering for making my time at Texas A&M University a great experience.

Finally, thanks to my mother and father for their encouragement and to my wife for her patience and love.

I also gratefully acknowledge the financial support of this study jointly provided by U.S. National Science Foundation and the U.S. Department of Energy (NSF#0728032).

TABLE OF CONTENTS

CHAPTER Page

LIST OF FIGURES

FIGURE Page

FIGURE Page

LIST OF TABLES

CHAPTER I

INTRODUCTION

1.1 Problem Statement: Size Effects and Material Length Scales

With the emerging area of nanotechnology in recent years, there have been significant and rapidly growing efforts to fabricate small structures in the micro- and nano-meter scales. Along with it came the challenge of evaluating the mechanical behaviors of materials at these small scales. Experiments have shown that the properties and behavior of matter at the meso- ($\approx 10^{-4} - 10^{-3}$ meters), micro- ($\approx 10^{-7} - 10^{-4}$ meters) and nano- ($\approx 10^{-10} - 10^{-7}$ meters) scales, cannot necessarily be predicted from those observed at larger (macro, i.e. larger than 10^{-3} meters) or smaller (atomic, i.e. smaller than 10^{-10} meters) scales. Instead, they exhibit important differences that cannot be explained by traditional models and theories. The dependence of material mechanical properties on the size of the structure is termed as *size scale effects* or more commonly *size effects*.

Several cases of size effects have been observed in experiments. Indentation of thin films shows an increase in the strength with decreasing the film thickness (Huber et al., 2002). Experimental works of Stolken and Evans (1998) has shown that the scaled bending strength in micro-bending of thin nickel films increases significantly as the film thickness decrease. Similarly, experimental work on particle-reinforced composites has

---

This thesis follows the style of International Journal of Plasticity.

revealed that a substantial increase in the macroscopic strength can be achieved by decreasing the particle size while keeping the volume fraction constant (Lloyd, 1994; Rhee et al., 1994a, 1994b; Zhu and Zbib, 1995; Nan and Clarke, 1996; Kiser et al., 1996; Zhu et al., 1997). But probably the most important of these is the so called *indentation size effect (ISE)*: the increase in hardness with decreased indentation size in micro and nano-indentation tests (e.g. Stelmashenko et al., 1993; Ma and Clarke, 1995; McElhaney et al.,1998; Lim and Chaudhri, 1999; Elmustafa and Stone, 2002; Swadener et al., 2002; Huber et al., 2002; Abu Al-Rub and Voyiadjis, 2004a).

These experiments have thus shown increase in strength with decrease in size at various length scales. The material mechanical properties, such as flow stress or hardness, in metallic materials whether in simple tension, torsion, bending, or indentation testing are thus size dependent. In all of these cases, the representative length scale of the deformation field sets the qualitative and quantitative behavior of size effects. The classical continuum plasticity and damage theories, as well as any theory in which the material behavior is fully characterized in terms of stresses and strains (without reference to any characteristic length scale), cannot predict the size effects since they do not possess an intrinsic material length-scale in their governing equations (i.e. material parameter with length dimension). On the other hand, it is still not possible to perform quantum and atomistic simulations on realistic time scale and structures. A multi-scale continuum theory, therefore, is needed to bridge the gap between the classical continuum theories and atomistic simulations.

The objective of the current work, therefore, is to develop analytical models to predict some of the most commonly encountered cases of size scale effects. The cases considered here are, biaxial and thermal loading of thin films on substrates, micro and nano-indentations on metallic structures by conical or pyramidal indenters and micro and nano-indentations on metallic structures by spherical indenters. Furthermore, as a subsequent development of the indentation size effect models, a way to determine the material length scale is discussed and its physical interpretation is sought.

1.2 Literature Review: Gradient Plasticity Theories

Size dependence of the material mechanical properties has largely been linked with the increase in higher-order strain gradients inherent in highly non-uniform (localized) zones of deformation by a number of authors in recent years (e.g. Stelmashenko et al., 1993; Fleck et al., 1994; Ma and Clarke, 1995; Arsenlis and Parks, 1999; Busso et al., 2000; Gao and Huang, 2003). For example the material deformation in crystalline materials enhances the dislocation formation, the dislocation motion, and the dislocation storage. The dislocation storage causes material hardening. The stored dislocations generated by trapping each other in a random way are referred to as *statistically-stored dislocations* (SSDs), while the stored dislocations that relieve the plastic deformation incompatibilities within the polycrystalline caused by non-uniform dislocation slip are called *geometrically-necessary dislocations* (GNDs). Their presence causes additional storage of defects and increases the deformation resistance by acting as obstacles to the SSDs (Gao et al., 1999). SSDs are believed to be dependent on the effective plastic strain, while the density of GNDs is directly proportional to the gradient

of the effective plastic strain (Kroner, 1962; Ashby, 1970; Arsenlis and Parks, 1999). Accordingly, the theories of strain gradient plasticity have been proposed based on the concept of geometrically necessary dislocations in order to characterize the size effects.

Inspired by the size effects problem in various metallic and non-metallic materials and the loss of well-posedness of the governing equations in the softening media, a number of gradient-enhanced theories have been proposed to address these problems through the incorporation of intrinsic length-scale measures in the constitutive equations, mostly based on continuum mechanics concepts. Gradient approaches typically retain terms in the constitutive equations of higher-order gradients with coefficients that represent length-scale measures of the deformation microstructure associated with the nonlocal continuum. These length-scale parameters are material properties that derive qualitatively and quantitatively the size effects. Moreover, the incorporation of these material length-scale parameters is necessary to preserve the well-posedness of the constitutive relations in softening media.

Aifantis (1984) was one of the first to study the gradient regularization in solid mechanics. However, the gradient theory of Aifantis (1984) is motivated by localization of softening and its principal aim was to achieve objectivity of continuum modeling and numerical simulations. Other researchers have contributed substantially to the gradient approach with emphasis on numerical aspects of the theory and its implementation in finite element codes: Lasry and Belytschko (1988), Zbib and Aifantis (1992); and de Borst and coworkers. In addition, we should include here the recent works of Oka et al. (2000), Aifantis (1999), Wang et al. (1998); Askes and Sluys (2002), Geers et al. (2000),

and Svedberg and Runesson (2000) etc. Gradient thermodynamic damage models were also introduced by Fremond and Nedjar (1996), Voyiadjis et al. (2001) and Voyiadjis and Dorgan (2001). Moreover, interesting contributions on the physical origin of the length scale in gradient plasticity theories have been made by Voyiadjis and Abu Al-Rub (2002), Abu Al- Rub and Voyiadjis (2004a), Abu Al-Rub (2007) and Abu Al-Rub and Faruk (2010).

The gradient terms in several plasticity models are introduced through the yield function (e.g. Mühlhaus and Aifantis, 1991; de Borst and Mühlhaus, 1992; Gao et al., 1999; Chen and Wang, 2002; Gao, 2003 and Gao, 2008). The gradient concept is also extended to the gradient damage theory that has been developed for isotropic damage (e.g. Peerlings et al., 1996) and for anisotropic damage (e.g. Kuhl et al., 2000; Voyiadjis et al., 2001; Voyiadjis and Dorgan, 2001). In addition, extension of the gradient theory to rate-dependent plasticity/damage has been recently addressed by few authors (Wang et al., 1998; Aifantis et al., 1999; Oka et al., 2000; Gurtin, 2002, 2003; Saczuk et al., 2003).

In parallel, other approaches that have length-scale parameters in their constitutive structure (commonly referred to as nonlocal theories) have appeared in the literature as an outgrowth of earlier work by Eringen (e.g. Eringen and Edelen, 1972) and Bazant (e.g. Pijaudier-Cabot and Bazant, 1987; Bazant and Pijaudier-Cabot, 1988). Nonlocal models also abandon the assumption that the stress at a given point is uniquely determined by the history of strain and temperature at this point only. They take into account possible interactions with other material points in the vicinity of that point.

Theoretically, the stress at a point can depend on the strain history in the entire body, but the long-range interactions certainly diminish with increasing distance, and can be neglected when the distance exceeds the length of interaction.

All the theories mentioned so far include in their structure explicit material length scale measures. However, incorporation of rate-dependent viscous terms (e.g. Needleman, 1988; Wang et al., 1996) introduces an implicit length scale measure and limits localization in dynamic or quasi-static problems. The gradient-dependent theories have given reasonable agreement with the size dependence encountered in composite material experiments (e.g. Shu and Fleck, 1999; Shu and Barrlow, 2000; Busso et al., 2000; Bassani, 2001; Xue et al., 2002a, Gao, 2003 and Gao, 2008), micro- and nano-indentation experiments (e.g. Nix and Gao, 1998; Shu and Fleck, 1998;; Gao et al., 1999; Huang et al., 2006; Abu Al-Rub, 2007 and Abu Al-Rub and Faruk, 2010), as well as with the micro-bend and micro-twist experiments (Gao et al., 1999; Aifantis, 1999; Tsagrakis and Aifantis, 2002). In this thesis a thermodynamically consistent gradient-dependent plastic theory suitable for describing the size effects problems in the meso-, micro- and nano-scale systems will be formulated.

1.3 Objectives

The objective of this study is to develop analytical models to predict some of the most commonly encountered cases of size scale effects and to evaluate material length scale parameter. The steps involved include:

- Developing a thermodynamically sound strain-gradient plasticity model based on non-local theories.

- Developing analytical model to predict size effects on biaxially loaded elasto-plastic thin film on elastic substrate.
- Developing analytical model to predict size effects on thermally loaded thin film on substrate.
- Developing analytical model to predict indentation size effects for indentation by conical/pyramidal indenters and comparing with experimental results.
- Developing analytical model to predict indentation size effects for indentation by spherical indenters comparing with experimental results.
- Developing analytical model to determine material intrinsic length scale parameters through indentation tests using both conical and spherical indenters and determining the correlation between the two models.

1.4 Organization of the Thesis

The rest of the thesis is organized as follows:

In Chapter II, the thermodynamic framework of the strain gradient plasticity model is developed in order to formulate the nonlocal yield condition and the higher order boundary conditions. Effects of interfacial yield strength and interfacial hardening is incorporated through the boundary conditions.

In Chapter III, the proposed gradient plasticity theory is used to investigate the size effect problems in question. In case of size effect in thin film, the yield conditions along with some basic laws of mechanics e.g. Hook's law and laws of equilibrium is used to formulate the second order differential equation. This is solved along with the non local boundary conditions to obtain the analytical model for predicting size effect.

In Chapter IV, definitions of SSD and GND densities are used to develop the indentation size effect models. One key idea that comes into play here is the nonlinear coupling between the SSDs and GNDs that eventually allows the model to simultaneously predict ISE from both micro and nano-indentations tests. As a subsequent development of the ISE model, a framework to evaluate the material intrinsic length scale is developed for both the cases of conical and spherical indenters. The physical nature of the length scale parameter is identified and a correlation between the length scale determined from a conical indentation test and that from a spherical indentation test is developed. Experimental data form indentation tests on a wide range of metallic materials using both conical and spherical indenters are analyzed using the developed models. Already existing models are also used on the same data to compare with the proposed model. Length scale parameters are calculated in each case.

Chapter V summarizes the conclusions of this work.

CHAPTER II

A HIGHER-ORDER STRAIN GRADIENT PLASTICITY THEORY BASED ON THERMODYNAMICS

2.1 Introduction

While attempting to develop theoretical understanding of the widely observed size effect phenomena, it became clear over the last three decades that the classical plasticity and damage theories are not well equipped. These conventional or classical theories generally assume that the stress at a point is a function of strain at that point only. However, when inhomogeneities are present and the gradients in strain become significant, this localization assumption is no longer valid. Therefore, continuum plasticity and damage theories that take into account the influence of the n^{th} nearest neighbor of the material points or the long-range micro structural interactions should be developed.

In this chapter, a physically motivated and thermodynamically consistent formulation of higher order gradient plasticity theory is presented. This proposed model is a non-local parameter framework that takes into consideration the presence of gradients of effective (or equivalent) plastic strain which is motivated by the accumulation of geometrically necessary dislocations and, hence, incorporates additional isotropic hardening. It is demonstrated that, the non-local yield condition and the higher order boundary conditions can be directly derived from the laws of thermodynamics. The following sections present the principal of virtual power and the fundamental

statements of irreversible thermodynamics that are commonly used in the mathematical modeling of the material mechanical behavior.

2.2 Thermodynamics of Higher-Order Gradient Plasticity

The classical theory of isotropic solids undergoing small deformation is based on the additive decomposition of the total strain rate, $\dot{\boldsymbol{\varepsilon}}$ into an elastic part, $\dot{\boldsymbol{\varepsilon}}^{\mathbf{e}}$ and a plastic part, $\dot{\boldsymbol{\varepsilon}}^{\mathbf{p}}$ such that,

$$\dot{\varepsilon}_{ij} = \dot{\varepsilon}^{e}_{ij} + \dot{\varepsilon}^{p}_{ij}, \qquad \dot{\varepsilon}^{p}_{kk} = 0 \tag{2.1}$$

where the rate of local effective plastic strain, $\dot{\varepsilon}^{p}$ is defined as,

$$\dot{\varepsilon}^{p} = \left\| \dot{\varepsilon}^{p}_{ij} \right\| = \sqrt{\frac{2}{3} \dot{\varepsilon}^{p}_{ij} \dot{\varepsilon}^{p}_{ij}} \tag{2.2}$$

The unit direction of plastic strain tensor, $\mathbf{N}$, is defined as follows:

$$N_{ij} = \frac{\dot{\varepsilon}^{p}_{ij}}{\left\| \dot{\varepsilon}^{p}_{ij} \right\|} = \frac{\dot{\varepsilon}^{p}_{ij}}{\dot{\varepsilon}^{p}} \qquad \Rightarrow \dot{\varepsilon}^{p}_{ij} = \dot{\varepsilon}^{p} N_{ij} \tag{2.3}$$

2.2.1 Principle of virtual power

The principle of virtual power asserts that, given any sub-body Γ, the virtual power expended on Γ by materials or bodies exterior to Γ (i.e. external power) be equal to the virtual power expended within Γ (i.e. internal power), such that

$$\mathrm{P}_{\mathrm{ext}} = \mathrm{P}_{\mathrm{int}} \tag{2.4}$$

Let **n** denote the outward unit normal to $\partial\Gamma$. The external expenditure of power is assumed to arise from a macroscopic surface traction t and the scalar microtraction force, q conjugate to the local effective plastic strain rate $\dot{\varepsilon}^{p}$, defined for each unit

vector **n** normal to the boundary $\partial\Gamma$ of Γ. Therefore, by neglecting body forces, one can write the external virtual power in the following form:

$$\mathrm{P}_{\mathrm{ext}} = \int_{\partial\Gamma} \left(t_i v_i + q\dot{\varepsilon}^p \right) dA \tag{2.5}$$

The kinematic fields $\mathbf{v}$ and $\dot{\varepsilon}^p$ are considered here as virtual, where $\mathbf{v}$ is the velocity vector and q is the microtraction force. The two integral terms in Eq. (2.5) constitute the macroscopic and the microscopic power expenditures respectively. Moreover, since plastic deformation, accommodated by dislocation generation and motion, is affected by interfaces, the last integral term result in higher order boundary conditions generally consistent with the framework of a gradient type theory. these extra boundary conditions need to be imposed at external and internal boundary surfaces or interfaces separating different constituents as is shown later in this chapter.

The external power is balanced by an internal expenditure of power characterized by the Cauchy stress tensor $\boldsymbol{\sigma}$ defined over Γ and the drag-stress R conjugate to ε^p and associated with isotropic hardening. However, to incorporate the gradients of the plastic strain, power expenditures associated with kinematic variables $\nabla_k \varepsilon^p$ are also considered. Therefore, it can be assumed that additional power is expended internally by the higher order microforce vector Q_k conjugate to $\nabla_k \varepsilon^p$. Specifically, the internal virtual power is assumed to have the following form:

$$\mathrm{P}_{\mathrm{int}} = \int_{\Gamma} \left(\sigma_{ij} \dot{\varepsilon}^e_{ij} + R\dot{\varepsilon}^p + Q_k \nabla_k \dot{\varepsilon}^p \right) dV \tag{2.6}$$

The first two terms in Eq. (2.6) constitutes the definition of the local internal virtual power in the mathematical definition of standard plasticity theory. The second term in

Eq. (2.6) represents the internal power generated by the drag-stress R which causes isotropic hardening. The last term is meant to take into account the large spatial variations in plastic strains at small length scales. It represents the internal power generated by the non-local drag vector Q which is meant to account for the additional isotropic hardening from the accumulation of GNDs. Thus, the expression for internal power is based on the concept that the power expended by each kinematical field be expressible in terms of an associated fore system consistent with its own balance.

Now, using Eq. (2.1) in Eq. (2.6) and rearranging one gets,

$$\mathrm{P}_{\mathrm{int}} = \int_{\Gamma} \left(\sigma_{ij} \dot{\varepsilon}_{ij} - s_{ij} \dot{\varepsilon}_{ij}^{p} + R \dot{\varepsilon}^{p} + Q_k \nabla_k \dot{\varepsilon}^{p} \right) dV \tag{2.7}$$

where $s_{ij} = \sigma_{ij} - \frac{1}{3} \sigma_{kk} \delta_{ij}$ is the deviatoric part of the Cauchy stress tensor and due to plastic incompressibility, $\sigma_{ij} \dot{\varepsilon}_{ij}^{p} = s_{ij} \dot{\varepsilon}_{ij}^{p}$.

One can apply the divergence theorem to obtain the following expressions:

$$\begin{aligned} \int_{\Gamma} \sigma_{ij} \dot{\varepsilon}_{ij} dV &= \int_{\partial\Gamma} \sigma_{ij} v_i n_j dA - \int_{\Gamma} \sigma_{ij,j} v_i dV \\ \text{and} \quad \int_{\Gamma} Q_k \nabla \dot{\varepsilon}^{p} dV &= \int_{\partial\Gamma} Q_k \dot{\varepsilon}^{p} n_k dA - \int_{\Gamma} Q_{k,k} \dot{\varepsilon}^{p} dV \end{aligned} \tag{2.8}$$

Substituting the above equations into Eq. (2.7) gives:

$$\mathrm{P}_{\mathrm{int}} = -\int_{\Gamma} \sigma_{ij,j} v_i dV - \int_{\Gamma} \left[s_{ij} \dot{\varepsilon}_{ij}^{p} - \left(R - Q_{k,k} \right) \dot{\varepsilon}^{p} \right] dV + \int_{\partial\Gamma} \sigma_{ij} n_j v_i dA + \int_{\partial\Gamma} Q_k \dot{\varepsilon}^{p} n_k dA \tag{2.9}$$

Substituting Eqs. (2.5) and (2.9) into Eq. (2.4) along with Eq. (2.3) and rearranging one gets,

$$\begin{aligned} \int_{\Gamma} \sigma_{ij,j} v_i dV + \int_{\partial\Gamma} \left(t_i - \sigma_{ij} n_j \right) v_i dA + \int_{\Gamma} \left[s_{ij} - \left(R - Q_{k,k} \right) N_{ij} \right] \dot{\varepsilon}_{ij}^{p} dV \\ + \int_{\partial\Gamma} \left(q - Q_k n_k \right) \dot{\varepsilon}^{p} dA = 0 \end{aligned} \tag{2.10}$$

The fields Γ, $\mathbf{v}$ and $\dot{\varepsilon}^p$ can be arbitrarily specified if and only if the following four conditions are satisfied:

$$\sigma_{ij,j} = 0 \tag{2.11}$$

$$t_i = \sigma_{ij} n_j \tag{2.12}$$

$$s_{ij} - \left(R - Q_{k,k}\right) N_{ij} = 0 \tag{2.13}$$

$$q = Q_k n_k \tag{2.14}$$

Eq. (2.11) is the macro-force equilibrium equation. It expresses the local static or dynamic equilibrium or the macroforce balance according to the notion of Gurtin (2003). Eq. (2.12) defines the stress vector as the surface density of the forces introduced. It also provides the local macrotraction boundary conditions on forces if the axiom of equilibrium of virtual power is applied to the whole region under consideration as opposed to arbitrarily sub-regions. Eq. (2.13) is the nonlocal microforce balance and Eq. (2.14) is the micro-traction boundary condition. However, one can view the microforce balance in Eq. (2.13) as the plasticity non-local yield condition, which is demonstrated in the next section, and the microtraction condition in Eq. (2.14) as a higher-order boundary condition (or internal boundary condition) augmented by the interaction of dislocations across interfaces (Gurtin, 2003; Gudmundson, 2004).

2.2.2 Non-local yield criterion

In the following it will be shown that the microforce balance presented in Eq. (2.13) is nothing more than the non-local yield condition. By taking the Euclidean norm of Eq. (2.13), one can write,

$$\left\|s_{ij}\right\| - \left\|R - Q_{k,k}\right\| \left\|N_{ij}\right\| = 0 \tag{2.15}$$

where $\mathbf{N}$ is collinear with $\mathbf{s}$. Moreover, since $\left\|R - Q_{k,k}\right\| = R - Q_{k,k}$ and $\left\|N_{ij}\right\| = 1$, one can then rewrite the above expression as the non-local yield criterion or the non-local plasticity loading surface f such that,

$$f = \left\|s_{ij}\right\| - \left(R - Q_{k,k}\right) = 0 \tag{2.16}$$

It is obvious that Eq. (2.16) represents a sphere in deviatoric stress-space of radius R - div$\mathbf{Q}$. One can also notice that the microstress div$\mathbf{Q}$ is giving rise to additional isotropic hardening. Since Eq. (2.16) implies that $\mathbf{N}$ is parallel to $\mathbf{s}$, one can, therefore, express the direction of plastic strain, $\mathbf{N}$, as follows:

$$N_{ij} = \frac{s_{ij}}{\left\|s_{mn}\right\|} \tag{2.17}$$

Or equivalently, from Eqs. (2.16) and (2.17),

$$N_{ij} = \frac{s_{ij}}{R - Q_{k,k}} \tag{2.18}$$

One can therefore express the plasticity flow rule, Eq. $(2.3)_2$ as follows:

$$\dot{\varepsilon}_{ij}^{p} = \dot{\varepsilon}^{p} \frac{s_{ij}}{\left\|s_{mn}\right\|} = \dot{\varepsilon}^{p} \frac{s_{ij}}{R - Q_{k,k}} \tag{2.19}$$

Therefore, one can easily proof that the plasticity flow rule can be written as,

$$\dot{\varepsilon}_{ij}^{p} = \dot{\varepsilon}^{p} \frac{\partial f}{\partial \sigma_{ij}} \tag{2.20}$$

Such that,

$$N_{ij} = \frac{\partial f}{\partial \sigma_{ij}} \tag{2.21}$$

Therefore, the flow rule in Eq. (2.20) asserts that the flow direction $\mathbf{N}$ in Eq. (2.21) is normal to the yield surface and directed outward from the yield surface. Moreover, if the higher-order gradients are neglected, one can easily retrieve from Eqs. (2.16), (2.20) and (2.21), respectively, the classical yield criterion, flow rule, and flow direction.

2.2.3 Non-local Clausius-Duhem in-equality

Utilizing the derived microforce balance, Eq. (2.13) into Eq. (2.9), one can rewrite the expression of the internal power defined in Eq. (2.7) as follows:

$$\mathrm{P}_{\mathrm{int}} = \int_{\Gamma} \sigma_{ij} \dot{\varepsilon}_{ij} dV + \int_{\partial\Gamma} Q_k \dot{\varepsilon}^p n_k dA \tag{2.22}$$

Comparing the above equation with its corresponding local expression $\mathrm{P}_{\mathrm{int}} = \int_{\Gamma} \sigma_{ij} \dot{\varepsilon}_{ij} dV$ (Green and Naghdi, 1971), implies that the long-range (non-local) energy interactions can be of non-vanishing within the plastic zone, which is represented by the second term in Eq. (2.22). Hence, according to the notion of Eringen and Edelen (1972), the energy term $\int_{\partial\Gamma} q\dot{\varepsilon}^p dA$ is called the *non-locality energy residual* that results from micro-structural interactions between the material points in the active plastic zone and at interfaces. Therefore, one can define the density of the non-locality energy residual, $\mathbb{R}$, as follows:

$$\int_{\Gamma} \mathbb{R} dV = \int_{\partial\Gamma} Q_k \dot{\varepsilon}^p n_k dA \tag{2.23}$$

This, after the use of the divergence theorem, yields,

$$\mathbb{R} = \left[Q_k \varepsilon^p \right]_{,k} \tag{2.24}$$

Assuming isothermal conditions, a purely mechanical theory can be considered based on the requirement that the rate of change in the total free energy should be less than or equal to the power done by external forces (Gurtin, 2000). If one denotes $\rho\Psi$ as the specific free energy, this requirement takes the form of a free energy inequality

$$\int_{\Gamma} \rho\Psi dV \leq \mathrm{P}_{\mathrm{ext}} \tag{2.25}$$

where, Ψ is the Helmholtz free energy. By substituting Eqs. (2.22) and (2.23) into Eq. (2.25) along with the $\mathrm{P}_{\mathrm{ext}} = \mathrm{P}_{\mathrm{int}}$, the following thermodynamic restriction can be obtained in a point wise form:

$$\sigma_{ij}\dot{\varepsilon}_{ij} - \rho\dot{\Psi} + \mathbb{R} \geq 0 \tag{2.26}$$

The inequality in Eq. (2.26) is termed here as the non-local Clausius–Duhem inequality differing from its classical counterpart only in the presence of $\mathbb{R}$. This inequality holds everywhere in Γ, but $\mathbb{R} = 0$ at material points in the elastic zone. Moreover, it can be noted from Eq. (2.24) that for a homogeneous plastic strain distribution $\mathbb{R} = 0$, one retains the classical Clausius–Duhem inequality.

2.2.4 Non-local state variables

The hardening in plasticity is introduced as hidden independent internal state variables in the thermodynamic state potential. The Helmholtz free energy is considered as the thermodynamic state potential depending on both observable and internal state variables. However, before giving its definition, a choice must be made with respect to

the nature of the state variables. Here, a form of this potential is chosen such that it depends on local variables, i.e. elastic strain, $\boldsymbol{\varepsilon}^e$ and the effect plastic strain ε^p and non-local state variable i.e. the gradient of the effective plastic strain $\nabla_k \varepsilon^p$. The Helmholtz free energy, therefore, can be expressed as:

$$\Psi = \Psi\left(\varepsilon_{ij}^e, \varepsilon^p, \nabla_k \varepsilon^p\right) \tag{2.27}$$

Assuming a separable material, i.e. no coupling between the elastic and plastic free energies (Gurtin, 2003), one can rewrite the Helmholtz free energy potential as,

$$\Psi = \Psi^e\left(\varepsilon_{ij}^e\right) + \Psi^p\left(\varepsilon^p, \nabla_k \varepsilon^p\right) \tag{2.28}$$

From Eq. (2.28), taking a time derivative of Ψ with respect to its internal state variables yields,

$$\dot{\Psi} = \frac{\partial \Psi^e}{\partial \varepsilon_{ij}^e}\dot{\varepsilon}_{ij}^e + \frac{\partial \Psi^p}{\partial \varepsilon^p}\dot{\varepsilon}_e^p + \frac{\partial \Psi^p}{\partial \nabla_k \varepsilon^p}\nabla_k \dot{\varepsilon}^p \tag{2.29}$$

The above equation can now be used into the nonlocal Clausius–Duhem inequality, Eq. (2.26) along with Eq. (2.3) such that,

$$\left(\sigma_{ij} - \rho\frac{\partial \Psi^e}{\partial \varepsilon_{ij}^e}\right)\dot{\varepsilon}_{ij}^e + \left(s_{ij} - \rho\frac{\partial \Psi^p}{\partial \varepsilon^p}N_{ij}\right)\dot{\varepsilon}_{ij}^p - \rho\frac{\partial \Psi^p}{\partial \nabla_k \varepsilon^p}N_{ij}\dot{\varepsilon}_{ij,k}^p + \mathbb{R} \geq 0 \tag{2.30}$$

Following thermodynamic state laws are obtained from the above inequality:

$$\sigma_{ij} = \rho\frac{\partial \Psi^e}{\partial \varepsilon_{ij}^e} \tag{2.31}$$

$$R = \sigma_y + \rho\frac{\partial \Psi^p}{\partial \varepsilon^p} \tag{2.32}$$

$$\text{And,} \quad Q_k = \rho \frac{\partial \Psi^p}{\partial \nabla_k \varepsilon^p} \tag{2.33}$$

where, σ_y is the initial yield strength.

In order to develop equations amenable to the analysis and computation, a simple example for the definition of the Helmholtz free energy function is considered here. Assuming decoupling between the elastic behavior and plasticity hardening (i.e. separable material) such that both Ψ^e and Ψ^p that appear in Equation (2.28) can be assumed to have, respectively, the following quadratic analytical forms:

$$\rho \Psi^e = \frac{1}{2} \varepsilon_{ij}^e E_{ijkl} \varepsilon_{kl}^e \tag{2.34}$$

$$\text{And,} \quad \rho \Psi^p = \frac{1}{2} a_1 \varepsilon^p \varepsilon^p + \frac{1}{2} a_2 \nabla_k \varepsilon^p \nabla_k \varepsilon^p \tag{2.35}$$

where, $\boldsymbol{E}$ is the symmetric fourth-order elastic stiffness tensor and a_1, a_2 are material constants. Eq. (2.31) along with Eq. (2.34) defines the Cauchy stress tensor as,

$$\sigma_{ij} = E_{ijkl} \varepsilon_{kl}^e = E_{ijkl} \left(\varepsilon_{kl} - \varepsilon_{kl}^p \right) \tag{2.36}$$

Whereas, Eqs. (2.32) and (2.33) along with Eq. (2.35) defines, respectively, the local and non-local conjugate forces as,

$$R = \sigma_y + h \varepsilon^p \tag{2.37}$$

$$Q_k = h \ell^2 \nabla_k \varepsilon^p \tag{2.38}$$

The material constants, a_1 and a_2 are favorably replaced by h and $h\ell^2$ respectively with h being the constant hardening modulus and ℓ being the material length scale parameter. Eq. (2.38) upon taking gradient yields,

$$Q_{k,k} = h\ell^2 \nabla^2 \varepsilon^p \tag{2.39}$$

where ∇^2 is the Laplacian operator. Therefore, the yield condition in Eq. (2.16) becomes,

$$\sqrt{\frac{3}{2} s_{ij} s_{ij}} - \left(\sigma_y + h\varepsilon^p\right) + h\ell^2 \nabla^2 \varepsilon^p = 0 \tag{2.40}$$

The modulus of the deviatoric part of the Cauchy stress tensor is defined here as $\sqrt{\frac{3}{2} s_{ij} s_{ij}}$ in case of Von-Mises type plasticity and can be set equal to the effective (or equivalent) stress. Aifantis (1984) presented the above yield condition as,

$$\sigma_e = \sigma_e^H - h\ell^2 \nabla^2 \varepsilon^p \tag{2.41}$$

where, σ_e and σ_e^H are the total and the homogeneous part of the effective stress.

2.2.5 Interfacial effects and higher order boundary conditions

It has already been discussed that the plastic deformation is mainly carried by dislocations within the bulk. These dislocations can move through the crystal grains and can interact with each other. Interfaces often hinder their transmission, creating a dislocation pile-up at the interface and thereby making the material harder to deform.

The effect of interfaces on plastic deformation is incorporated in the presented higher order gradient plasticity framework by relating the microtraction boundary condition in Eq. (2.14) with an interfacial energy term. This interfacial energy introduces a resistance against dislocation emission/transmission and is significant in small-scale systems (e.g. thin films, nano-wires, nano-composites, nano-crystalline material) when the surface-to-volume ratio becomes large enough. In Eq. (2.14), the microtraction stress

q is meant to be the driving force at the material internal and external boundaries, which can be interpreted as the interfacial stress at free surface or interface which is conjugate to the surface plastic strain. Therefore, q can be related to the interfacial energy φ per unit surface area by using the well-known relation (Gurtin and Murdoch, 1978):

$$q = \frac{\partial \varphi}{\partial \varepsilon^{p(I)}} = h\ell^2 \nabla_k \varepsilon^{p(I)} n_k \quad \text{On } \partial\Gamma^p \tag{2.42}$$

where, $\varepsilon^{p(I)}$ is the plastic strain at the interface and $\partial\Gamma^p$ is the plastic interface. Continuity of the strain field requires that, $\varepsilon^p\big|_{\partial\Gamma^p} = \varepsilon^{p(I)}$ at the interface. Therefore, $\varepsilon^{p(I)}$ and the bulk effective plastic strain ε^p are identical at the interface. However, it may be argued that the plastic strain should vanish at an elastic–plastic boundary. As explained in Fredriksson and Gudmundson (2007), the interfacial region has a finite but small thickness such that the plastic strain varies within this thickness and vanishes at the border between the interfacial region and the elastic material. However, if the thickness of the interfacial region is neglected, then the interface can be modeled as a mathematical surface where jumps in the plastic strain are allowed.

According to the definition in Eq. (2.42), $\varphi = 0$ designates a free surface where dislocations are allowed to escape, while $\varphi \to \infty$ designates a micro-clamped surface (i.e. rigid interface) where dislocations are not allowed to penetrate. Hence, constrained plastic flow could be modeled either as a full constraint, i.e. $\varepsilon^p = 0$ (when $\varphi \to \infty$), or no constraint, i.e. $q = 0$ (when $\varphi \to 0$). However, following the ideas presented by Gudmundson (2004), Fredriksson and Gudmundson (2005, 2007), Aifantis and Willis

(2005, 2006), Aifantis et al. (2006), and Abu Al-Rub et al. (2007) an intermediate kind of micro-boundary condition is introduced. Therefore, the interfacial energy φ presented in Eq. (2.42) can be assumed to have the following form in analogy with linearly hardening bulk materials:

$$\varphi = \left[\gamma \varepsilon^{p(I)} + \frac{1}{2} \beta \left(\varepsilon^{p(I)} \right)^2 \right] f\left(T\right) \tag{2.43}$$

where, γ is the temperature dependent interfacial yield strength which characterizes the stiffness of the interface boundary in blocking dislocations from crossing the interface and β is another temperature dependent interfacial property which characterizes the interfacial hardening that results during the transference of dislocation pile-ups across the interface. The temperature dependence of γ and β are expressed by the function $f\left(T\right)$ which can have the following form:

$$f\left(T\right) = \left(1 - T/T_y\right)^{\alpha} \tag{2.44}$$

with, T_y being the temperature at the onset of yield. Substituting Eq. (2.43) into Eq. (2.42) gives,

$$h\ell^2 \nabla_k \varepsilon^{p(I)} = \left[\gamma + \beta \varepsilon^{p(I)} \right] f\left(T\right) \tag{2.45}$$

Eq. (2.45) defines the higher-order boundary condition at the interface. One can assume that the interfacial strength, γ and the interfacial hardening, β scales with the bulk yield strength, σ_y and bulk hardening, h by an interfacial length scale, ℓ_I such that

$$\gamma = \ell_I \sigma_y \text{ and } \beta = \ell_I h \tag{1.46}$$

CHAPTER III

SIZE EFFECTS IN MICRO/NANO STRUCTURES

3.1 Introduction

Size effect (i.e. the dependence of mechanical response on the structure size) is a subject of current increasing interest due to the fact that current applications in modern technology involve a variety of length scales ranging from a few centimeters down to a few nanometers. The emerging area of nanotechnology exhibits important differences that result from continuous modification of material microstructural characteristics with changing size, whereby the smaller is the size the stronger is the response. There are many experimental observations which indicate that, under certain specific conditions, the specimen size may significantly affect deformation and failure of the engineering materials and it is required a length scale for their interpretation. From the discussions of Chapter I and Chapter II, it is already evident that these phenomena cannot be explained by the classical continuum mechanics since no length scale enters the constitutive description. However, the gradient plasticity theory has been successful in addressing the size effect problem. This success stems out from the incorporation of a micro-structural length-scale parameter in the governing equations for the material description.

In Chapter II, a strain gradient plasticity theory has been developed based on laws of thermodynamics and in this chapter it is shown that, this theory can be effectively used to model several size effect problems. Size dependent behavior in biaxial loading of a plastic thin film on an elastic substrate and thermal cooling of a thin

film on a substrate are considered here to be investigated by the developed gradient theory. The qualitative aspects of the proposed interfacial properties are also discovered subsequently.

3.2 Biaxial Loading of a Thin Film on a Substrate

3.2.1 Analytical solution

A biaxially loaded elastic-plastic thin film of thickness d on a semi-infinite elastic substrate as shown in Figure 3.1 is considered. Let x_3 be the perpendicular axis to the film and $x_3 = 0$ corresponds to the film–substrate interface. The loading is defined by a monotonically increasing biaxial strain ε_o such that $\varepsilon_{11} = \varepsilon_{22} = \varepsilon_o$. A plane stress situation is assumed such that the non-vanishing stress components are

$$\sigma_{11} = \sigma_{22} = \sigma_o\left(x_3\right) \tag{3.1}$$

From the plastic incompressibility assumption and the symmetry, one can write the non-vanishing plastic strain components as

$$\varepsilon_{11}^p = \varepsilon_{22}^p = -2\varepsilon_{33}^p = \varepsilon_o^p\left(x_3\right) \tag{3.2}$$

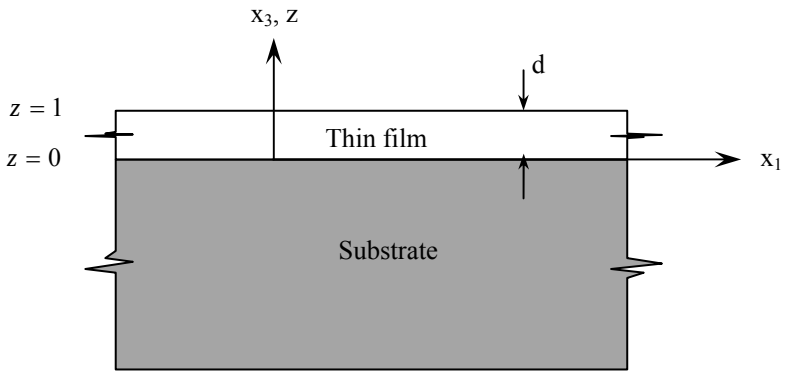

Fig. 3.1. An elasto-plastic thin film of thickness d on elastic substrate

The effective plastic strain, ε_e^p and its Laplacian, $\nabla^2\varepsilon_e^p$ are assumed in this case, to be,

$$\varepsilon_e^p = \varepsilon_o^p(x_3) \text{ and } \nabla^2\varepsilon_e^p = \varepsilon_{o,33}^p \tag{3.3}$$

Where, $\varepsilon_{o,33}^p = \partial\varepsilon_o^p / \partial x_3 \partial x_3$

The yield condition for the system can be expressed from Eq. (2.40) as:

$$\sqrt{\frac{3}{2}s_{ij}s_{ij}} = \sigma_e = \sigma_y + h\varepsilon^p - h\ell^2\nabla^2\left(\varepsilon^p\right) \tag{3.4}$$

And the generalized Hook's law can be used to obtain the stress-strain relationship,

$$\sigma_o(x_3) = \frac{E}{1-\upsilon}\left[\varepsilon_o - \varepsilon_o^p(x_3)\right] \tag{3.5}$$

Using Eqs. (3.1) and (3.3) into the yield condition in Eq. (3.4), yields the following ordinary differential equation for $\varepsilon_o^p\left(x_3\right)$:

$$\varepsilon_{o,33}^p - \frac{1}{\ell^2}\varepsilon_o^p = \frac{\sigma_y - \sigma_o}{h\ell^2} \tag{3.6}$$

The above equation is more conveniently expressed in a non-dimensional form with the aid of variable substitution (i.e. $z = x_3/d$, $\bar{\varepsilon}_o^p = \varepsilon_o^p/\varepsilon_y$ and $\bar{\varepsilon}_o = \varepsilon_o/\varepsilon_y$, where, $\varepsilon_y = (1-\upsilon)\sigma_y/E$ is the in-plane yield strain) such that:

$$\bar{\varepsilon}_{o,zz}^p - \lambda^2\bar{\varepsilon}_o^p = -F \tag{3.7}$$

With the constant co-efficients λ and F are given through,

$$\lambda = d/\ell \text{ and } F = \frac{(E/h)(\bar{\sigma}_o - 1)}{(1-\upsilon)(\ell/d)^2} \tag{3.8}$$

where, $\bar{\sigma}_o = \sigma_o/\sigma_y$.

The normalized stress-strain relationship can be written, from Eq. (3.5) to be,

$$\bar{\sigma}_o(z) = \bar{\varepsilon}_o - \bar{\varepsilon}_o^p(z) \tag{3.9}$$

Eq. (2.42) through (2.45) specifies the higher order boundary conditions for the current problem. At the film free surface ($x_3 = d$), $q = h\ell^2\varepsilon^p_{,3} = 0$ and at the film-substrate interface for an isothermal condition, ($x_3 = 0$), $q = h\ell^2\varepsilon^p_{,3} = \left[\gamma + \beta\varepsilon^{p(I)}\right]$. Therefore, the dimensionless boundary conditions for the problem are,

$$\bar{\varepsilon}^p_{o,z}\Big|_{z=1} = 0 \tag{3.10}$$

$$\left(\ell/d\right)\bar{\varepsilon}^p_{o,z}\Big|_{z=0} = \delta_1\frac{E/h}{1-\upsilon} + \delta_2\,\bar{\varepsilon}^p_o\Big|_{z=0} \tag{3.11}$$

where $\delta_1 = \gamma/\sigma_y\ell$ and $\delta_2 = \beta/h\ell$ are the non-dimensional interfacial strength and hardening, respectively. Solution to the differential equation with the stated boundary conditions is obtained to be,

$$\bar{\varepsilon}^p_o\left(z\right) = \frac{F}{\lambda^2} - \frac{\delta_1\left(\dfrac{E/h}{1-\upsilon}\right) + \delta_2\left(F/\lambda^2\right)}{Sinh\lambda + \delta_2 Cosh\lambda}Cosh\lambda\left(1-z\right) \tag{3.12}$$

with,
$$\frac{F}{\lambda^2} = \frac{\left(E/h\right)\left(\bar{\sigma}_o - 1\right)}{\left(1-\upsilon\right)}H\left(\bar{\sigma}_o - 1\right) \tag{3.13}$$

Here, Heaviside step function, $H\left(\bar{\sigma}_o - 1\right)$ is favorably used to imply that, $\bar{\varepsilon}^p_o = 0$ as long as $\sigma_o \le \sigma_y$. For $\delta_1 = \delta_2 = 0$, one obtains the classical solution $\bar{\varepsilon}^p_o\left(z\right) = F/\lambda^2$ which is uniform along d.

Substituting Eq. (3.12) along with Eq. (3.13) into the normalized stress-strain relationship, Eq. (3.9), expression for the normalized stress as a function of z to be,

$$\bar{\sigma}_o(z) = \frac{\bar{\varepsilon}_o + \frac{E/h}{1-\upsilon}\left[1 + \frac{(\delta_1 - \delta_2)Cosh\lambda(1-z)}{Sinh\lambda + \delta_2 Cosh\lambda}\right]}{1 + \frac{E/h}{1-\upsilon}\left[1 - \frac{\delta_2 Cosh\lambda(1-z)}{Sinh\lambda + \delta_2 Cosh\lambda}\right]} \tag{3.14}$$

The above equation can be integrated to obtain the average stress over the thickness, d to be,

$$\bar{\sigma}_o^{\,avg} = \frac{\bar{\varepsilon}_o + \frac{E/h}{1-\upsilon}\left[1 + \frac{(\delta_1 - \delta_2)/\lambda}{1 + \delta_2 Coth\lambda}\right]}{1 + \frac{E/h}{1-\upsilon}\left[1 - \frac{\delta_2/\lambda}{1 + \delta_2 Coth\lambda}\right]} \tag{3.15}$$

3.2.2 Qualitative analysis of biaxially loaded thin film

Eqs. (3.12) through (3.15) can be used to analyze, qualitatively, the behavior of biaxially loaded thin films on elastic substrates. To analyze effect of size scale and interfacial properties, an aluminum thin film on silicon substrate is considered. The size effect is achieved by varying ℓ/d while, varying δ_1 and δ_2 incorporate effects of interfacial energy. Typical properties of aluminum are adopted ($E = 70\,GPa$, $\nu = 0.33$, $\sigma_y = 36\,MPa$ and $E/h = 0.2$). Different sizes are represented by $\ell/d = 0.1$, 0.5, 1.0, 1.5 and 2.0.

The level of interfacial energy at the interface is controlled by both the normalized interfacial yield strength parameter, δ_1 and hardening parameter δ_2. Four

different cases, that are expressed by the mathematical forms of the interfacial energy φ, can be considered for qualitative examination:

Case 1: $\varphi = \gamma \varepsilon^{p(I)}$, which indicates that the interface is not allowed to harden. This is achieved by setting $\delta_2 = 0$ in the preceding analytical developments.

Case 2: $\varphi = \frac{1}{2}\beta\left(\varepsilon^{p(I)}\right)^2$, which indicates that the interface yields at the same time when the bulk interior yields but it is allowed to harden differently. This is equivalent to setting $\delta_1 = 0$

Case 3: $\varphi = \gamma \varepsilon^{p(I)} + \frac{1}{2}\beta\left(\varepsilon^{p(I)}\right)^2$, this form characterizes both the interfacial yielding and hardening analogous to the bulk interior. The expressions in Eq. (3.11) through (3.15) are used as they are and different values of δ_1 and δ_2 ($\delta_1 \neq \delta_2$) are used.

Case 4: $\varphi = \ell_I\left[\sigma_y \varepsilon^{p(I)} + \frac{1}{2}h\left(\varepsilon^{p(I)}\right)^2\right]$, which is equivalent to setting $\delta_1 = \delta_2 = \delta = \ell_I / \ell$ in Eqs. (3.12) through (3.15). This is similar to case 3 but both the yield strength and hardening are controlled by the boundary layer length scale ℓ_I.

Case 1: Influence of the interfacial yield strength

The influence of the interfacial yield strength, γ, separated from the effect of interfacial hardening, β, is examined first by varying the non-dimensional measure δ_1 and setting $\delta_2 = 0$. Figure 3.2 study the stress-strain relationship from Eq. (3.15). The interfacial yield strength is varied from $\delta_1 = 0.1$ [Fig. 3.2(a)] and $\delta_1 = 0.45$ [Fig. 3.2(b)].

Namely, $\delta_1 = 0.1$ corresponds to a compliant interface (i.e. interface with low yield strength, and $\delta_1 = 0.45$ corresponds to a stiff interface (i.e. interface with high yield strength. As expected, both of them show strong size effects i.e. the smaller is the size (higher ℓ/d) stronger is the response. But more interestingly, an increase in global yield strength is observer with either decreasing size (increasing ℓ/d) or with increasing

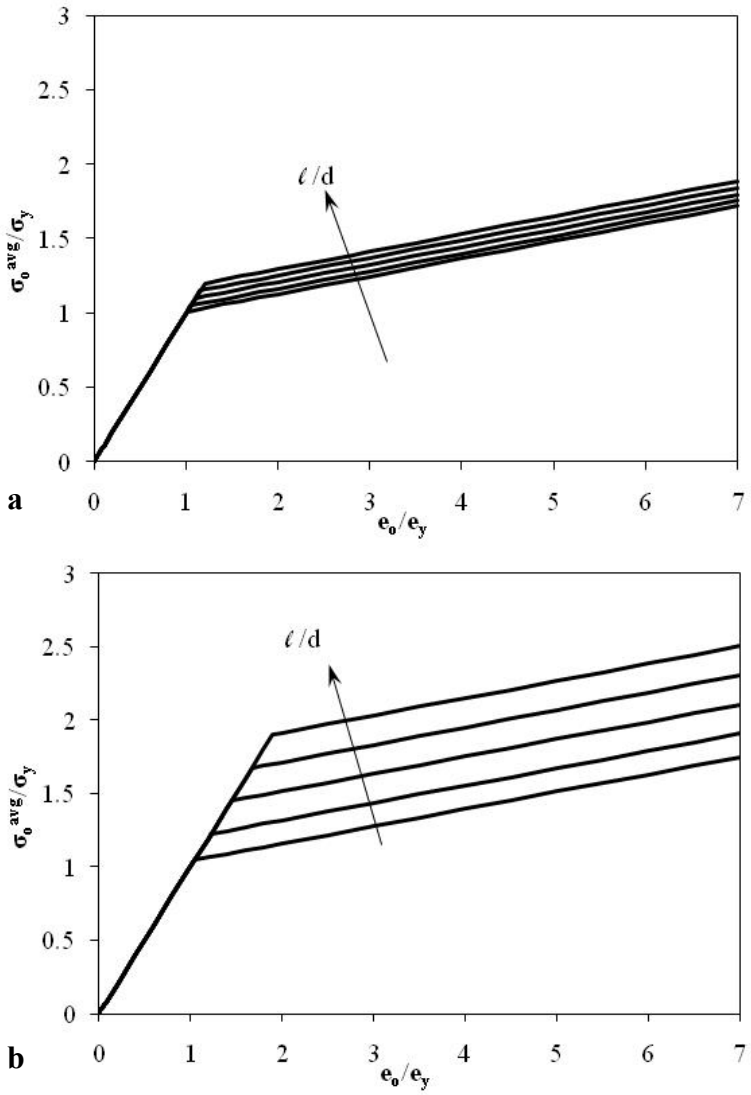

Fig. 3.2. Size effect in stress-strain relationship due to interfacial yield strength only ($\delta_2 = 0$). $\delta_1 = 0.1$ for (a) and $\delta_1 = 0.45$ for (b)

interfacial yield strength (increasing δ_1). This indicates that interfacial yield strength has determining effects on the global yield strength. The tangent hardening modulus shows no increment after yield point in either case which is an expected response since the interface is not allowed to hardened by setting $\delta_2 = 0$.

Figures 3.3 show the effects of varying interfacial strength on the distribution of plastic strain and total stress through the characteristic size d at an applied normalized strain of $\bar{\varepsilon}_o = 3$. The size effect in case of normalized total stress [Fig. 3.3(c,d)], $\bar{\sigma}_o$ shows opposite trend to that in case of $\bar{\varepsilon}$ (i.e. increase with decreasing size). However,

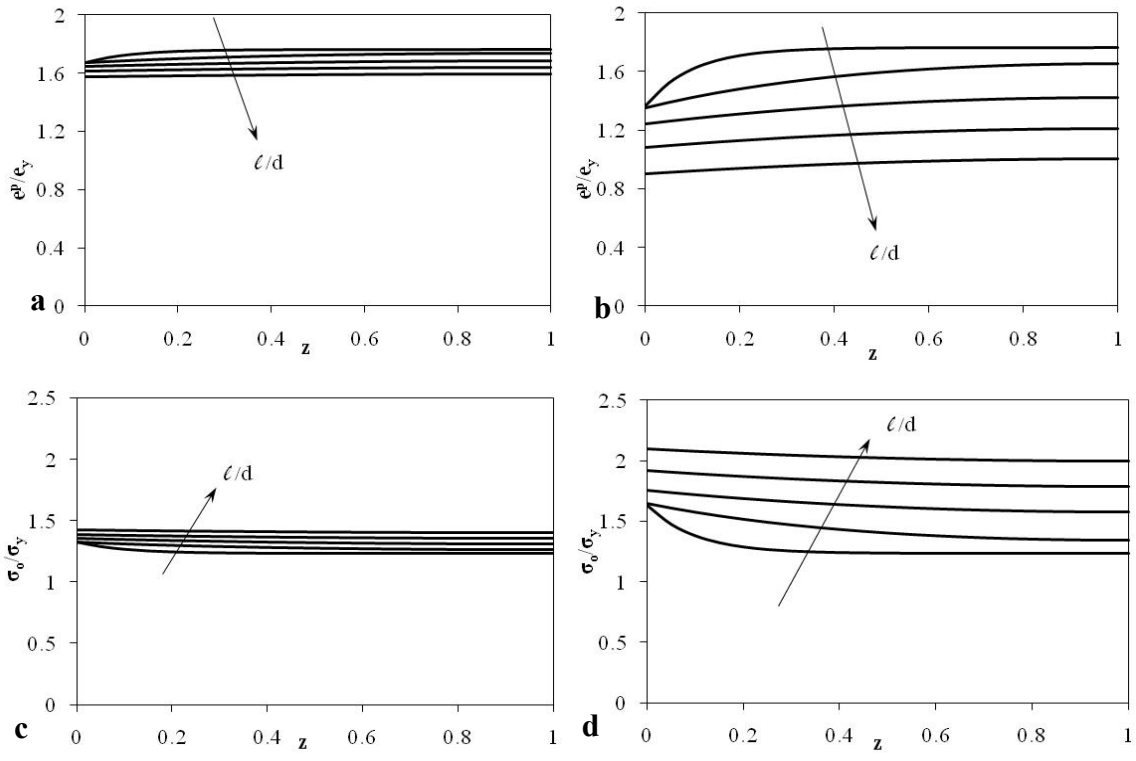

Fig. 3.3. Size effects in normalized plastic strain and total stress distributions due to interfacial yield strength only ($\delta_2 = 0$). $\delta_1 = 0.1$ for (a,c) and $\delta_1 = 0.45$ for (b,d)

the size effect becomes much more prominent as the interface is made stiffer which is the similar to what was seen in case of Fig 3.3(a,b).

One can obtain for this case (i.e. when the interfacial hardening is neglected) an expression for the yield strength in Fig. 3.2 (i.e. onset of plasticity in the bulk interior) as a function of the interfacial yield strength, γ, and size, d, by simply finding the value of the normalized applied stress at which the average plastic strain in the specimen is zero; that is, $\bar{\sigma}_o = \bar{\sigma}_Y$ when $\left(\bar{\varepsilon}_o^p\right)^{avg} = 0$, where $\bar{\sigma}_Y$ is interpreted as the normalized global size-dependent yield strength of the whole specimen and $\left(\bar{\varepsilon}_o^p\right)^{avg}$ is the average plastic strain in the specimen. This can be achieved simply by setting $\delta_2 = 0$ in Eq. (3.12), integrating the result over z, and substituting $\lambda = d/\ell$, which yields

$$\bar{\sigma}_Y = 1 + \delta_1 \left(\ell/d\right) \tag{3.16}$$

This can be rewritten after substituting $\bar{\sigma}_Y = \sigma_Y/\sigma_y$ and $\delta_1 = \gamma/\sigma_y\ell$ as follows:

$$\sigma_Y = \sigma_y + \gamma/d \tag{3.17}$$

This relation shows that the yield strength, σ_Y, scales with the interfacial yield strength, γ, and increases linearly with the inverse of the specimen size, d^{-1} (note that d could be interpreted here as the grain size, film thickness, or any characteristic dimension where there is variation in the plastic strain distribution).

It is noteworthy that Eq. (3.17)matches to a great extent the findings of some of the experimental and discrete dislocation studies of the dependence of the yield strength on the thickness of thin metal films. For example, the effects of grain size and film

thickness on the yield strength were separated experimentally by Venkatraman and Bravman (1992). Those authors established an almost linear increase of yield strength with the inverse of both film thickness and grain size. Also, the calculations made by Nix (1989) of thin film plasticity with a single misfit dislocation proposed a linear dependence of the flow stress on the inverse of the film thickness.

Case 2: Influence of the interfacial hardening

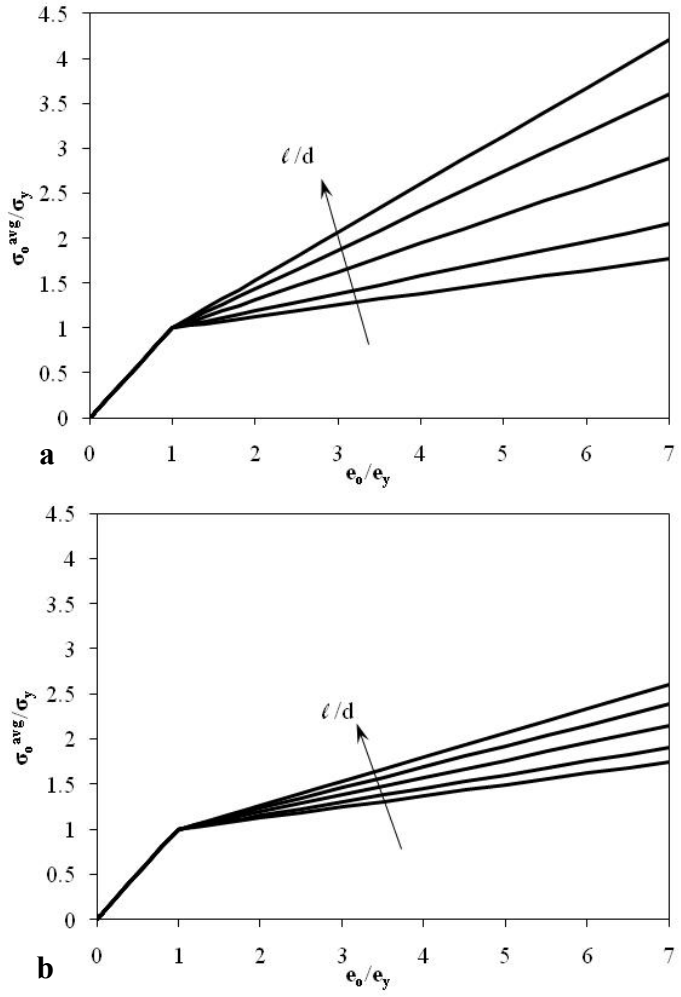

Fig. 3.4. Size effect in stress-strain relationship due to interfacial hardening only ($\delta_1 = 0$). $\delta_2 = 1$ for (a) and $\delta_2 = 10$ for (b)

Figure 3.4 (a and b) for two interface conditions; an intermediate interface with $\delta_2 = 1$ and a hard interface with $\delta_2 = 10$ respectively. The additional contribution to strain hardening is attributed to the presence of interfacial hardening through non zero δ_2 values that give rise to the interaction of dislocations with the interface. Figure 3.5 show the effects of varying interfacial strength on the distribution of plastic strain and total

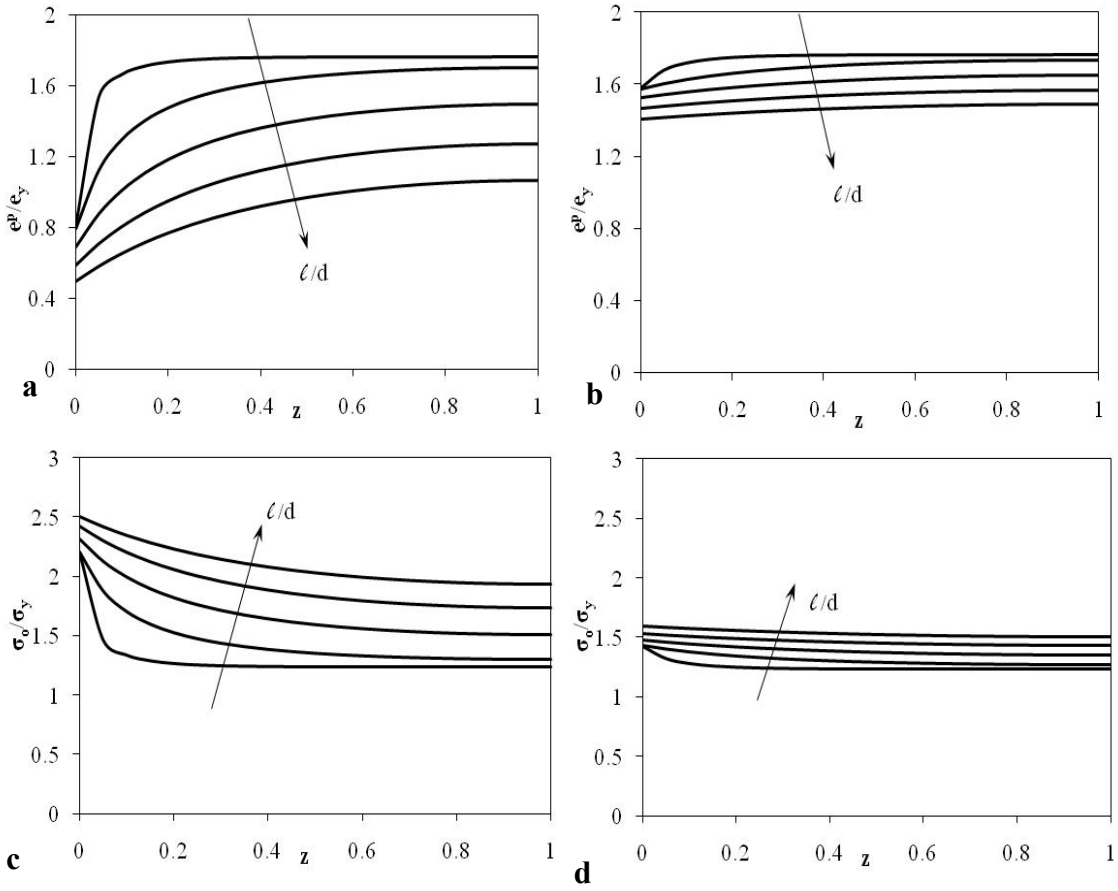

Fig. 3.5. Size effects in normalized plastic strain and total stress distributions due to interfacial hardening only ($\delta_1 = 0$). $\delta_2 = 1$ for (a,c) and $\delta_2 = 10$ for (b,d)

stress through the characteristic size d. In all the Figures of 3.4 and 3.5, size effect is observed as expected and it is more prominent with a harder interface.

Following similar procedures to those that led to Eqs. (3.16) and (3.17) one finds a constant (size independent) value of $\bar{\sigma}_Y = 1$, for $\delta_1 = 0$ and $\delta_2 \neq 0$. This can also be seen from Fig. 3.4 (a,b) that the yield stress is independent of (ℓ/d) and β such that the bulk and the interface yields at the same time.

From the above results, one concludes that the inclusion of the interfacial hardening, β, enables one to qualitatively describe the strain hardening (i.e. increase inflow stress and tangent modulus), but it cannot predict any strengthening (i.e. increase in the yield strength) with decreasing size. On the other hand, the inclusion of the interfacial yield strength, γ, enables one to qualitatively predict strengthening but without further increasing the strain hardening rate with decreasing size. Therefore, since an increase in the yield strength is usually accompanied by an increase in the hardening rate, which is often seen in experimental results for diminishing sizes (e.g. Huang and Spaepen, 2000; Shrotriya et al., 2003; Haque and Saif, 2003; Espinosa et al., 2004; Uchic et al., 2004; Dimiduk et al., 2005; Greer et al., 2005; Volkert and Lilleodden, 2006; Simons et al., 2006).

Case 3 and 4: Combined influence of the interfacial yield strength and hardening

The combined effect of interfacial yield strength and interfacial hardening is examined here. Figure 3.6 (a and b) show the average stress-strain relationships for $\delta_1 = 0.45$ while interfacial hardening is varied between values, $\delta_2 = 1$ and $\delta_2 = 10$. As

expected, both global yield strength and plastic strain rate are subjected to size effects such that, a decrease in characteristic size, d shows increment in both global yield strength and plastic hardening rate. This is a desirable behavior since it conforms to the

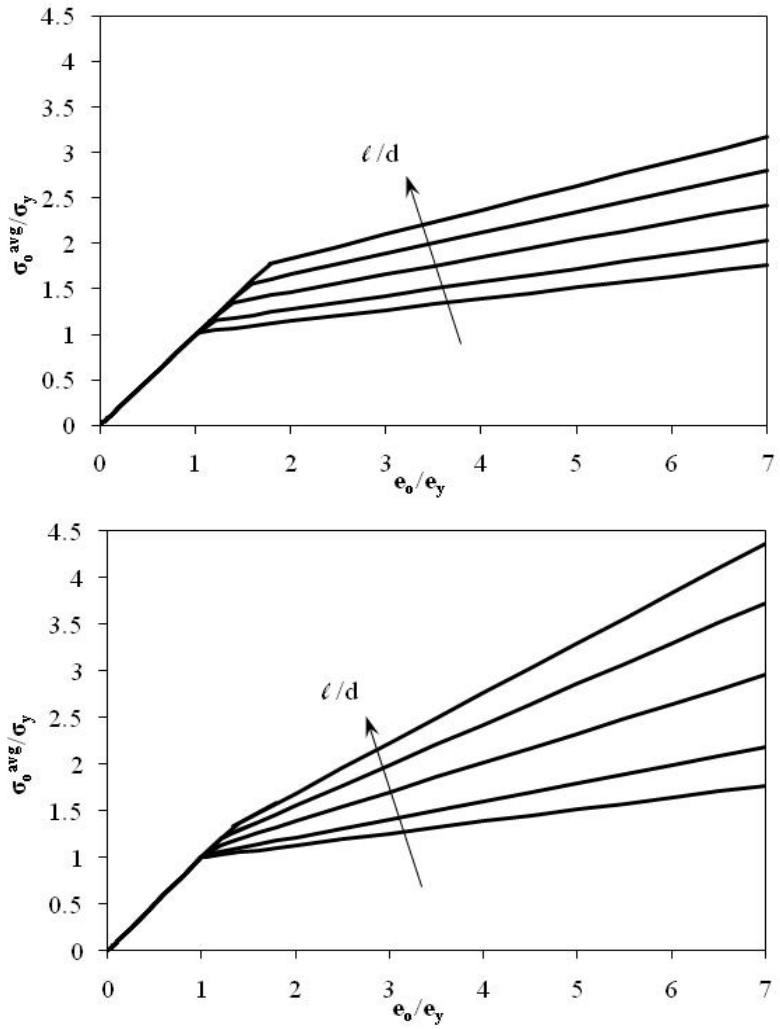

Fig. 3.6. Size effect in stress-strain relationship due to both interfacial yield strength and hardening $\delta_1 = 0.45$ in all cases while $\delta_2 = 1$ for (a) and $\delta_2 = 10$ for (b)

experimental results at the micron and submicron length scales (see Fleck et al., 1994; Huang and Spaepen, 2000; Haque and Saif, 2003; Espinosa et al., 2004). But, the size effect in yield strength is decreased with the increase of interfacial hardening ($\delta_2 = 1$ to $\delta_2 = 10$) although, interfacial yield strength is kept same in both occasions ($\delta_1 = 0.45$). This indicates that, global yield strength is sensitive to both interfacial yield strength and hardening.

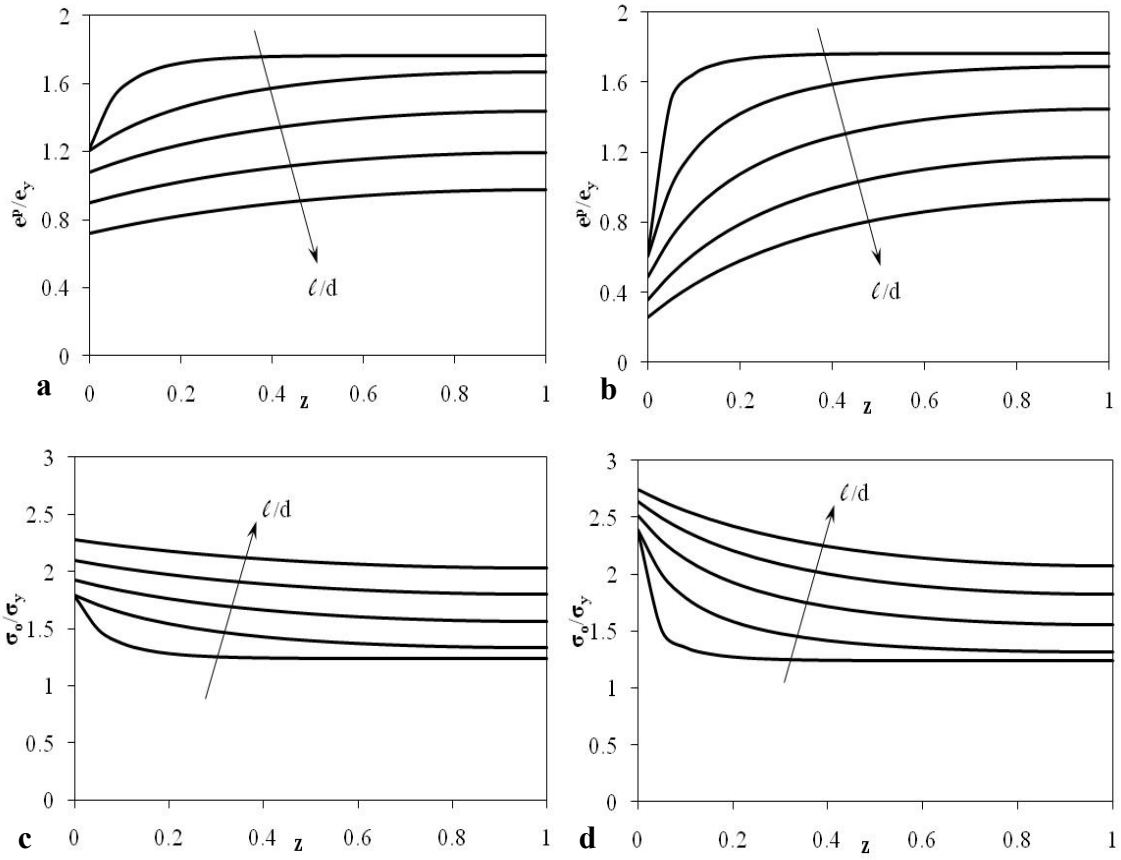

Fig. 3.7. Size effects in normalized plastic strain and total stress distributions due to both interfacial yield strength and hardening. $\delta_1 = 0.45$ in all cases while. $\delta_2 = 1$ for (a,c) and $\delta_2 = 10$ for (b,d)

The plastic strain and stress distributions listed in Figures 3.7 show essentially, similar qualitative behavior to those listed in Figures 3.3 and 3.5.

An expression for the normalized yield strength, $\bar{\sigma}_Y$ as a function of both interfacial yield strength and hardening, (δ_1 and δ_2, respectively) can be obtained by following procedures similar to those involved in obtaining Eq. (3.16) such that,

$$\bar{\sigma}_Y = 1 + \frac{\delta_1}{\lambda + \delta_2 \left(\lambda Coth\lambda - 1\right)} \tag{3.18}$$

It can be seen from the above equation that the global yield strength is sensitive to both the interfacial yield strength and the interfacial hardening in way that, increasing interfacial hardening will decrease the global yield strength. This is an undesirable behavior since one expects that by increasing the interfacial hardening, increase in both the yield strength and the strain hardening rate should be achieved.

A different approach may be to change the interfacial yield strength and hardening such that δ_1 and δ_2 are equal to each other. It is a way of declaring the interdependency of the two interfacial terms such that increasing one will result in an automatic increase to the other. Therefore, by setting $\delta_1 = \delta_2 = \delta = \ell_I / \ell$ in Eq. (3.18) the expression for the size dependent global yield strength becomes,

$$\bar{\sigma}_Y = 1 + \left[\lambda/\delta + \lambda Coth\lambda - 1\right]^{-1} \tag{1.19}$$

The above expression shows an increase in the global yield strength with increasing δ. This is more evident in the Figure 3.8 where $\delta\left(=\delta_1 = \delta_2\right)$ is increased from 0.45 to 1.0 and a significant increase in the global yield strength is observed. The

slight increase in the strain hardening rate is easily attributed to the increase in the interfacial hardening value.

A physical interpretation of this behavior is that the increase in interfacial hardening is marked by increased dislocation interactions in the interface which results in a stiff network of dislocations and thus increases the resistance to plastic deformation at the interface such that a stiff interface is obtained.

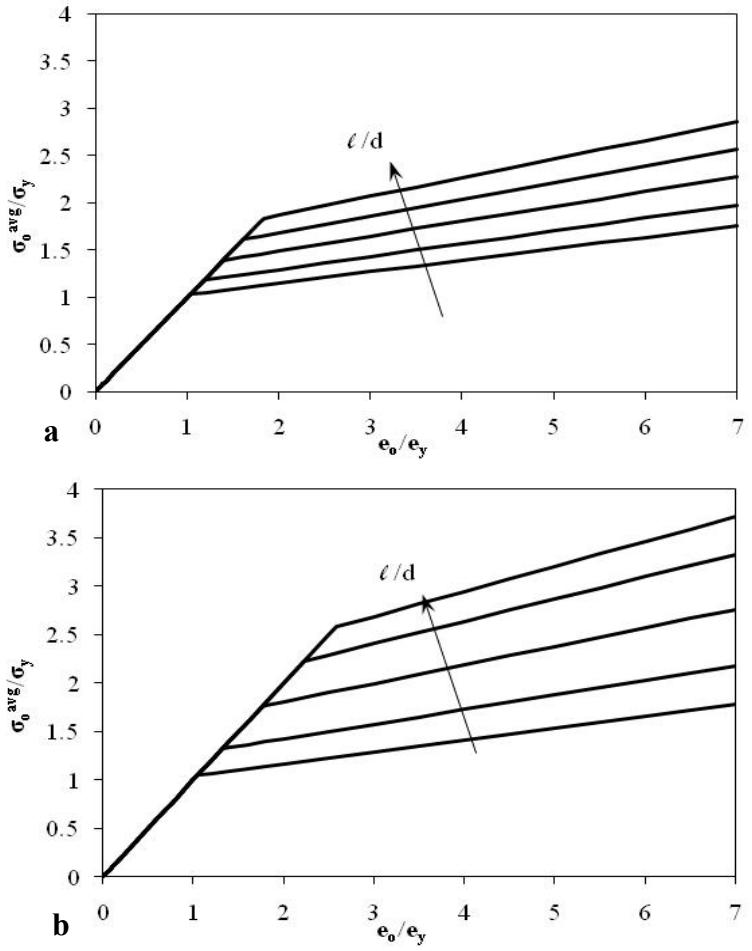

Fig. 3.8. Size effect in stress-strain relationship due to both interfacial yield strength and hardening $\delta = 0.45$ for (a) and $\delta = 1.0$ for (b)

Therefore, the interfacial hardening and interfacial yield strength are interdependent and as such cannot be varied independently.

3.3 Thermal Loading of a Thin Film on a Substrate

3.3.1 Analytical solution

The problem of a thin film on a semi-infinite substrate subjected to thermal load-

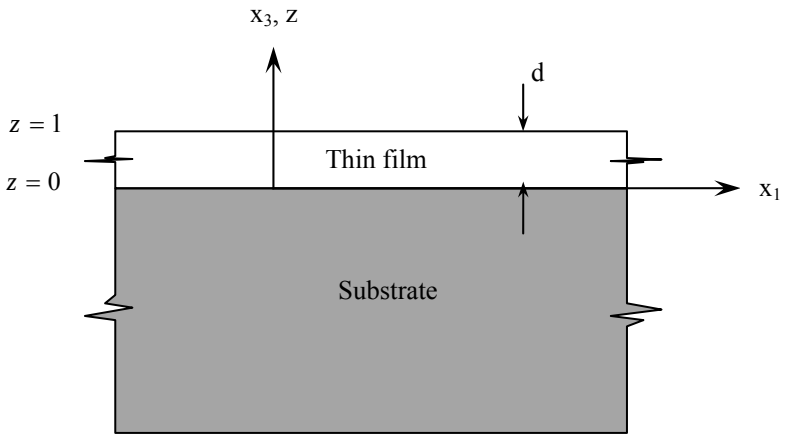

Fig. 3.9. An elasto-plastic thin film of thickness d on elastic substrate

ing will be studied now. A quasi-static monotonic thermal loading is imposed by cooling the film–substrate system from an initial temperature T_o at which the film and substrate are stress free and dislocation free. The substrate undergoes unconstrained contraction but, due to the mismatch between the thermal-expansion coefficient of the film, α_f, and the substrate, α_s, stress develops in the film; which is tensile for $\alpha_f > \alpha_s$. Since the film is infinitely long in the x_1-direction (Figure 3.9) and initially homogeneous, the solution depends only on x_3 such that by assuming a plane strain problem in the x_2 direction one can write

$$\sigma_{33} = \sigma_{13} = 0 \text{ and, } \sigma_{11} = \sigma_o\left(x_3\right) \tag{3.20}$$

where the stress field, $\sigma_o\left(x_3\right)$, is non-uniform and unknown at this stage. Because of symmetry and because the strain components do not depend on x_1, the total strain $\varepsilon_{11} = \varepsilon_o$ must be uniform throughout the film such that the effective plastic strain, ε^p, and its laplacian, $\nabla^2\varepsilon^p$ in this case can be assumed as follows,

$$\varepsilon^p = \varepsilon_o^p\left(x_3\right) \quad \text{and} \quad \nabla^2\varepsilon^p = \varepsilon_{o,33}^p \tag{3.21}$$

where $\varepsilon_{o,33}^p = \partial^2\varepsilon_o^p / \partial x_3^2$. For a plane strain condition, the stress-strain relationship can be expressed as follows,

$$\sigma_o\left(x_3\right) = \frac{E}{1-\nu^2}\varepsilon_o^e\left(x_3\right) \tag{3.22}$$

where E is the Young's modulus and ν is the Poisson's ratio. The total strain in the film can be decomposed into elastic, plastic, and thermal components, given by,

$$\varepsilon_o = \varepsilon_o^e + \varepsilon_o^p + \left(1+\nu\right)\alpha_f\Delta T \tag{3.23}$$

where $\Delta T = T - T_o$ is the temperature change and the term $(1+\nu)$ is a result of the plan strain assumption. Compatibility of deformation between the film and the substrate requires that ε_o be the same and uniform throughout the film. The total strain in the substrate is given by,

$$\varepsilon_o = \left(1+\nu\right)\alpha_s\Delta T \tag{3.24}$$

In Eqs. (3.23) and (3.24), $\nu_f = \nu_s = \nu$ is assumed. Substituting ε_o^e from Eqs. (3.23) and (3.24) into Eq. (3.22) yields,

$$\sigma_o\left(x_3\right)=\frac{E}{1-\nu^2}\left[\left(1+\nu\right)\left(\alpha_s-\alpha_f\right)\Delta T-\varepsilon_o^p\left(x_3\right)\right] \tag{3.25}$$

In the elastic range, the above equation can be utilized to relate the yield stress with the temperature at the onset of yield (i.e. by substituting $T=T_y$ when $\sigma_o=\sigma_y$) by setting $\varepsilon_o^p=0$ in Eq. (3.25) such that,

$$\sigma_y=\frac{E}{1-\nu}\left(\alpha_s-\alpha_f\right)\left(T_y-T_o\right) \tag{3.26}$$

Following from the yield condition in Eq. (3.4) with Eqs. (3.20) and (3.21), one gets,

$$f=\sigma_o-\sigma_y-h\varepsilon_o^p+h\ell^2\varepsilon_{o,33}^p=0 \tag{3.27}$$

Substituting Eq. (3.25) into Eq. (3.27) along with Eq. (3.26) yields the following ordinary differential equation for $\varepsilon_o^p\left(x_3\right)$:

$$\varepsilon_{o,33}^p-\frac{1}{\ell^2}\left[1+\frac{E/h}{\left(1-\nu^2\right)}\right]\varepsilon_o^p=\frac{E/h}{\ell^2\left(1-\nu\right)}\left(\alpha_f-\alpha_s\right)\left(T-T_y\right) \tag{3.28}$$

The above equation is more conveniently expressed as a non-dimensional form with the aid of variable substitution (i.e. $z=x_3/d$) such that:

$$\varepsilon_{o,zz}^p-\lambda^2\varepsilon_o^p=-F \tag{3.29}$$

with the constant coefficients λ and F are given through,

$$\lambda^2=\frac{1}{\left(\ell/d\right)^2}\left[1+\frac{E/h}{\left(1-\nu^2\right)}\right] \text{ and } F=\frac{E/h}{\left(\ell/d\right)^2\left(1-\nu\right)}\left(\alpha_f-\alpha_s\right)\left(T_y-T\right) \tag{3.30}$$

Eq. (2.42) through (2.45) specifies the higher order boundary conditions for the current problem.. At the film free surface ($x_3=d$), $q=h\ell^2\varepsilon_{,3}^p=0$ and at the film-

substrate interface ($x_3 = 0$), $q = h\ell^2 \varepsilon_{,3}^p = \left[\gamma + \beta\varepsilon^{p(I)}\right] f(T)$. Therefore, the dimensionless boundary conditions for the problem are,

$$\varepsilon_{o,z}^p\Big|_{z=1} = 0 \tag{3.31}$$

$$(\ell/d)\,\varepsilon_{o,z}^p\Big|_{z=0} = \left[\delta_1 \sigma_y/h + \delta_2\, \varepsilon_o^p\Big|_{z=0}\right] f(T) \tag{3.32}$$

where $\delta_1 = \gamma/\sigma_y \ell$ and $\delta_2 = \beta/h\ell$ are the non-dimensional interfacial strength and hardening, respectively. Solution to the differential equation with the stated boundary conditions is obtained to be,

$$\varepsilon_o^p(z) = \frac{F}{\lambda^2} + \frac{\left[\delta_1\left(\sigma_y/h\right) + \delta_2\left(F/\lambda^2\right)\right] f(T)}{\lambda(\ell/d) + \delta_2 f(T) Coth\lambda}\left[Sinh\lambda z - Coth\lambda\ Cosh\lambda z\right] \tag{3.33}$$

$$\text{with,} \quad \frac{F}{\lambda^2} = \frac{(1+\nu)E/h}{(1-\nu^2) + E/h}\left(\alpha_f - \alpha_s\right)\left(T_y - T\right) \tag{3.34}$$

which can be rewritten after substituting Eqs. (3.34) as follows:

$$\begin{aligned}\varepsilon_o^p(z) = {} & \frac{\delta_1 f(T)\sigma_y/h}{\lambda(\ell/d) + \delta_2 f(T) Coth\lambda}\left[Sinh\lambda z - Coth\lambda Cosh\lambda z\right] \\ & + \frac{(1+\upsilon)(E/h)\left(\alpha_f - \alpha_s\right)\left(T_y - T\right)}{\left(1-\upsilon^2\right) + E/h}\left[1 + \frac{\delta_2 f(T)\left(Sinh\lambda z - Coth\lambda Cosh\lambda z\right)}{\lambda(\ell/d) + \delta_2 f(T) Coth\lambda}\right]\end{aligned} \tag{3.35}$$

Substituting the above equation into Eq. (3.25) yields a linear relationship between σ_o and T as follows:

$$\sigma_o(z) = \sigma_n - c\left(Sinh\lambda z - Coth\lambda Cosh\lambda z\right) \tag{3.36}$$

with

$$\sigma_n = \frac{E}{1-\nu}\left(\alpha_f - \alpha_s\right)\left[\left(T_o - T\right) - \frac{\left(T_y - T\right)}{1+\left(1-\nu^2\right)\left(h/E\right)}\right] \tag{3.37}$$

$$c = \frac{E}{1-\nu^2} f\left(T\right)\left[\frac{\delta_1 \sigma_y / h + \delta_2 F/\lambda^2}{\lambda\left(\ell/d\right) + \delta_2 f\left(T\right) Coth\lambda}\right] \tag{3.38}$$

Integrating Eqs. (3.35) and (3.36) over the thickness of the film (i.e. from $z = 0$ to $z = 1$) gives the average plastic strain $\varepsilon_o^{p,avg}$ and average stress σ_o^{avg} such that,

$$\varepsilon_o^{p,avg} = \frac{F}{\lambda^2} - \left(\frac{1-\upsilon^2}{E}\right)\frac{c}{\lambda} \tag{3.39}$$

$$\sigma_o^{avg} = \sigma_n + \frac{c}{\lambda} \tag{3.40}$$

3.3.2 Qualitative analysis of thermal loading of a thin film

The analytical relations developed so forth (Eqs. (3.33) through (3.40), are used here for qualitative analysis of 'thermal loading of a thin film' problem. Once again, an aluminum thin film on silicon substrate having typical properties, ($E = 70 GPa$, $\nu = 0.33$, $\sigma_y = 36 MPa$, $\alpha_f = 23.3\times10^{-6}/K$, $\sigma_y = 36 MPa$ and $E/h = 0.2$) is considered. The analysis are done to simulate the cooling of the specimen from an initial temperature of $T_o = 600 K$ to $T = 400 K$. Thermal expansion coefficient for silicon is taken to be $\alpha_s = 3.0\times10^{-6}/K$. The temperature at which yielding occurs is calculated from Eq. (3.26) to be $T_y = 582.94 K$. Film thicknesses are varied as $\ell/d = 0.1, 0.5, 1.0, 1.5$ and 2. The size and interfacial energy effects are achieved by varying ℓ/d, δ_1 and δ_2

respectively. The four cases for interfacial energy φ considered in section 3.2.2 are also considered here.

Case 1: Influence of the interfacial yield strength

The interface is not allowed to harden by setting $\delta_2 = 0$ and varying the non-dimensional yield strength measure, δ_1. The resulting qualitative curves are shown in Figure 3.10. The interfacial yield strength is varied from $\delta_1 = 0.1$ [(a) and (c)] to $\delta_1 = 0.45$ [(b) and (d)].

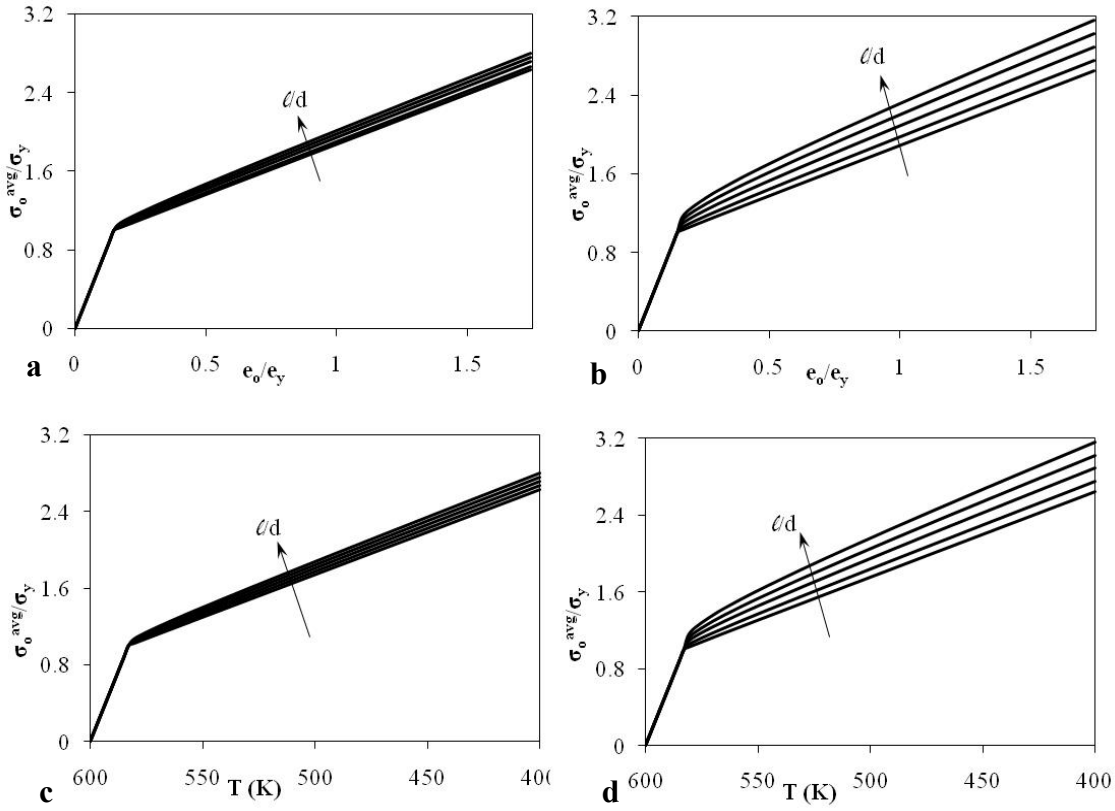

Fig. 3.10. Size effect in stress-strain relationship (a,b) and stress-temperature relationship (c,d) under thermal loading due to interfacial yield strength only ($\delta_2 = 0$). $\delta_1 = 0.1$ for (a) and (c) and $\delta_1 = 0.45$ for (b) and (d)

Figures (a) and (b) study the stress-strain relationship [average stress from Eq. (3.40) vs. total strain from Eq. (3.24)] and Figures (c) and (d) study the variation of average stress with decreasing temperature [Eq. (3.40)]. As expected, both of them show size effects i.e. the smaller is the size (higher ℓ/d) stronger is the response.

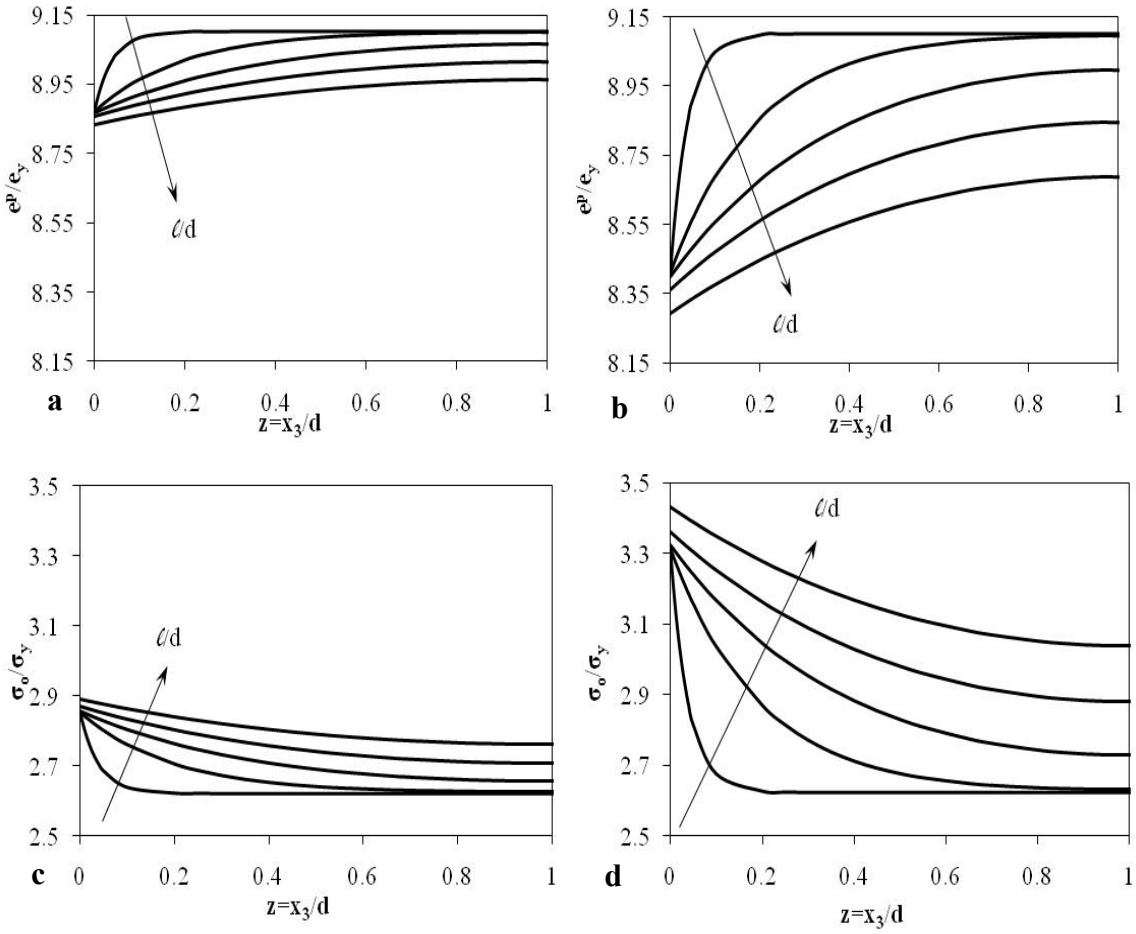

Fig. 3.11. Size effects in normalized plastic strain and total stress distributions due to interfacial yield strength only ($\delta_2 = 0$). $\delta_1 = 0.1$ for (a,c) and $\delta_1 = 0.45$ for (b,d)

But more interestingly, an increase in global yield strength is observer with either decreasing size (increasing ℓ/d) or with increasing interfacial yield strength (increasing δ_1). This indicates that interfacial yield strength has determining effects on the global yield strength. The tangent hardening modulus remain fairly uniform which is due to the fact that the interfacial hardening has been restricted by setting $\delta_2 = 0$.

Plastic strain distribution and total stress distributions along the characteristic size (thickness, d) due to the interfacial yielding effect for a temperature change from $600K$ to $400K$ are showed in Figure 3.11. Similar to the trends seen in the biaxial loading cases, here also, plastic strain distribution decreases with decreasing size, while the stress distribution increases with decreasing size. In both these cases, size effect increase with increasing γ.

Case 2: Influence of the interfacial hardening

The effect of interfacial hardening is studied by fixing $\delta_1 = 0$ (interface yields at the same time as the buck), while δ_2 is varied between $\delta_2 = 0.2$ and $\delta_2 = 1$ (Figure 3.12). In this case also, size effect is observed on the flow stress and hardening rate. The increment in tangential modulus is attributed to the presence of interfacial hardening through non zero δ_2 values. Although the global yield strength is unchanged which was expected given that, δ_1 has been set to zero.

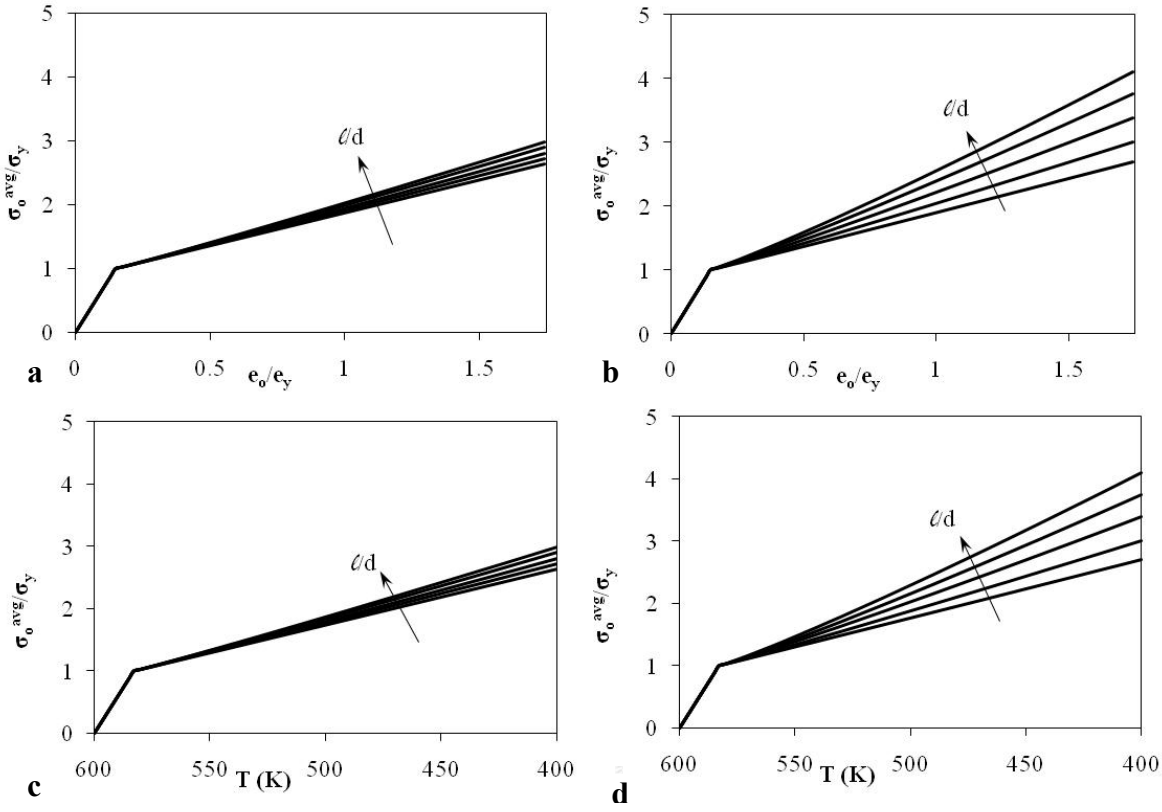

Fig. 3.12. Size effect in stress-strain relationship (a and b) and stress-temperature relationship (c and d) under thermal loading due to interfacial hardening only ($\delta_1 = 0$). $\delta_2 = 0.2$ for (a) and (c) and $\delta_2 = 1$ for (b) and (d)

Figure 3.13 show the effects of varying interfacial strength on the distribution of plastic strain and total stress through the characteristic size d. In all the Figures of 3.12 and 3.13, size effect is observed as expected and it is more prominent with a harder interface.

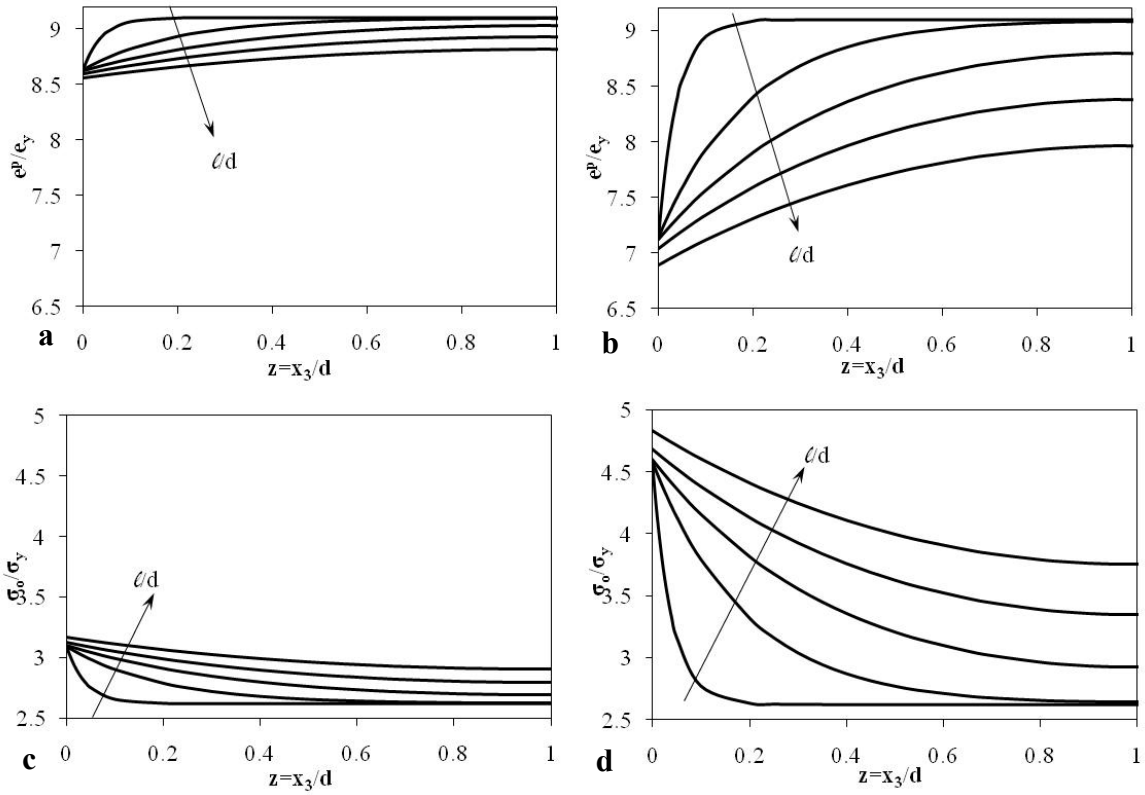

Fig. 3.13. Size effects in normalized plastic strain and total stress distributions due to interfacial hardness only ($\delta_1 = 0$). $\delta_2 = 0.2$ for (a,c) and $\delta_2 = 1.0$ for (b,d)

Case 3 and 4: Combined influence of the interfacial yield strength and hardening

The combined effect of interfacial yield strength and interfacial hardening is next examined. Figure 3.14 (a and b) shows the average stress-strain relationships for $\delta_1 = 0.45$ while δ_2 is varied between values, 0.2 and 1.0. As expected, both global yield strength and plastic strain rate are subjected to size effects such that, a decrease in characteristic size, d shows increment in both global yield strength and plastic hardening rate. But, the rate of increment in yield strength is decreased with the increase

of interfacial hardening ($\delta_2 = 0.2$ to $\delta_2 = 1.0$) although, interfacial yield strength is kept same in both occasions ($\delta_1 = 0.45$). This indicates that, global yield strength is sensitive to both interfacial yield strength and hardening. Similar arguments as those in case of biaxial loading can be made to explain this behavior. In this case also, varying the interfacial hardening and yield strength such that, $\delta_1 = \delta_2 = \delta$ gives better response as shown in Figure 3.15.

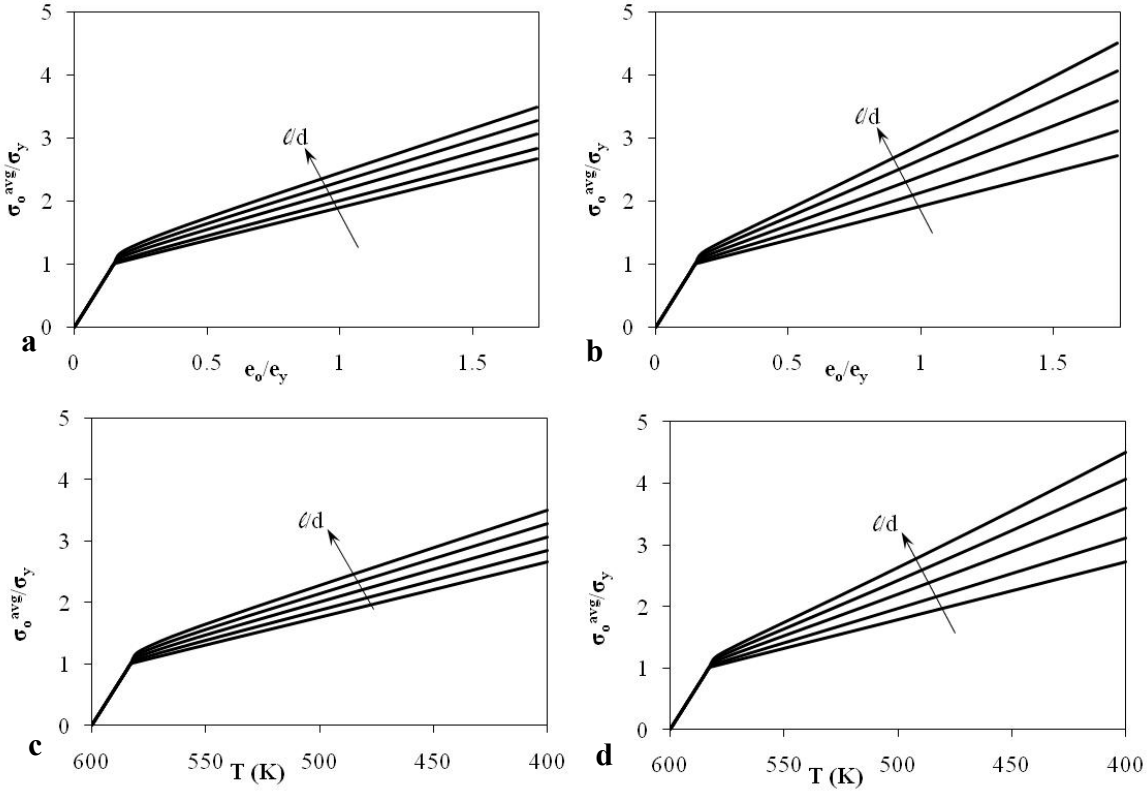

Fig. 3.14. Size effect in stress-strain relationship (a and b) and stress-temperature relationship (c and d) under thermal loading due to interfacial yield strength and hardening $\delta_1 = 0.45$ in all cases while. $\delta_2 = 0.2$ for (a,c) and $\delta_2 = 1$ for (b,d)

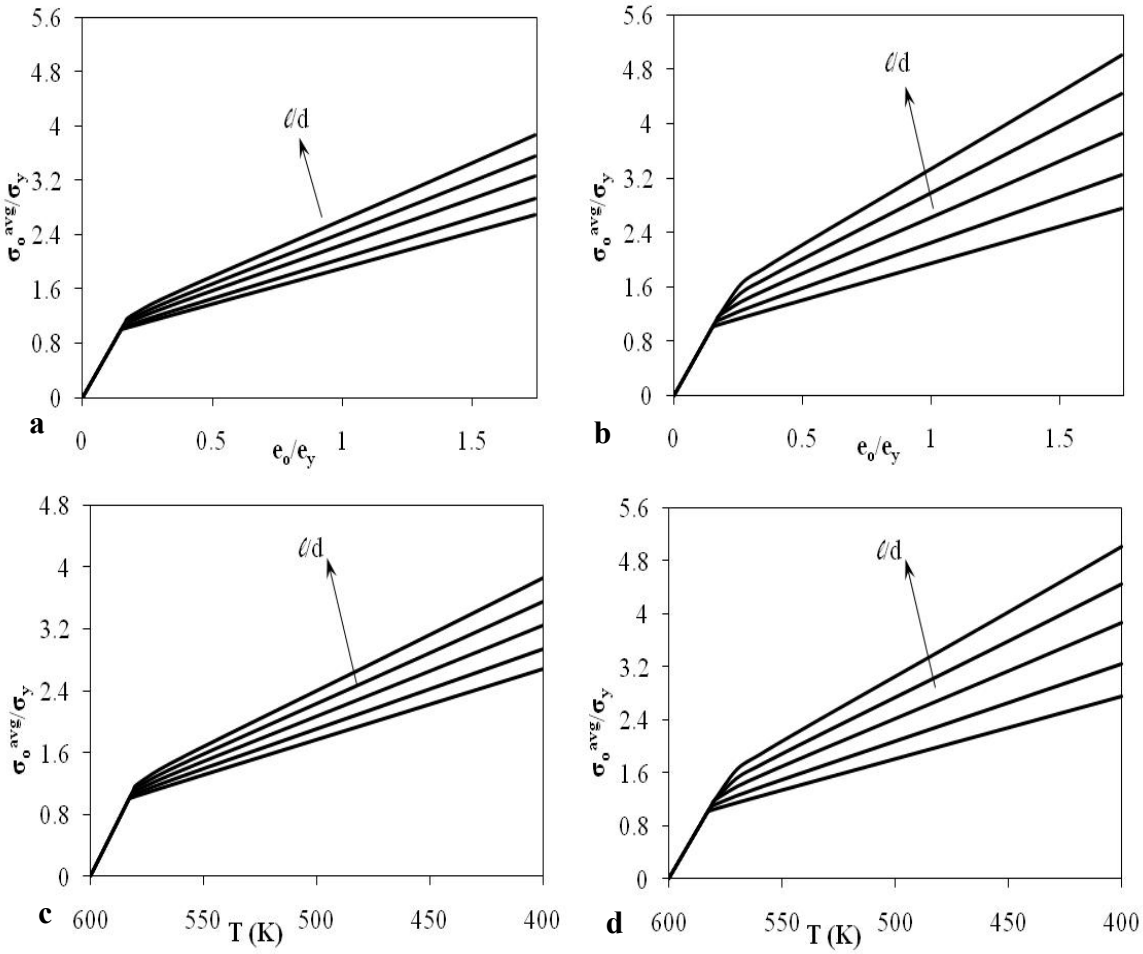

Fig. 3.15. Size effect in stress-strain relationship (a and b) and stress-temperature relationship (c and d) under thermal loading due to interfacial yield strength and hardening $\delta = 0.45$ for (a,c) and $\delta = 1$ for (b,d)

In Figure 3.16, the plastic strain distribution and total stress distribution across the film thickness is plotted. Varying interfacial yield strength and hardening both impart size effects in the plastic strain profile across the thickness while it is more pronounced in case of stiffer and harder interfaces marked by higher δ value.

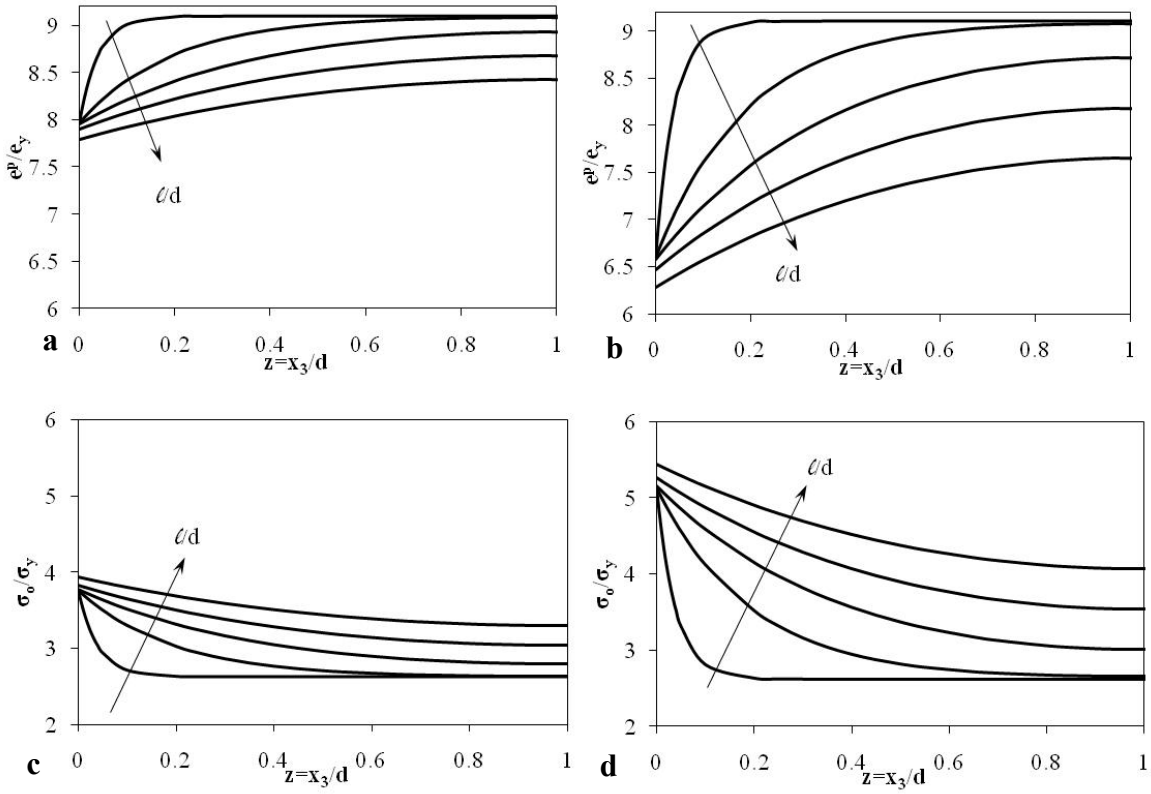

Fig. 3.16. Size effects in normalized plastic strain and total stress distributions due to interfacial yield strength and interfacial hardness $\delta = 0.45$ for (a,c) and $\delta = 1.0$ for (b,d)

CHAPTER IV

INDENTATION SIZE EFFECT MODELS AND MATERIAL INTRINSIC LENGTH SCALE: AN ANALYTICAL APPOACH

4.1 Introduction

In the attempt of evaluating material mechanical properties (e.g. hardness, stiffness) at small scales, micro- and nano- indentation tests proves to be most suitable for their economic as well as fast, precise and nondestructive merit. However there are numerous indentation tests at scales on the order of a micron or a submicron level that have shown that the measured hardness increases significantly with decreasing the indentation size or equivalently the indenter size (e.g. Stelmashenko et al., 1993; DeGuzman et al., 1993; Ma and Clarke, 1995; Poole et al., 1996; McElhaney et al., 1998; Lim and Chaudhri, 1999; Elmustafa and Stone, 2002; Gerberich et al., 2002; Swadener et al., 2002; Huber et al., 2002; Abu Al-Rub and Voyiadjis, 2004a). This phenomenon is commonly termed as indentation size effect (ISE).

It has already been discussed in the preceding chapters that indentation size effect or any form of size scale effects in general could not be explained by the classical continuum mechanics, whereas gradient plasticity theory has been successful in addressing the size effect phenomena. This is due to the incorporation of a micro-structural length scale parameter in the governing equation of the deformation description. Gradient plasticity theory attributes ISE to the evolution of the so-called

geometrically necessary dislocations (GNDs) beneath the indenter, which gives rise to strain gradients (Ashby, 1970; Arsenlis and Park, 1999).

By considering the GNDs generated by a conical indenter, Nix and Gao (1998) utilized the dislocation arguments set by Stelmashenko et al. (1993) and Ma and Clarke (1995) and developed an ISE model that suggests a linear dependence of the square of the micro-hardness to the inverse of the indentation depth. Swadener et al. (2002) utilized the basic precepts given by Nix and Gao (1998) for a conical indenter and developed an ISE model for spherical indenters which suggests a linear dependence of the square of the micro-hardness to the inverse of the diameter of the spherical indenter. However, recent micro- and nano-indentation results show that the predictions of the Nix-Gao and Swadener et al. models deviate significantly from the experimental results at small indentation depths (i.e. nano-indentation) in the case of Berkovich and Vickers indenters (e.g. Lim and Chaudhri, 1999; Saha et al., 2001; Elmustafa and Stone, 2002; Feng and Nix, 2004; Abu Al-Rub and Voyiadjis, 2004a; Manika and Maniks, 2006; Abu Al-Rub, 2007) and at small diameters for the case of spherical indenters (Swadener et al. 2002; Abu Al-Rub and Voyiadjis, 2004a). Moreover, Elmustafa and Stone (2002) observed that when the Nix-Gao model is used to fit the experimental results of micro- and nano-hardness, the data at deep indents (micro-hardness) exhibits a straight-line behavior whereas for shallow indents (nano-hardness) the slope of the line severely changes, decreasing by a factor of 10, resulting in a bilinear behavior and, therefore, two different values for the material length scale are used to fit the micro- and nano-indentation data. Recently, Huang et al. (2006) modified the Nix-Gao model by reducing

the density of GNDs at small indentation depths where two values for the material length scale are also used to fit the micro- and nano-indentation data. Therefore, Nix-Gao model can fit well either the hardness data from micro-indentation or nano-indentation tests, but not both simultaneously. The same can be said about Swadener et al. (2002) ISE model for spherical indenters.

Recently, Abu Al-Rub (2007) and Abu Al-Rub and Faruk (2010) argued that the most likely impediment in both the Nix and Gao (1998) and Swadener et al. (2002) ISE models is the assumption that the densities of GNDs and SSDs in the Taylor's hardening law (Taylor, 1938) are summed arithmetically such that it underestimates the total dislocation density underneath a conical/pyramidal indenter. It was concluded that it is better to postulate the total shear stresses as the arithmetic sum of shear stresses from SSDs and that from GNDs. This conclusion is used in this chapter in order to formulate two new ISE models for conical and spherical indenters as compared to those by Nix and Gao (1998) and Swadener et al. (2002) respectively. Moreover, some insight are shed on the interpretation of the ISE encountered in micro- and nano-hardness from indentation tests and an ISE analytical model is proposed that *can predict equivalently well the micro- and nano-indentation hardness data* from both conical and spherical indentation. The predictions of this model are compared to that by Swadener et al. (2002) against a set of micro-indentation tests on several metallic materials from the literature. Values for the material length scale parameter are calculated and it is shown that these values vary with the plastic strain for a certain material.

4.2 Strain Gradient Plasticity Theory and Coupling between SSDs and GNDs

Plastic strain gradients play an essential role in the prediction of size-scale effects in the deformation behavior of metals at the micron and submicron scales. Strain gradient plasticity theories extend the classical plasticity models by explicitly including an intrinsic material length scale and by including the history effects of the surrounding material points on the material point under consideration (i.e. nonlocality), and are therefore appropriate for materials and structural systems involving small dimensions. Many researchers tend to write the weak form of the non-local conventional effective plastic strain, $\widehat{\varepsilon}^{p}$, which is the conjugate variable of the plasticity isotropic hardening, in terms of its local counterpart, ε^{p}, and the corresponding higher-order gradients, η. The coupling between $\widehat{\varepsilon}^{p}$ and η was presented in many different mathematical forms by Abu Al-Rub and Voyiadjis (2004a, 2004b). Motivated by the Taylor's hardening law at the micro-mechanical level, one can assume the following power-law of the corresponding gradient-dependent flow stress at the mesoscale (Abu Al-Rub, 2007):

$$\sigma = \sigma_{ref}\left(\widehat{\varepsilon}^{p}\right)^{1/n} \quad \text{with} \quad \sqrt{\widehat{\varepsilon}^{p}} = \sqrt{\varepsilon^{p}} + \sqrt{\ell\eta} \tag{4.1}$$

where σ can be set equal to the effective (or equivalent) stress, for example, $\sigma = \sqrt{3 s_{ij} s_{ij} / 2}$ in case of von Mises-type plasticity, where $s_{ij} = \sigma_{ij} - \frac{1}{3}\sigma_{kk}\delta_{ij}$ is the deviatoric part of the Cauchy stress tensor σ_{ij} with δ_{ij} designates the Kronecker delta. The reference stress σ_{ref} is a measure of the yield strength in uniaxial tension, ℓ is the material length scale where its physical meaning and origin will be explored in the following developments, $n \geq 1$ is the strain-hardening exponent, and η is an effective

measure of the gradient of plastic strain which is related to the GND density. For example, one can assume $\eta = \sqrt{\nabla_k \varepsilon^p . \nabla_k \varepsilon^p}$, where ∇_k is the first-order gradient operator. For other expressions of η, one can consult Abu Al-Rub and Voyiadjis (2004a).

It is assumed, in general, that the total dislocation density represents the total coupling between two types of stored dislocations which play a significant role in the hardening mechanism of small scale metallic systems; namely: statistically stored dislocations (SSDs) and geometrically necessary dislocations (GNDs) (Nye, 1953; Ashby, 1970; Arsenlis and Parks, 1999). SSDs are generated by trapping each other in a random way while GNDs relieve the plastic deformation incompatibilities within the polycrystal caused by non-uniform dislocation slip. GNDs cause additional storage of defects and increase the deformation resistance by acting as obstacles to SSDs. Furthermore, the density of SSDs, ρ_S, depends on the local effective plastic strain, ε^p, while the density of GNDs, ρ_G, is directly proportional to the gradient of the effective plastic strain, $\nabla_k \varepsilon^p$ (Ashby, 1970); thus, introducing nonlocality. The densities ρ_S and ρ_G can be combined in various ways for which, unfortunately, there is a little guidance from dislocation mechanics until now. Mughrabi (2001) concluded that the simple superposition of the density of GNDs on the density of SSDs (i.e. $\rho_T = \rho_S + \rho_G$) is not well founded and they are unambiguously related. Abu Al-Rub and Voyiadjis (2004a, 2004b), Voyiadjis and Abu Al-Rub (2005), and Abu Al-Rub (2007) presented different phenomenological forms to enhance the nonlinear coupling between SSDs and GNDs.

They have concluded that the most likely impediment in the Nix and Gao (1998) model in predicting nano-hardness from conical/pyramidal indenters is due to the assumption that the total dislocation density, ρ_T, in the Taylor's hardening law is a simple arithmetic sum of both SSD and GND densities. One possible coupling can be assessed by writing the overall flow stress, σ, as follows:

$$\sigma = \left[\sigma_S^{\beta} + \sigma_G^{\beta} \right]^{1/\beta} \tag{4.2}$$

where the interaction coefficient β is considered as a material constant and used to assess the sensitivity of predictions to the way in which the coupling between the SSDs and GNDs is enhanced during the plastic deformation process. The general form in Eq. (4.2) ensures that $\sigma \rightarrow \sigma_S$ whenever $\sigma_S >> \sigma_G$ (i.e. classical plasticity) and that $\sigma \rightarrow \sigma_G$ whenever $\sigma_S << \sigma_G$. The stresses σ_S and σ_G are associated respectively with the densities of SSDs and GNDs through the Taylor's hardening law (Taylor, 1938) as follows:

$$\sigma_S = m\alpha Gb\sqrt{\rho_S}\,, \quad \sigma_G = m\alpha Gb\sqrt{\rho_G} \tag{4.3}$$

where m is the Taylor's factor, which acts as an isotropic interpretation of the crystalline anisotropy at the continuum level such that $m = \sqrt{3}$ for an isotropic solid and $m = 3.08$ for FCC polycrystalline metals (Taylor, 1938), G is the shear modulus, b is the magnitude of Burgers vector, and α is a statistical coefficient between 0.1 and 0.5.

Substituting Eqs. (4.3) into Eq. (4.2), one can express the total dislocation density, ρ_T, as follows:

$$\rho_T = \left[\rho_S^{\beta/2} + \rho_G^{\beta/2} \right]^{2/\beta} \tag{4.4}$$

such that the flow stress σ in Eq. (4.2) can be rewritten as

$$\sigma = m\alpha Gb\sqrt{\rho_T} \tag{4.5}$$

However, recently, Abu Al-Rub (2007) has shown that the real situation in experiments suggests that ρ_T cannot be taken as a simple sum of the densities of SSDs and GNDs (i.e. for $\beta = 2$) and that the total dislocation density under indentation is larger than this simple sum. In fact, for $\beta < 2$ in Eq. (4.4), ρ_T is larger than the arithmetic sum of SSD and GND densities, whereas for $\beta > 2$, ρ_T is smaller than the sum. Therefore, β either increases the effect of both kinds of dislocations or decreases such effect. However, Ashby (1970) has pointed out that in general the presence of GNDs will accelerate the rate of SSDs storage and that an arithmetic sum of their densities gives a lower limit on ρ_T, which implies that β should be less than 2. In fact, Abu Al-Rub (2007) has concluded after analyzing several micro- and nano-hardness data from indentation by conical/pyramidal indenters that $\beta \approx 1$ in Eq. (4.4). In other words, Abu Al-Rub (2007) has concluded that a simple arithmetic *sum of the flow stresses from the densities of SSDs and GNDs* is a better assumption than the simple sum of the densities of SSDs and GNDs. Hence, by setting $\beta = 1$ in Eq. (4.2), one can rewrite the total flow stress as follows:

$$\sigma = \sigma_S + \sigma_G \tag{4.6}$$

This along with Eq. (4.4) leads to a coupling between SSD and GND densities of the form,

$$\sqrt{\rho_T} = \sqrt{\rho_S} + \sqrt{\rho_G} \tag{4.7}$$

which differs from the linear coupling of the form,

$$\rho_T = \rho_S + \rho_G \tag{4.8}$$

adopted in formulating the Nix-Gao and Swadener's models. Eq. (4.7) gives a total dislocation density larger than that given by $\rho_T = \rho_S + \rho_G$. In the following subsequent developments, Eqs. (4.1), (4.3), and (4.6) will be utilized to formulate an ISE model and in exploring the physical origin of the material length scale parameter responsible for the observed size-scale effects.

4.3 Physical Interpretation of the Intrinsic Material Length Scale

The full utility of the strain gradient plasticity theories hinges on one's ability to determine the constitutive length scale parameter, ℓ, which scales the gradient effect. In this section, the physical intepretation of ℓ is identified. The study of Begley and Hutchinson (1998), Yuan and Chen (2001), Abu Al-Rub and Voyiadjis (2004a, 2004b), Abu Al-Rub (2007) and Abu Al-Rub and Faruk (2010) indicated that micro- and nano-indentation may be the most effective test for measuring the length scale parameter. However, the physical origin of ℓ based on dislocation mechanics has not been discussed until the work of Abu Al-Rub and Voyiadjis (2004a, 2004b). In fact, Abu Al-Rub and Voyiadjis (2004a, 2004b) have shown based on dislocation mechanics that ℓ is proportional to the average spacing between dislocations (or the mean free path for

dislocation motion). This met to a great extent the phenomenological arguments by Nix and Gao (1998) and Gao et al. (1999) that ℓ may be interpreted physically as the square of dislocation spacing over the magnitude of the Burgers vector. However, they proposed an expression for ℓ as a function of the magnitude of the Burgers vector multiplied by square of the ratio of the shear modulus to the yield strength and other empirical parameters. This expression yields a constant value for ℓ for a specific material and is independent of the material micro-structural features. Whereas, the study of Abu Al-Rub and Voyiadjis (2004a) and Voyiadjis and Abu Al-Rub (2005) have indicated that this length scale parameter is not a constant for a given material but since it depends on the spacing between dislocations is deformation dependent. In other words, as the plastic strain increases, the smaller is the length scale and the weaker is the size effect. Also, Voyiadjis and Abu Al-Rub (2005) proposed a phenomenological expression for ℓ in terms of: (a) the average grain size in polycrystalline materials or the particle size in composite materials with dispersed hard particles, (b) the geometric characteristic size such as the thickness of a thin film, radius of a thin wire, or inter-particle spacing in particulate composites, (c) the magnitude of the plastic strain, and (d) the rate of strain-hardening (annealed versus work-hardened or pre-deformed materials).

During plastic deformation, the density of SSDs increases due to a wide range of processes that leads to production of new dislocations. Those new generated dislocations travel on a background of GNDs which act as obstacles to the SSDs. If L_S is the average distance traveled by a newly generated dislocation, then the rate of accumulation of strain due to SSDs scales with $\dot{\varepsilon}_e^p \propto L_S b \dot{\rho}_S$ (Orowan, 1948) such that for proportional

loading and monotonically increasing plasticity, one can express ε^p in terms of ρ_S as (Abu Al-Rub and Voyiadjis, 2004a, 2004b):

$$\varepsilon^p = \frac{1}{m} b L_S \rho_S \tag{4.9}$$

On the other hand, Ashby (1970) and Arsenlis and Parks (1999) showed that gradients in the plastic strain field are accommodated by the GND density, ρ_G, such that the effective plastic strain gradient η that appears in Eq. $(4.1)_2$ can be defined as follows:

$$\eta = \frac{\rho_G b}{\bar{r}} \tag{4.10}$$

The constant $\bar{r} \approx 2$ is the Nye's factor introduced by Arsenlis and Parks (1999) to reflect the scalar measure of GND density resultant from mesoscopic plastic strain gradients.

Now, substituting ρ_S from Eq. (4.9) and ρ_G from Eq. (4.10) into Eq. (4.7) and then in Eq. (4.5), and comparing the result with Eq. $(4.1)_1$ after substituting Eq. $(4.1)_2$ yields the following expression for the intrinsic material length scale ℓ in term of the mean free path of dislocations or the mean spacing between dislocations, L_S, such that

$$\ell = \Gamma L_S \quad \text{with} \quad \Gamma = \bar{r}/m \tag{4.11}$$

which also gives σ_{ref} as

$$\sigma_{ref} = G\sqrt{\alpha^2 m^3 b / L_S} \tag{4.12}$$

The micro-structural length scale parameter, ℓ, and the phenomenological measure of the yield stress in uniaxial tension, σ_{ref}, are now related to measurable physical parameters. It appears from Eq. $(4.11)_1$ that the size effect and its implications on the flow stress and work-hardening in metals is fundamentally controlled by the dislocation glide, which depends on the course of deformation and the material's microstructural features. If one assumes $m \approx 2$ and $\bar{r} \approx 2$ then $\ell \approx L_S$, which can be experimentally measured. Therefore, L_S is a crucial physical measure that controls the evolution of the length scale in gradient plasticity theory for metals such that the key feature of plastic deformation is the reduction of the free path, cell size, or spacing between dislocations with deformation, material's microstructure, and size of the structural system.

By substituting L_S from Eq. $(4.11)_1$ into Eq. (4.12), one obtains a relation for ℓ as a function of the shear modulus, yield stress, and other micro-structural parameters, such that:

$$\ell = m^2 \alpha^2 \bar{r} \left(G/\sigma_{ref} \right)^2 b \tag{4.13}$$

This agrees with the expression proposed by Nix and Gao (1998). If one sets $m = 3.08$, $\alpha = 0.3$, $b = 0.225\,\text{nm}$, G/σ_{ref} = 100, then $\ell = 3.8\,\mu\text{m}$ which is a physically sound value in the range of micrometers as reported by many authors in the Material Science community (e.g. Begley and Hutchinson, 1998; Nix and Gao, 1998; Stolken and Evans, 1998; Zhao et al., 2003; Abu Al-Rub and Voyiadjis, 2004a, 2004b).

4.4 Model for Hardness Indentation Size Effect

Indents with tip sizes exceeding tens of microns generally produce size-independent hardness values in most metals and can be considered as large indents. Smaller indents in the range from submicron to about $10\,\mu m$ in single crystals or fine-grained poly-crystals display a significant size effect. A clear understanding of the ISE and its connection with the material strength is especially important in modern applications involving thin films and multi-layers since micro- and nano-indentation are frequently the only means of measuring their mechanical properties.

In this section two simple analytical models that can be used to predict equivalently both micro- and nano-hardness when using conical or spherical indenters is proposed based on the concept of GNDs.

4.4.1 ISE model for the conical tipped indenters

Let us consider the indentation by a rigid cone, as shown schematically in Figure 4.1. One can assume that the density of GNDs is integrated by the geometry of the indenter and the indentation is accommodated by circular loops of GNDs with Burgers vectors normal to the plane of the surface. One can use the simple model of GNDs developed by Stelmashenko et al. (1993), DeGuzman et al. (1993), Nix and Gao (1998), Abu Al-Rub and Voyiadjis (2004b), and Abu Al-Rub (2007) to determine the density of GNDs evolved under a conical/pyramidal indenter. As the indenter is forced into the surface of a single crystal, GNDs are required to account for the permanent shape change at the surface. Of course, SSDs, not shown in Figure 4.1, would also be created and they would contribute to the deformation resistance.

The fundamental parameters for indentation tests by conical/pyramidal indenter are (see Figure 4.1): the force applied to the indenter, P, the residual contact radius of indentation, a_p, the hardness, $H_c = P/\pi a_p^2$, the permanent indentation depth, h_p, the total indentation depth, h, the plastic zone radius, c_p, and the indenter geometry; i.e. the angle between the surface of the conical indenter and the plane of the surface θ. This angle is related to h_p and a_p by $\tan\theta = h_p/a_p$ (see Figure 4.1). The subscript c in

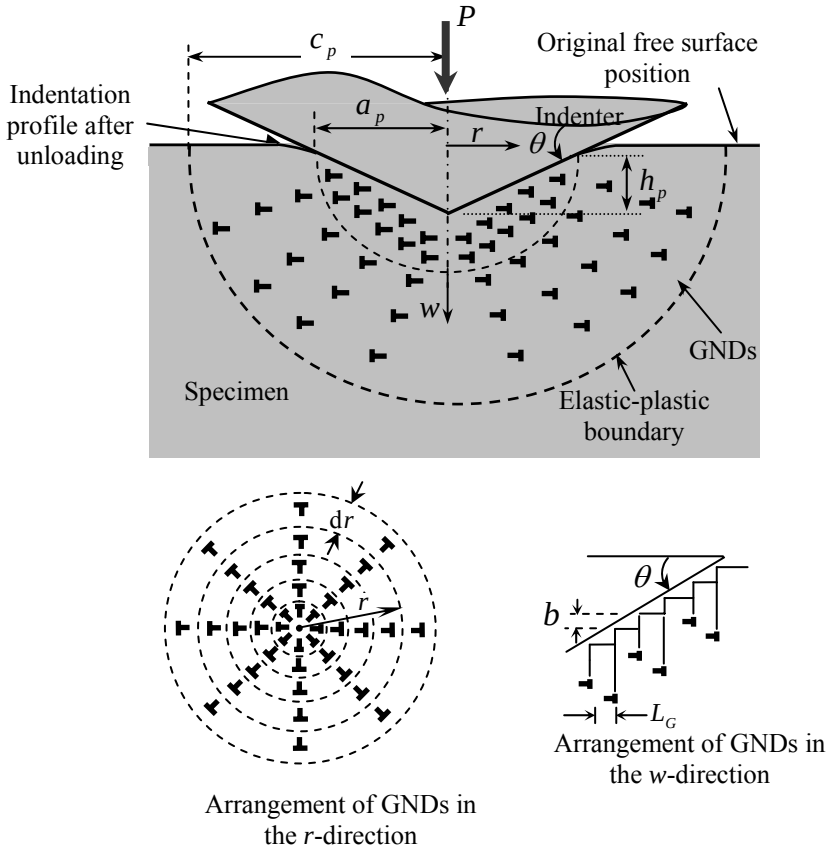

Fig. 4.1. Indentation by axisymmetric rigid conical indenter. Geometrically necessary dislocations created during the indentation process. The dislocation structure is idealized as circular dislocation loops

H_c indicates the hardness value from a conical indentation test. The unloading process in the indentation experiment is essential for the proper specification of these geometric parameters. Thus, the residual values h_p and a_p should be used as measurable data in the hardness H_c calculations.

The indentation profile in the unloaded configuration when using conical/pyramidal indenters can be described by (see Figure 4.1):

$$w(r) = h_p - r(\tan\theta) \quad \text{for} \quad 0 \le r \le a_p \tag{4.14}$$

It is assumed that the dislocation evolution during indentation is primarily governed by a large hemispherical volume V that scales with the contact radius a_p around the indentation profile (see Figure 4.1). However, the GNDs reside inside a plasticity zone which can be viewed as extending to a radius c_p to the outermost dislocation emanated from the indent core. Therefore, the size of the plastic zone, c_p, underneath the indenter is larger than the contact radius, a_p, as suggested by Feng and Nix (2004) and Durst et al. (2006) such that $c_p = f\, a_p$ where $f > 1$. Now, one can calculate the GND density using the following relation

$$\rho_G = \frac{\lambda}{V} \tag{4.15}$$

where λ is the total length of dislocation loops and V is the storage volume. From Figure 4.1, one can write:

$$\left|\frac{dw}{dr}\right| = \frac{b}{L_G} = \tan\theta = \frac{h_p}{a_p} \quad \Rightarrow \quad L_G = \frac{b a_p}{h_p} \tag{4.16}$$

where L_G is the mean spacing between individual slip steps on the indentation surface corresponding to the GND loops. If λ is the total length of the injected loops, then between r and $r+dr$ one can write:

$$\mathrm{d}\lambda = 2\pi r \frac{\mathrm{d}r}{L_G} = 2\pi r \frac{h_p}{ba_p}\mathrm{d}r \tag{4.17}$$

Integrating from 0 to c_p gives the total length of GND loops as:

$$\lambda = \int_o^{c_p} 2\pi r \frac{h_p}{ba_p}\mathrm{d}r = \int_o^{fa_p} 2\pi r \frac{h_p}{ba_p}\mathrm{d}r = \frac{\pi a_p h_p}{b} f^2 \tag{4.18}$$

One can then assume that all the induced GND loops remain within a net volume V which is calculated as the indentation volume ($\frac{1}{3}\pi a_p^2 h_p$) subtracted from the total hemispherical volume of radius c_p (i.e. $\frac{2}{3}\pi c_p^3$), such that:

$$V = \frac{2}{3}\pi\gamma f^3 a_p^3 \quad \text{with} \quad \gamma = 1 - \frac{1}{2f^3}\left(\frac{h_p}{a_p}\right) \tag{4.19}$$

Therefore, the density of GNDs from Eq. (4.15) becomes

$$\rho_G = \frac{3}{2fb\gamma h_p}\tan^2\theta \tag{4.20}$$

The GND density is reduced by using a bigger storage volume at small indentation depth. In reality the GND density cannot be very large because of the strong repulsive forces between GNDs which push dislocations to spread beyond the hemisphere at small indentation depth (Swadener et al., 2002).

Based on the assumption of a self-similar deformation field (Biwa and Storakers, 1995), it was shown that the displacement is proportional to the indentation depth h_p. Based on this observation, Xue et al. (2002) showed from numerical experiments that the strain field should depend only on the normalized indentation depth, h_p / a_p, such that one may assume that the effective plastic strain ε^p is defined by:

$$\varepsilon^p = c_c \left(h_p / a_p \right) = c_c \tan\theta \tag{4.21}$$

where c_c is a material constant which has a value of $c_c = 0.2$. It can be noted from Eq. (4.21) that the plastic strain is independent of the indentation depth. Considering Eqs. (4.9), (4.11), and (4.21) yields the following expression for the density of SSDs:

$$\rho_S = \frac{c_c \, \bar{r} \tan\theta}{\ell b} \tag{4.22}$$

Tabor (1951) specified the mapping from the $H - h_p$ curve to $\sigma - \varepsilon^p$ curve such that one can express the micro-/nano-hardness as:

$$H_c = \kappa\sigma = \kappa m \alpha b G \left[\sqrt{\rho_S} + \sqrt{\rho_G} \right] \tag{4.23}$$

where Eqs. (4.5)and (4.7) are used in obtaining the above expression. The parameter κ is the Tabor's factor, which has a value from 2.8 to 3.07. The Tabor's relation (i.e. $H = \kappa\sigma$) has been extensively verified and used by many authors in the literature and, therefore, one may indeed take it as a starting point.

The macro-hardness H_{oc} is defined as the hardness that would arise from SSDs alone in the absence of GNDs, that is, the hardness that corresponds to the saturation

value where the hardness H_c does not change as the indentation depth h_p increases, or that predicted by classical plasticity theory, such that one can write from Eq. (4.23):

$$H_{oc} = \kappa m \alpha b G \sqrt{\rho_S} \tag{4.24}$$

From Eqs. (4.23) and (4.24), the ratio, H_s / H_{os} can be written as,

$$\frac{H_c}{H_{oc}} = 1 + \sqrt{\frac{\rho_G}{\rho_S}} \tag{4.25}$$

substituting Eqs. (4.20) and (4.22) into Eq. (4.25), one can obtain the following ISE model:

$$\frac{H_c}{H_{oc}} = 1 + \sqrt{\frac{h^*}{h_p}} \tag{4.26}$$

where h^* and H_{oc} are, respectively, given by:

$$h^* = \zeta \ell \quad \text{with} \quad \zeta = \frac{3}{2 f \gamma c_c \bar{r}} \tan\theta \tag{4.27}$$

$$H_{oc} = \kappa \sigma_{ref} c_c^{1/n} \left(\tan\theta\right)^{1/n} \tag{4.28}$$

The parameter h^* is a material parameter that characterizes the depth dependence of the hardness and is proportional to the material length scale, ℓ, with a proportionality factor ζ which depends on the indenter geometry, θ, and the plastic flow through f, c_c, and $\bar{r}$. Thus, h^* is a crucial parameter that characterizes the ISE and its accurate experimental measure gives values for ℓ on which the ability of the strain gradient plasticity theory to guide the development of small scale systems depends on. Therefore, micro-/nano-indentation hardness data can be effectively used in calibrating the strain

gradient plasticity theory. Furthermore, one can note that Eq. (4.28) yields a size-independent and constant value of H_{oc}.

One can obtain the commonly used ISE model of Nix and Gao (1998) simply by assuming a linear coupling between SSD and GND densities as in Eq. (4.8) (i.e. by setting $\beta = 2$ in Eq. (4.4)) and assuming that all the GNDs are stored in a plastic zone of radius equal to the contact radius a_p (i.e. $f = 1$), such that:

$$\frac{H}{H_o} = \sqrt{1 + \frac{h^*}{h_p}} \tag{4.29}$$

Moreover, Nix and Gao (1998) suggested that h^* and H_o are dependent and related through $h^* = (81/2)b\alpha^2 \tan^2\theta (G/H_o)^2$. Their relation, thus, gives a similar argument to that of Eq. (4.27) which suggests that h^* is dependent on the shape of the indenter as well as on the material property.

The size of the plastic zone, c_p, in Eq. (4.19) can be calculated using the following well-established relation (e.g. Johnson, 1970; Kramer et al., 1999; Chiu and Ngan, 2002):

$$c_p = \sqrt{\frac{3P}{2\pi\sigma_y}} \tag{4.30}$$

Using $H_c = P/\pi a_p^2$ in the above expression to substitute P along with the use of $H_y = \kappa\sigma_y$ and $c_p = fa_p$ yields the ratio of plastic zone size to contact radius as $f = \sqrt{\frac{3}{2}\kappa H_c/H_y}$. Here, H_y is the hardness due to the initial yield stress σ_y. However,

$P/\pi c_p^2$ is observed experimentally to be roughly constant with respect to the indent size (Chiu and Ngan, 2002), and this means that H is roughly constant at $r = c_p$. This suggests that the indentation hardness near the elastic-plastic boundary is already approximately self-similar and is not affected by size dependent events at the indent core. Therefore, at $r = c_p$ one can set $H_c = H_y$, which gives the factor $f = \sqrt{\frac{3}{2}\kappa}$ such that f is constant. For example, substituting $\kappa = 3$ gives $f = 2.12$, which is in the range of the experimental values reported by Kramer et al. (1999), Feng and Nix (2004), and Durst et al. (2006). Moreover, Feng and Nix (2004) suggested a dependence of f on the indentation depth based on phenomenological aspects and not physical ones.

Now that the value of f is specified, the value of γ in Eq. $(4.19)_2$ can be calculated along with the use of Eq. (4.16) to be $\gamma \approx 1$, if one sets $\tan\theta = 0.358$, a commonly used value for a Berkovich and Vickers indenter. Therefore, $\gamma = 1.0$ will be assumed for the experimental comparisons in the following sections.

It is noteworthy that the present interpretation of the ISE is based on the evolution of the GNDs, while from time to time in the literature several important factors in experiments (e.g. interfacial friction, indenter pile-up or sink-in, loading rate, oxidation layer, etc.) have been thought to be responsible for the ISE. However, careful experimental studies by Xue et al. (2002) have excluded these factors from being completely responsible for the ISE.

4.4.2 ISE model for spherical tipped indenters

Let us now consider the indentation by a rigid sphere, as shown in Fig. 4.2. rocedures similar to those in section 4.4.1 can be used to develop the analytical model for predicting indentation hardness. The fundamental parameters for indentation tests by a spherical indenter are (see Fig. 2): the force applied to the indenter, P, the residual contact radius of indentation, a_p, the hardness, $H_s = P/\pi a_p^2$, the permanent indentation

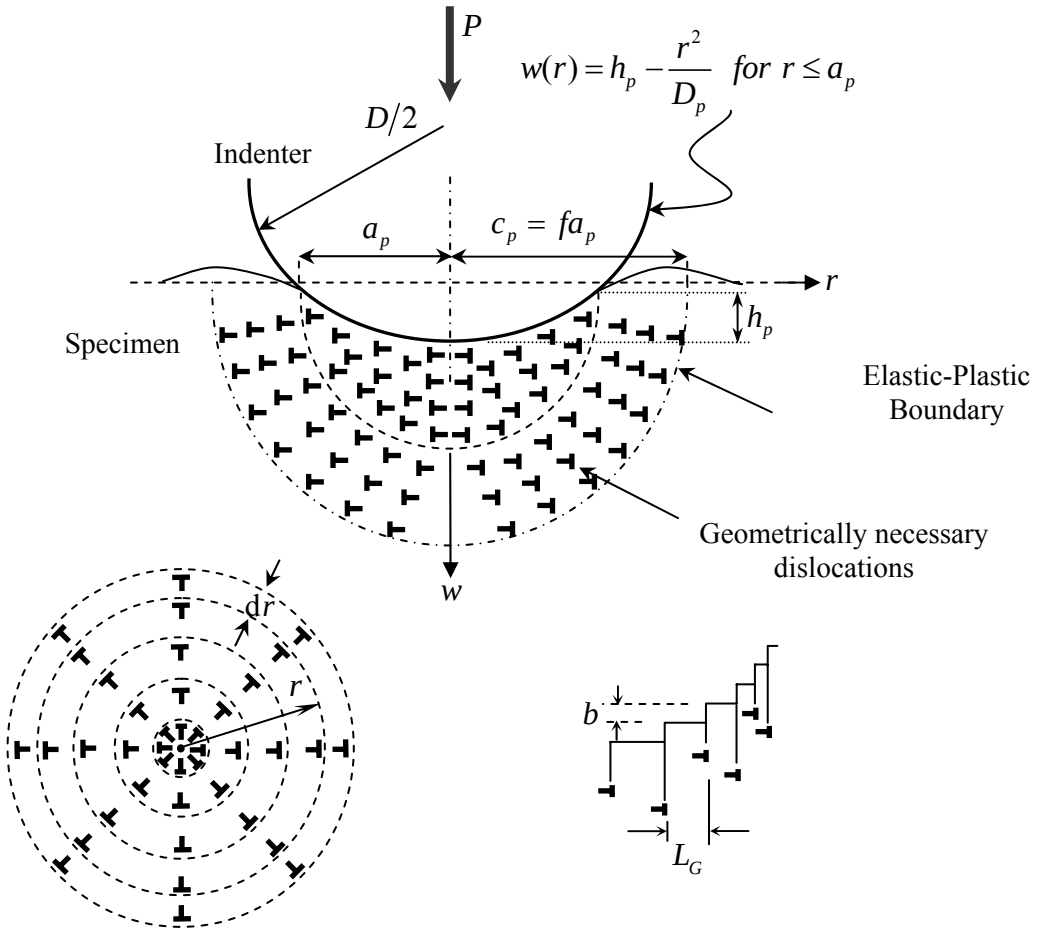

Fig. 4.2. Indentation by axisymmetric rigid spherical indenter. Geometrically necessary dislocations created during the indentation process. The dislocation structure is idealized as circular dislocation loops

depth, h_p, the total indentation depth, h, the residual indentation profile diameter, D_p, the plastic zone radius, c_p, which is scaled to a_p with a factor f such that $c_p = fa_p$, and the indenter geometry (i.e. the sphere diameter D). The subscript s in H_s indicates the hardness value from a spherical indentation test. Due to the importance of the unloading process for the proper specification of these parameters, h_p and a_p should be used as measureable data in the hardness, H_s calculation as well as the residual indentation profile diameter $D_p > D$ when using spherical indenter.

It can be assumed that the spherical indenter is approximated by a paraboloid and the indentation profile in the unloaded configuration can be described by:

$$w(r) = h_p - \frac{r^2}{D_p} \quad \text{for } 0 \le r \le a_p \tag{4.31}$$

where h_p, a_p, and D_p are measured in the unloaded configuration. By taking the slope of Eq. (4.31) and comparing it with Figure 4.2, one can easily show that:

$$\left|\frac{dw}{dr}\right| = \frac{2r}{D_p} = \frac{b}{L_G} \Rightarrow \quad L_G = \frac{bD_p}{2r} \tag{4.32}$$

where L_G is the mean spacing between the individual slip steps on the indentation surface corresponding to the GND loops. One can conclude from Eq. (4.32) that the GND loops are more closely spaced as one move away from the center of the spherical indenter in order to accommodate the geometric shape of the indenter.

Now, if λ is the total length of induced GND loops, then between r and $r + dr$ one has:

$$d\lambda = 2\pi r \frac{dr}{L_G} = 4\pi \frac{r^2}{bD_p} dr \tag{4.33}$$

which upon integrating over the radius of the plastic volume V (i.e. $c_p = f\, a_p$) gives:

$$\lambda = \int_0^{c_p} \frac{4\pi}{bD_p} r^2 dr = \frac{4\pi f^3 a_p^3}{3bD_p} \tag{4.34}$$

If one assumes that all the induced GND loops reside within the net volume V, which is calculated as the indentation volume ($\frac{1}{2}\pi a_p^2 h_p$) subtracted from the total hemispherical volume of radius c_p (i.e. $\frac{2}{3}\pi c_p^3$), such that:

$$V = \frac{2}{3}\pi\gamma f^3 a_p^3 \quad \text{with} \quad \gamma = 1 - \frac{3}{4f^3}\left(\frac{h_p}{a_p}\right) \tag{4.35}$$

Now, one can calculate the GNDs density using the following relation:

$$\rho_G = \frac{\lambda}{V} = \frac{2}{b\gamma D_p} \tag{4.36}$$

which shows that the density of GNDs is proportional to the inverse of the diameter of the spherical indenter.

Tabor's (1951) mapping for the $H - h$ curve to $\sigma - \varepsilon^p$ curve will be used here as well to assume the following mapping:

$$H_s = \kappa\sigma \quad , \quad \varepsilon^p = c_s \omega \tag{4.37}$$

where, c_s is a material constant with a value of $c_s = 0.4$ (Atkins and Tabor, 1965), and $\omega = a_p / D_p$ defines the ratio between the contact radius to the indenter diameter in the unloaded configuration. Thus, one can define the micro/nano-hardness

(i.e. size-dependent hardness), H_s, and macro-hardness (i.e. size-independent hardness), H_{os}, with the use of Eqs. (4.5)and (4.7), as follows:

$$H_s = \kappa m \alpha b G \left(\sqrt{\rho_S} + \sqrt{\rho_G} \right) \quad , \quad H_{os} = \kappa m \alpha b G \sqrt{\rho_S} \tag{4.38}$$

From the above equations, one can write the ratio of H_s / H_{os} as

$$\frac{H_s}{H_{os}} = 1 + \sqrt{\frac{\rho_G}{\rho_S}} \tag{4.39}$$

Considering Eqs. (4.9), (4.11), and $(4.37)_2$, yields the following expression for the density of SSDs:

$$\rho_s = \frac{c_s \bar{r} \omega}{\ell b} \tag{4.40}$$

Substituting Eqs. (4.36) and (4.40) into (4.39), yields:

$$\frac{H_s}{H_{os}} = 1 + \sqrt{\frac{a^*}{a_p}} \tag{4.41}$$

where

$$a^* = \varsigma \ell \quad \text{with} \quad \varsigma = \frac{2}{c_s \bar{r} \gamma} \tag{4.42}$$

By substituting Eq. (4.40) into Eq. $(4.38)_2$ along with Eq. (4.13), one can obtain a simple relation to estimate the macro-hardness H_{os} as follows:

$$H_{os} = \kappa \sigma_{ref} \sqrt{c_s \omega} \tag{4.43}$$

It can be noted that both Eqs. (4.41) and (4.43) in addition to $H_s = P / \pi a^2{}_p$ are functions of the residual contact radius, a_p. Therefore, Eq. (4.41) cannot be used alone

to characterize the indentation size effect noticed in hardness experiments with spherical indenters. However, Lim and Choudhri (1999) and Swadener et al. (2002) have shown experimentally that for indentation of material with spherical indenters of few micron tip radii, the indentation hardness systematically increases with residual contact radius a_p and decreases with the residual indentation profile diameter D_p. Lim and Choudhri (1999) and Swadener et al. (2002) tend to attribute the ISE to the different hardness values obtained for different spheres at the same value of the normalized contact radius $\omega = a_p / D_p$ (or equivalently at fixed effective plastic strain $\varepsilon^p = c\omega$). Therefore, by substituting $a_p = \omega D_p$ into Eq. (4.41), one obtains a relation that can characterize the ISE for a constant ω, such that:

$$\frac{H_s}{H_{os}} = 1 + \sqrt{\frac{D^*}{D_p}} \tag{4.44}$$

where D^* is a material specific parameter that characterizes the size dependence of hardness and depends on the indenter geometry as well as on the plastic flow such that it is given by:

$$D^* = \xi \ell \quad \text{with} \quad \xi = \frac{2}{c_s \bar{r} \gamma \omega} \tag{4.45}$$

Eq. (4.45) shows that D^* is a linear function of the length scale parameter ℓ. Thus, D^* is a crucial material parameter that characterizes the indentation size effect and its accurate experimental measure using spherical indenters yields a reasonable value for the intrinsic material length scale parameter in the strain gradient plasticity theory.

By assuming that both SSDs and GNDs are coupled in a linear sense (i.e. $\rho_T = \rho_S + \rho_G$), Swadener et al. (2002) proposed the following ISE model:

$$\frac{H}{H_o} = \sqrt{1 + \frac{D^*}{D_p}} \tag{4.46}$$

It is noteworthy that the expression for γ in Eq. $(4.35)_2$ can be expressed in terms of ω by adapting the following relations between a_p, h_p, and D_p proposed by Kucharski and Mroz (2001):

$$a_p = \sqrt{q^2 D_p h_p} \quad \text{with} \quad q^2 = 2.5\left(\frac{2n-1}{4n+1}\right) \tag{4.47}$$

where q^2 is a constant that depends on the strain hardening exponent n and is mostly on the order of 1.0. Therefore, by substituting Eq. (4.47)1 into Eq. $(4.35)_2$, one can rewrite the expression for γ in terms of $\omega = a_p / D_p$ as follows:

$$\gamma = 1 - \frac{3\omega}{4 f^3 q^2} \tag{4.48}$$

Then, if one takes the value of f from the calculations of section 4.4.1, $f = 2.12$ along with $n = 2$, and $\omega = 0.05$, which are typical values for a metal, one obtains from Eq. (4.48) $\gamma \approx 1.0$. Therefore, $\gamma = 1.0$ will be assumed in the experimental comparisons in Chapter V.

4.5 Correlation between Length Scales Obtained by Conical and Spherical Indentation Tests

The preceding sections describe size effect models for conical and spherical indentation tests and how they can be used to measure the material intrinsic length scale parameter. In this section the length scales measured using this two approaches are compared and a relationship between them are established. For investigating this one can start with rewriting the expression of effective plastic strain in Eq (4.9), such that, for conical indenters,

$$\varepsilon_{con}^{p} = \frac{1}{m} b L_{CS} \rho_{CS} \tag{4.49}$$

And for spherical indenters,

$$\varepsilon_{sph}^{p} = \frac{1}{m} b L_{SS} \rho_{SS} \tag{4.50}$$

Where, L_{CS} and L_{SS} are mean free path between the SSDs for conical and spherical indenters respectively and b is the magnitude of Burgers vector. Recalling that, material length scale is equal to the mean free path between dislocations and assuming that, it is inversely proportional to the square root of SSD densities (i.e. $L_S \propto 1/\sqrt{\rho_S}$) one obtains

$$\frac{\varepsilon_{con}^{p}}{\varepsilon_{sph}^{p}} = \frac{\ell_S}{\ell_C} \tag{4.51}$$

Where, ℓ_S and ℓ_C are length scales obtained by spherical and conical indentation tests respectively. Now, according to Eqs. (4.21) and (4.37) the effective plastic strains are also defined as,

$$\varepsilon_{con}^{p} = c_C \tan\theta \tag{4.52}$$

And,
$$\varepsilon_{sph}^{p} = c_S \omega \tag{4.53}$$

Therefore, one obtains from the above three equations,

$$\frac{\ell_S}{\ell_C} = \frac{c_C \tan\theta}{c_S \omega} \tag{4.54}$$

Thus for known values of $\tan\theta$, ω, c_C and c_S (According to Atkins and Tabor, 1965 taken to be $c_C = 0.2$ and $c_S = 0.4$) a simple relation between the length scales determined by two test methods is obtained.

Furthermore, from the definitions of macro hardness in Eqs. (4.28) and (4.43) along with Eq. (4.54), one obtains,

$$\frac{\ell_S}{\ell_C} = \chi^n \quad \text{with,} \quad \chi = H_{oc}/H_{os} \tag{4.55}$$

The preceding formulations can be used to establish a correlation between the indentation size effect models, Eqs. (4.26) and (4.44) by equating the depth of conical indenter and the diameter of the spherical indenter that produce the same hardness value to be,

$$D_p = \frac{D^*}{\left[\chi\left(1+\sqrt{h^*/h_p}\right)-1\right]^2} \tag{4.56}$$

While, Eqs. (4.27) and (4.42) yield the relation between D^* and h^* to be

$$D^* = \frac{4f}{3}\left(\frac{c_C}{c_S \omega}\right)^2 h^* \tag{4.57}$$

Using Eq. (4.57) into Eq. (4.56), one obtains,

$$D_p = \frac{\frac{4f}{3}\left(\frac{c_C}{c_S \omega}\right)^2}{\left[(\chi - 1)/\sqrt{h^*} + \chi/\sqrt{h_p}\right]^2} \tag{4.58}$$

The above relation can be used to bring the hardness values measured with a pyramidal indenter into the range of the spherical data by knowing the calibrated h^* value.

CHAPTER V

INDENTATION HARDNESS: COMPARING MODELS WITH EXPERIMENTAL DATA

5.1 Introduction

In Chapter IV, analytical models were developed for predicting indentation size effects for conical and spherical indenters based on dislocation density conceptions. In this chapter, the proposed models are validated against several micro- and nano-indentation experimental data obtained from available literature. Presently, Nix-Gao (1998) model and Swadener et al. (2002) model are most commonly used to predict the micro- and nano-indentation hardness of metals in case of conical and spherical indenters respectively. Therefore, it is interesting to compare the predictions from these two models, and the two proposed models, Eqs. (4.26) and (4.44).

5.2 Data from Indentation Test with Conical Indenters

In this section, comparisons are made between the predictions of the present ISE model in Eq. (4.26) and that of Nix-Gao model in Eq. (4.29) with several micro- and nano-indentation data from the literature. The experimental data reported by Swadener et al. (2002) on annealed iridium, annealed and work hardened oxygen free copper (OFC), by Zhang et al. (2005) on undeformed and pre-strained Ni, by Kim et al. (2008) on undeformed and pre-strained SCM21 (structural steel), and by Zong et al. (2006) on LIGA Ni, (001)Ni, (001)Ag, and (001)Au are utilized here to conduct this comparison.

The experimental hardness data obtained from nano- and micro-indentations using, respectively, Berkovich and Vickers indenters are plotted in Figures 5.2(a-g) and 5.3(a-g) as the hardness H_c versus the indentation depth h_p.

All the experiment data used here in validating the proposed model, Eq.(4.26), are conducted at room temperature and using a Berkovich or Vickers pyramidal indenters for which the nominal or projected contact area varies as:

$$A_c = 24.5h^2 = \pi a^2 \tag{5.1}$$

Using this relation together with $\tan\theta = h_p / a_p$ yields:

$$\tan\theta = \sqrt{\frac{\pi}{24.5}} = 0.358 \tag{5.2}$$

The characteristic form for the ISE presented by Eq. (4.26) gives a straight line when the hardness data are plotted as H_c/H_{oc} versus $1/\sqrt{h_p}$, the intercept of which is 1 and the slope is $\sqrt{h^*}$. Taking a square of the slope of this curve gives the parameter h^*. For example, this fitting procedure is presented in Figure 5.1(a) using Eq. (4.26) by plotting the LIGA Ni hardness data of Zong et al. (2006) which yields $h^* = 0.079\,\mu\text{m}$. The macroscopic hardness $H_{oc} = 1.892\,\text{GPa}$ is obtained when the hardness curve reaches plateau at large indentation depths [see Figure 5.2(d)]. It can be seen from Figure 5.1(a) that the proposed model fits very well both the micro- and nano-indentation hardness data. Nix and Gao (1998) proposed plotting their model in Eq. (4.29) as $(H/H_o)^2$ versus $1/h$, which should result in a straight line with slope h^*. Figure 5.1(b) fits well

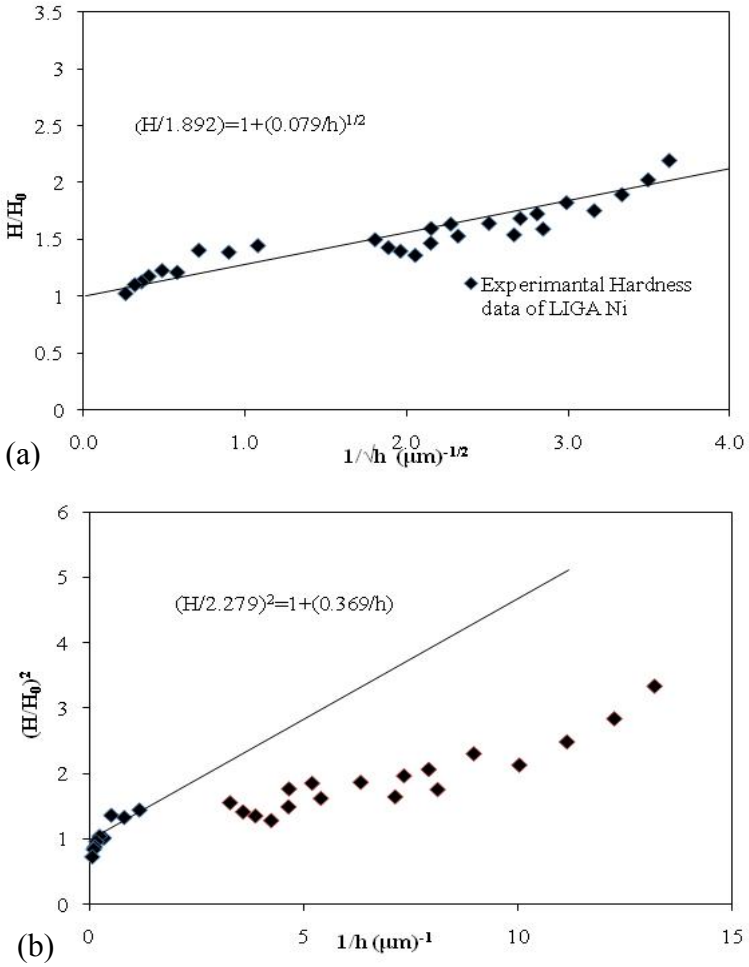

Fig. 5.1. The fitting procedures for both (a) the present model, Eq. (4.26), and (b) the Nix and Gao (1998) model, Eq. (4.29). The solid line is a linear curve fit of the experimental hardness results for LIGA Nickel by Zong et al. (2006)

only the micro-indentation hardness data with $H_o = 2.279\,\text{GPa}$ and $h^* = 0.369\,\mu\text{m}$, but significantly overestimates the nano-indentation hardness data [see Figure 5.2(d)].

The fitting procedures as described above for both the present model and the Nix-Gao model are repeated for the remaining hardness data of Swadener et al. (2002), Zhang et al. (2005), Kim et al. (2008), and Zong et al. (2006). In Figures 5.2(a-g) data from micro- and nano- indentation tests on annealed Ir, annealed OFC, work hardened

OFC, Liga Ni, (001)Ni, (001) Ag, and (001)Au are presented respectively to show the comparisons between the predictions of the present model, Eq. (4.26), and the Nix-Gao model, Eq. (4.29). Whereas, figures 5.3(a-g) shows similar fittings of nano-indentation data from undeformed and pre-strained Ni and undeformed and pre-strained SCM21. The values of H_{oc} and h^* used to fit the experimental results in each case are shown in the figures.

In case of Figures 5.2(a-g), both micro- and nano-indentation test data are analyzed and it can be seen that the present model predictions agree well with both the micro- and nano-hardness data, while the predictions of the Nix-Gao model diverge significantly from the nano-hardness results for $h < 1\mu m$. Moreover, despite the fact that results for indentation depths less than 100 nm are affected by tip rounding, the proposed model fits well both micro- and nano-hardness data although this effect is not considered in formulating the present model. However, it is shown in Huang et al. (2006) that the indenter tip radius effect alone cannot explain the nano-indentation size effect such that the ISE models of Qui et al. (2001), Xue et al. (2002), and Qu et al. (2004), which incorporate this effect, provide only marginal improvements.

Figures 5.3(a-g) are plotted using data analyzed from nano-indentation tests only and, as expected, both the models give good predictions of the experimental values. Although it can be noticed that in general, the present model slightly over-predicts the hardness at large indentation depths, because the ISE from the present model does not progressively vanish as fast as the experimental data. This is due to the fact that hardness data at larger indentation depths should also be measured in order to accurately identify

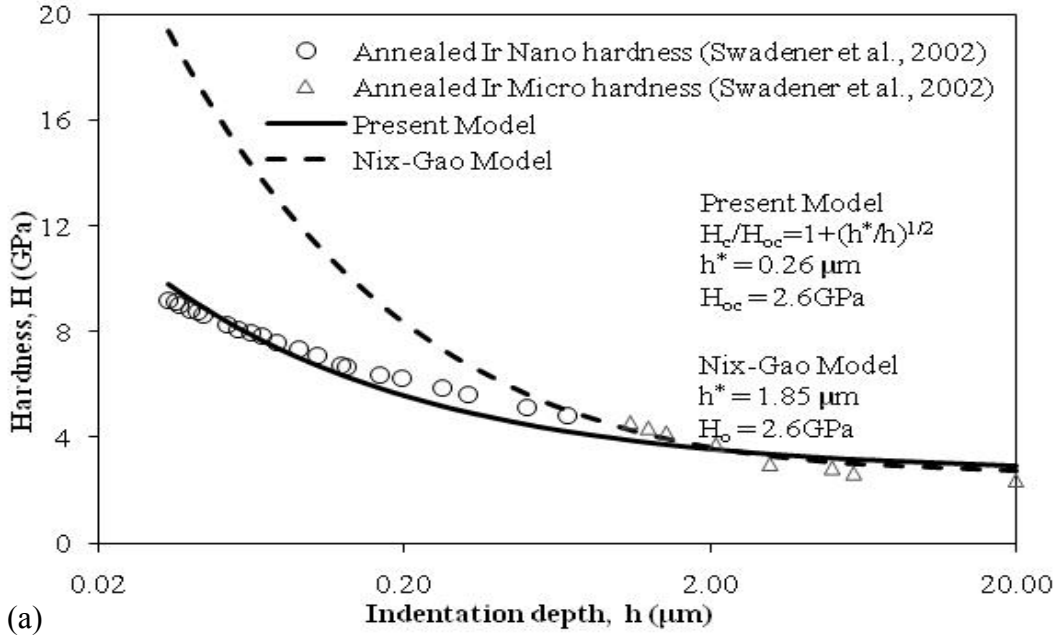

(a)

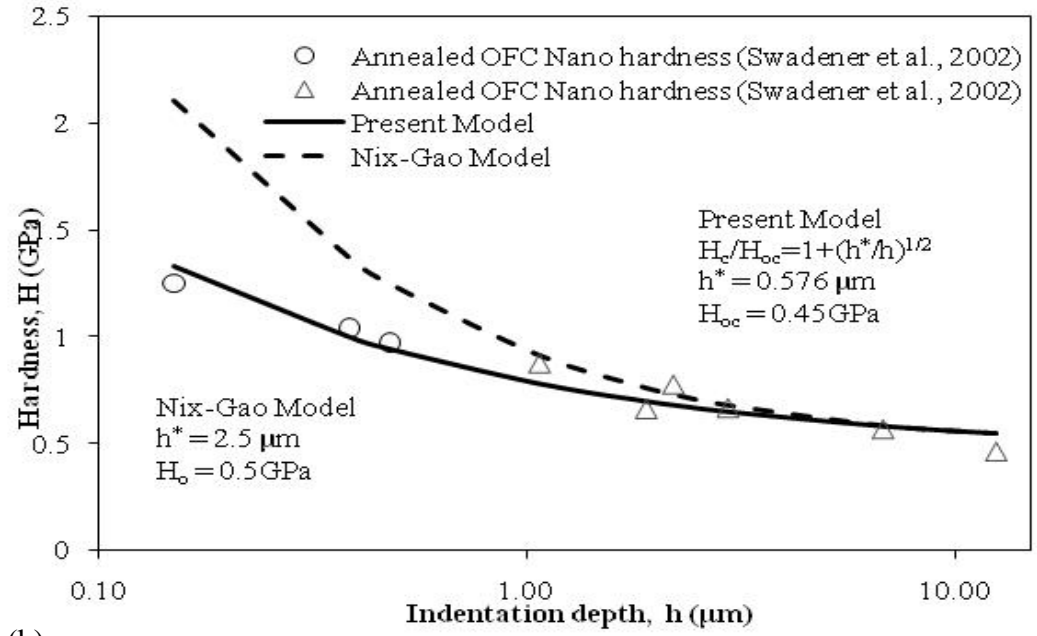

(b)

Fig. 5.2. Comparison of fit of the proposed model and Nix-Gao model to the experimental data: (a) Annealed Ir, (b) annealed OFC, (c) work hardened OFC, (d) LIGA Ni, (e) (001) Ni, (f) (001) Ag, (g) (001) Au. The symbols Δ and O designate micro-hardness and nano-hardness data, respectively

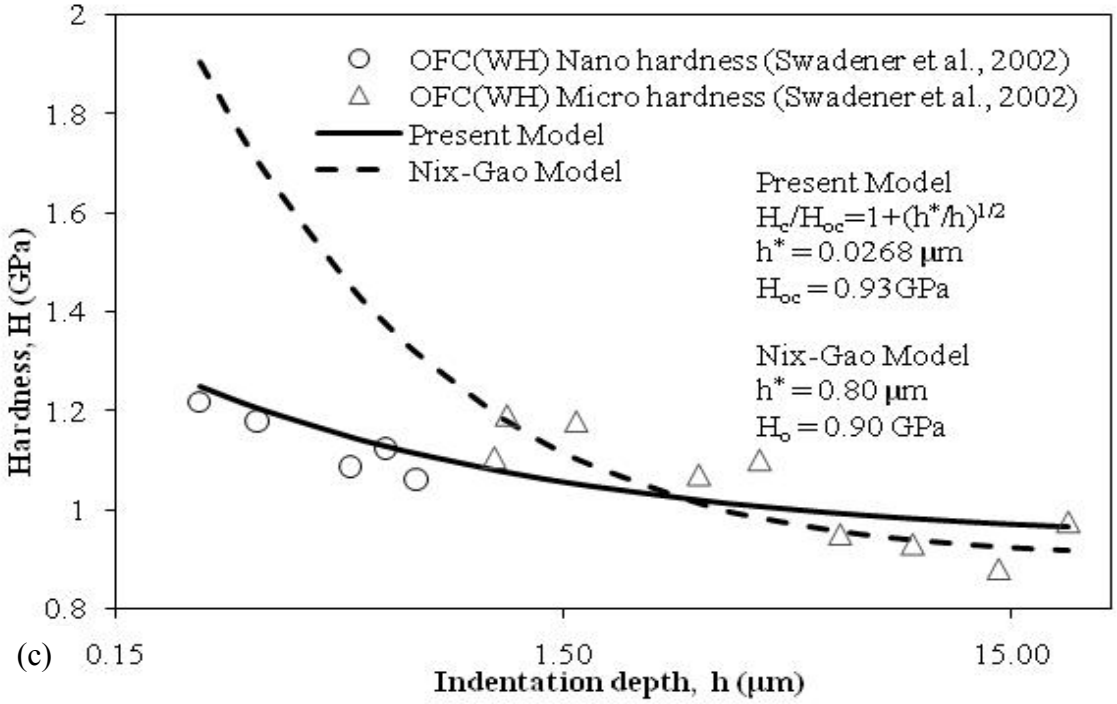

(c)

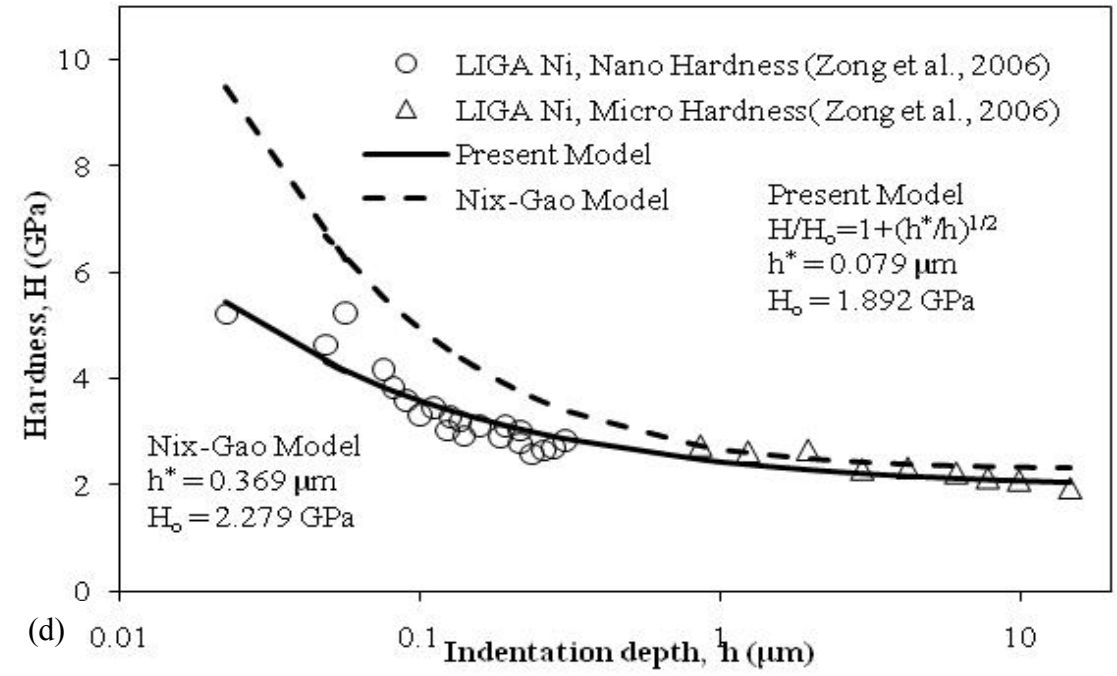

(d)

Fig. 5.2 (continued)

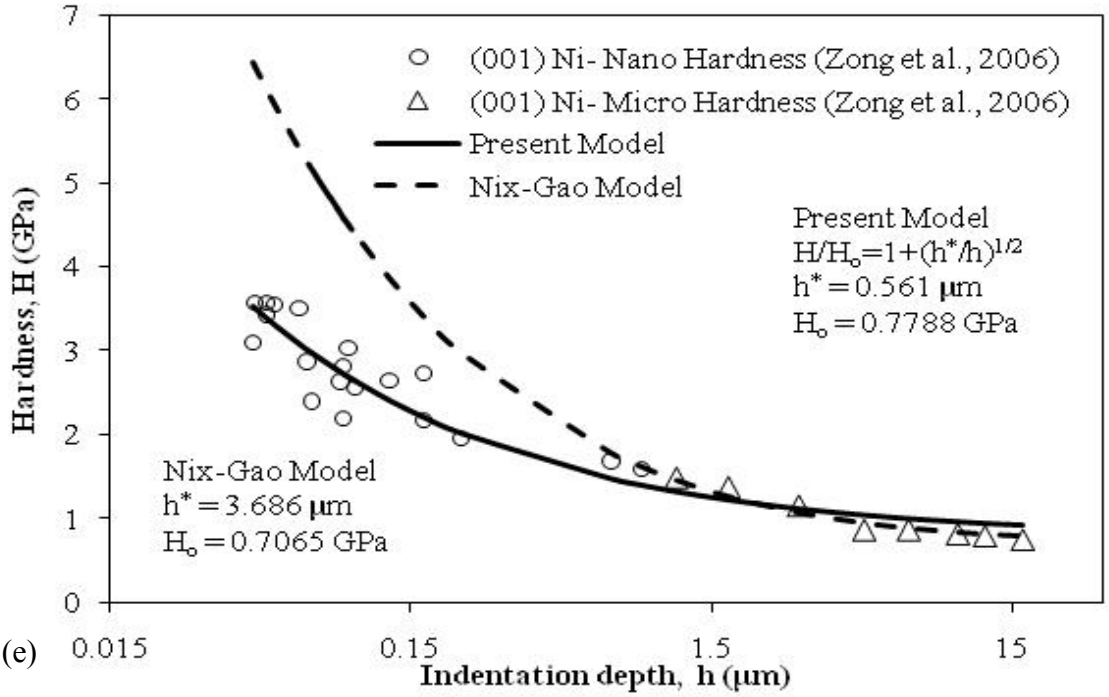

(e)

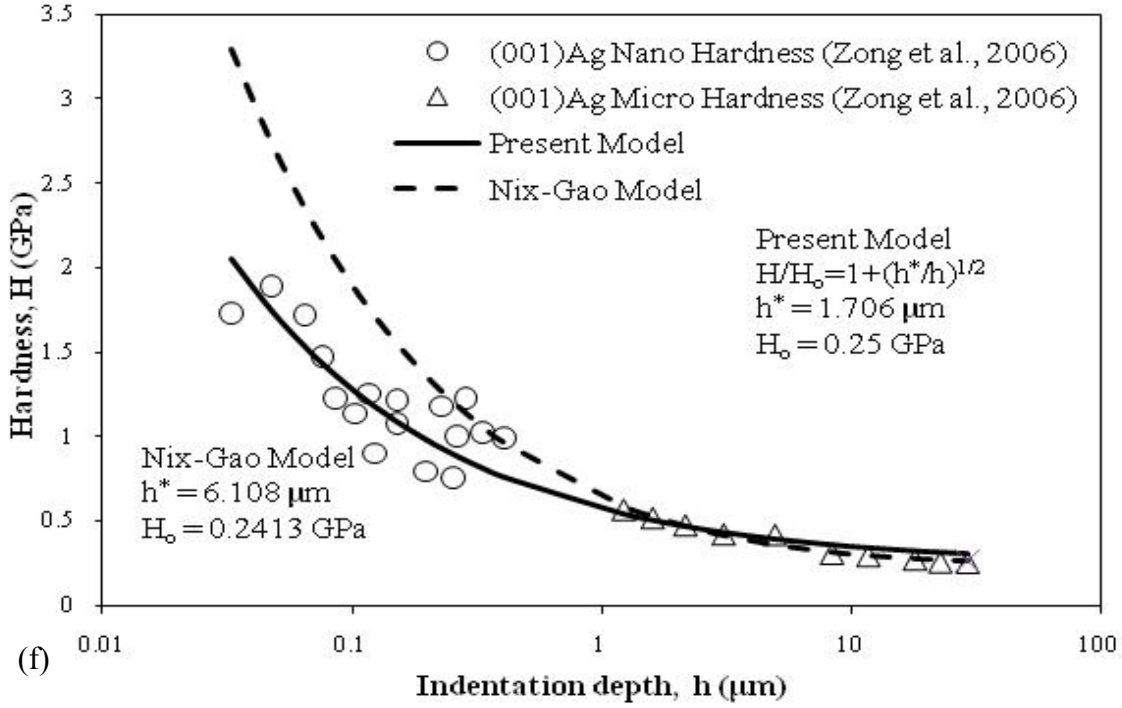

(f)

Fig. 5.2 (continued)

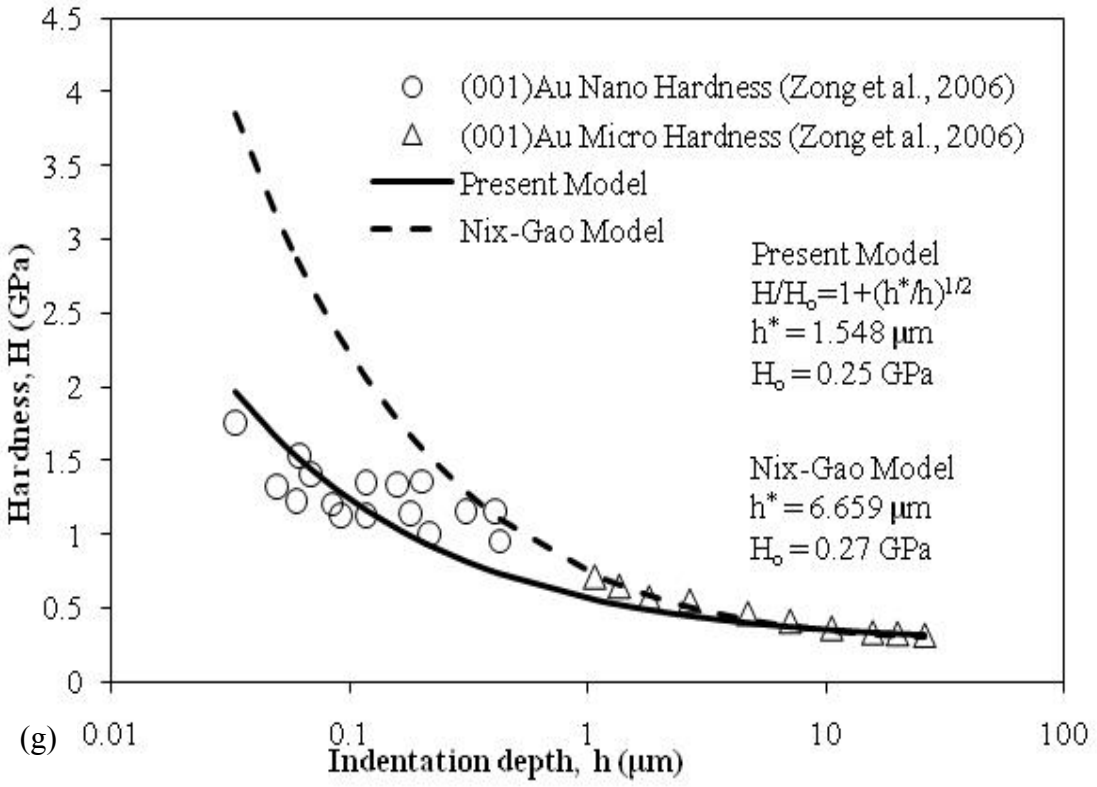

(g)

Fig. 5.2 (continued)

the macro-hardness value H_o.

A summary of the values for H_{oc} and h^* used to fit the experimental results by the present ISE model in Eq. (4.26) is shown in Table 5.1 along with different parameters of interest obtained from the plotting. The dimensionless parameter $\zeta = 0.633$, which is used to estimate the material length scale parameter, ℓ, is calculated from Eq. $(4.27)_2$ by assuming that $c = 0.2$ [corresponds to 7% effective plastic strain as

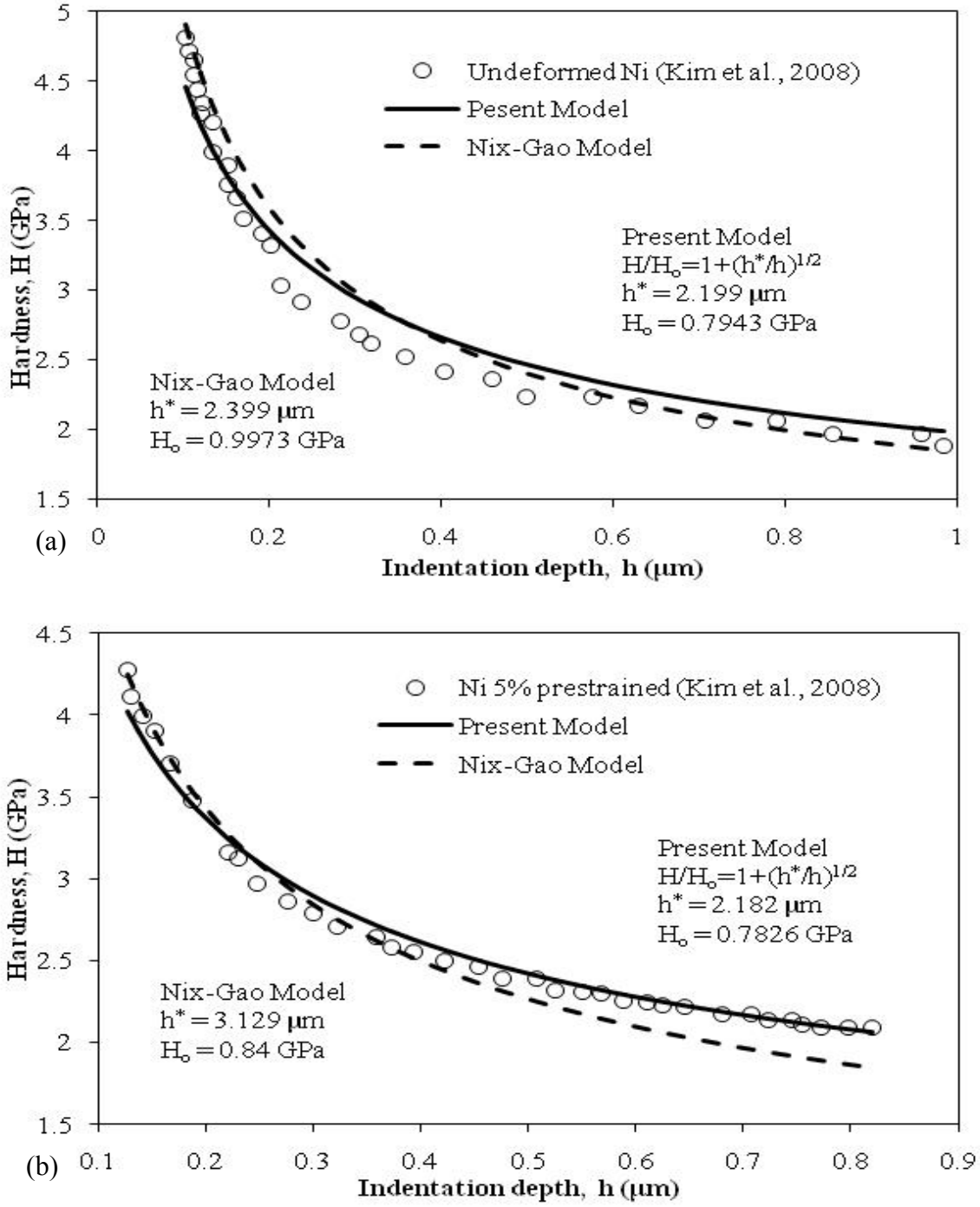

Fig. 5.3. Comparison of fit of the proposed model and Nix-Gao model to the experimental nano-hardness data: (a) Undeformed Ni, (b) 5% prestrained Ni, (c) 10% prestrained Ni, (d) 15% prestrained Ni,, (e) Undeformed SCM21, (f) 2% prestrained SCM21, (g) 5% prestrained SCM21

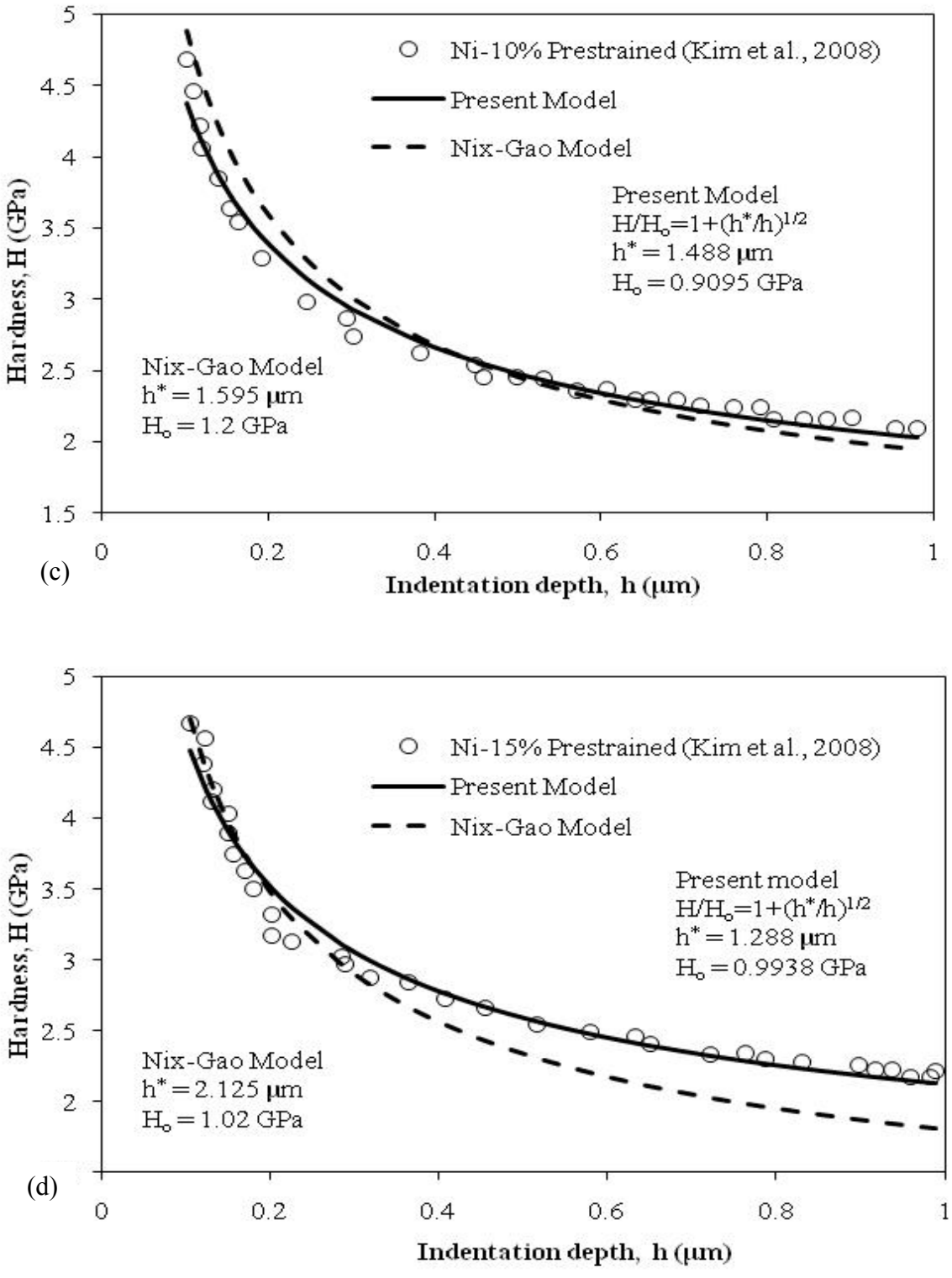

Fig. 5.3 (continued)

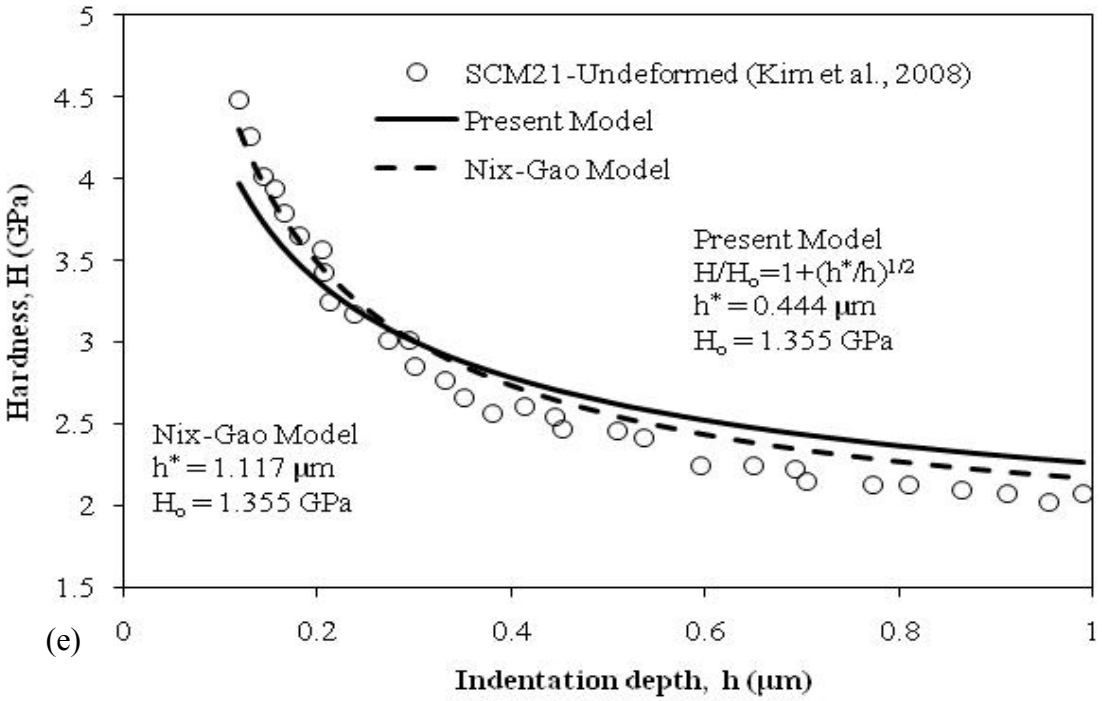

(e)

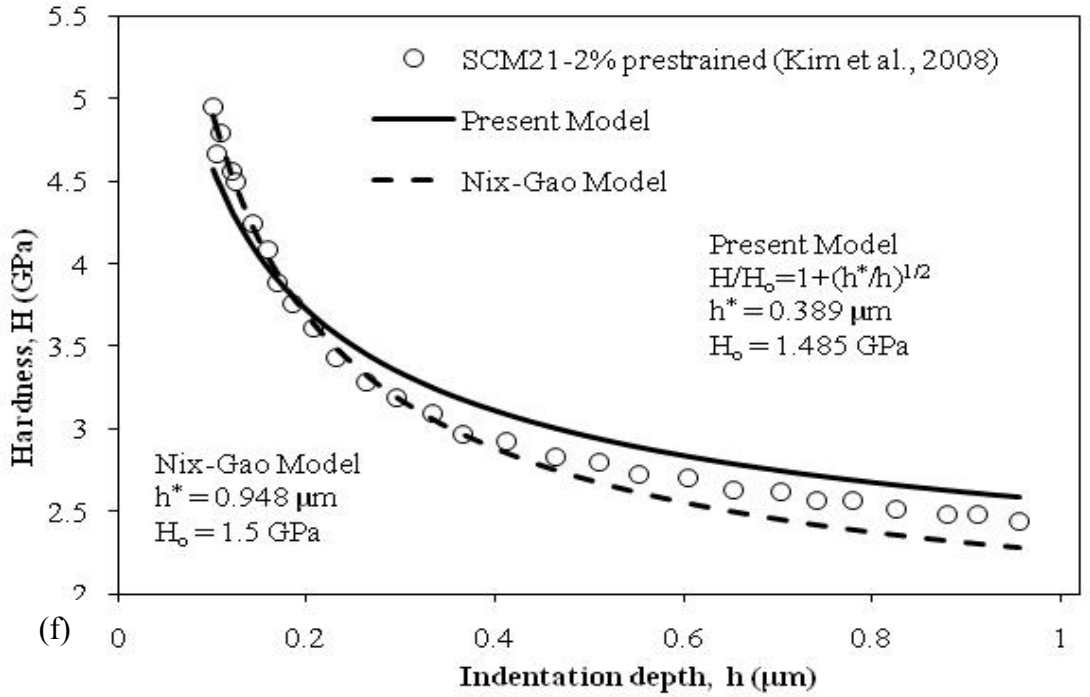

(f)

Fig. 5.3 (continued)

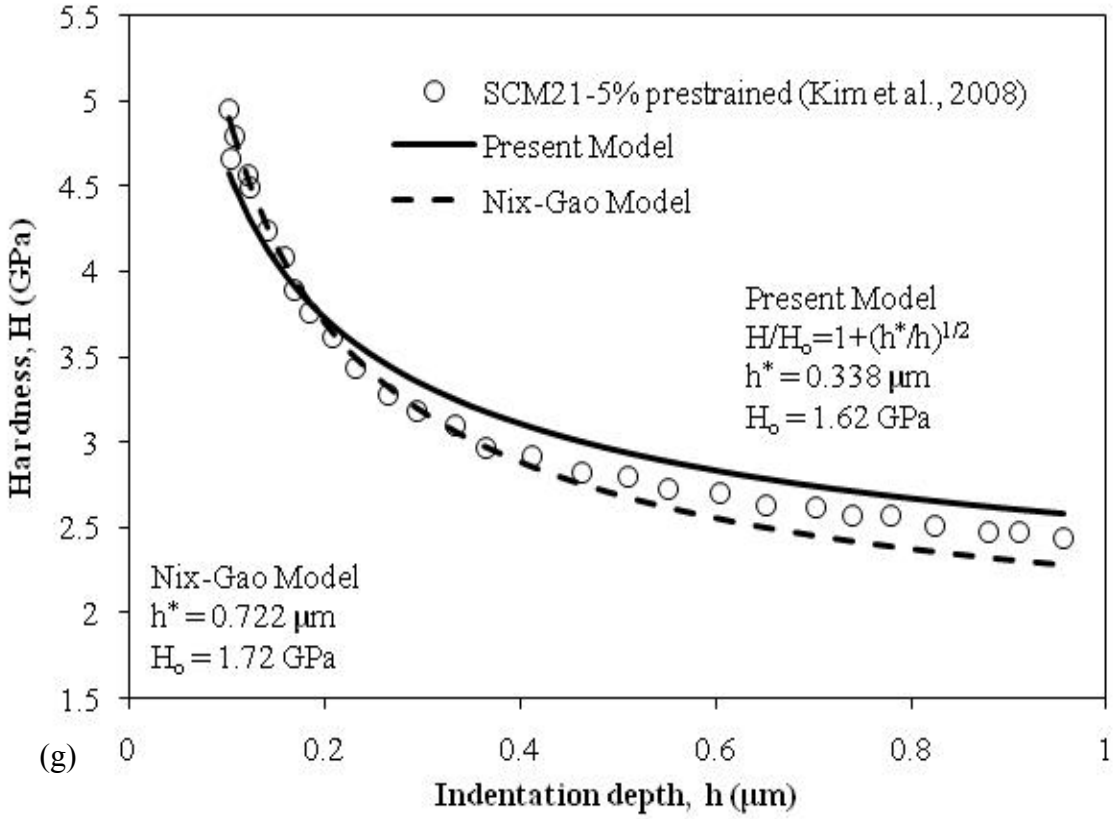

(g)

Fig. 5.3 (continued)

reported by Johnson (1970) when using pyramidal indentation], the Nye factor $\bar{r} = 2$ (Arsenlis and Park, 1999), the plastic zone ratio $f = 2.12$ as argued at the end of Section 4.4.1, and $\tan\theta = 0.358$. The calculation of ℓ, therefore, strongly depends on the values of the material parameters c, $\bar{r}$, and f.

However, one important observation from Figures 5.3 and Table 5.1 is the decrease in the length scale, ℓ with increasing pre-straining of the material. This effect is better shown in Figure 5.4(a) (undeformed and pre-strained Ni) and Figure 5.4(b) (undeformed and pre-strained SCM21). Therefore, the value for the material length scale is not fixed or constant for a specific material but depends on the course of deformation

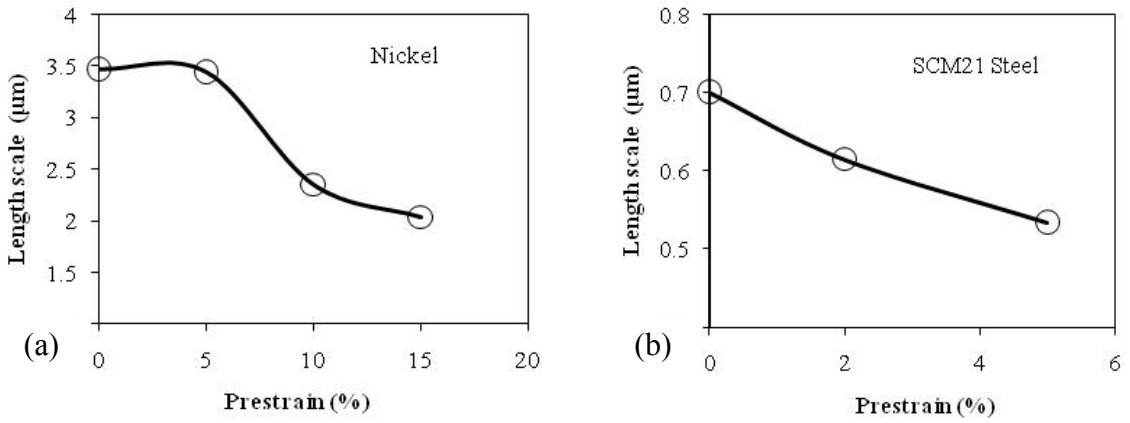

Fig. 5.4. Variation of the length scale parameter value with the level of prestraining for (a) Nickel and (b) SCM21 steel specimens of Kim et al. (2008)

and should be considered as an internal variable. This agrees very well with the physical interpretation for ℓ as presented in Eq. $(4.11)_1$ which states that the material length scale in metals is related to average spacing between dislocations. Indeed, as the level of pre-straining increases, as more dislocations are generated in the microstructure of the material, and as the average spacing between dislocations decreases. Similar arguments have been presented in Abu Al-Rub and Voyiadjis (2004a, 2004b), Voyiadjis and Abu Al-Rub (2005), and Abu Al-Rub (2007) who stated that the length scale parameter is not

fixed but decrease as the plastic strain increases. The results in Table 5.1 confirm their conclusion.

It is noteworthy that the last column in Table 5.1 presents the ISE index as

Table 5.1 The parameters of the present ISE model, Eq. (4.26), and the calculation of the length scale parameter ℓ, Eq. (4.27), from the fitted hardness data.

Material	H_0 (GPa)	h* (μm)	ζ	ℓ=h*/ ζ (μm)	ISE
Annealed Ir	2.6 (2.6)	0.26 (1.85)	0.633	0.411	1.612
Annealed OFC	0.45 (0.5)	0.576 (2.5)	0.633	0.91	2.4
Work Hardened OFC	0.93 (0.9)	0.0268 (0.8)	0.633	0.042	0.517
LIGA Ni	1.892 (2.279)	0.079 (0.369)	0.633	0.125	0.869
(001) Ni	0.7788 (0.7065)	0.561 (3.686)	0.633	0.886	2.368
(001) Ag	0.25 (0.2413)	1.706 (6.108)	0.633	2.695	4.13
(001) Au	0.25 (0.27)	1.548 (6.659)	0.633	2.445	3.934
Undeformed Ni	0.7943 (0.9973)	2.199 (2.399)	0.633	3.474	4.689
5% Prestrained Ni	0.7826 (0.84)	2.182 (3.129)	0.633	3.447	4.671
10% Prestrained Ni	0.9095 (1.20)	1.488 (1.595)	0.633	2.351	3.857
15% Prestrained Ni	0.9938 (1.02)	1.288 (2.125)	0.633	2.035	3.589
Undeformed SCM21	1.355 (1.355)	0.444 (1.117)	0.633	0.701	2.107
2%Prestrained SCM21	1.485 (1.50)	0.389 (0.948)	0.633	0.615	1.972
5%Prestrained SCM21	1.62 (1.72)	0.338 (0.722)	0.633	0.534	1.838

defined by Abu Al-Rub (2007) such that $\text{ISE} = (H_{0.1} - H_o)/H_o$, where $H_{0.1}$ is the extrapolated nano-hardness at $h = 0.1\mu\text{m}$. This index represents the increase in hardness as compared to the hardness at very large indentation depths (i.e. macro-hardness). A larger value of the ISE index indicates a higher indentation size effect (ISE) and, therefore, it can be used to compare the level of size effect in different materials. Accordingly, it is noticed that the undeformed Ni has the largest ISE and the largest material length scale, followed by 5% prestrained Ni. Thus, it can be generally concluded by comparing the values of the ISE index and the material length scales ℓ in Table 5.1 that the ISE increases as ℓ increases. Moreover, from the results for undeformed and prestrained Ni and SCM21, one can notice that the level of size effect decreases as the prestrain level increases (or generally as the course of deformation increases).Also, from Figure 5.3 and Table 5.1, it is noticed that the ISE is more pronounced in initially undeformed materials whereas the effect gradually reduces if the specimen is pre-strained. As in case of Nickel, the length scale ℓ reduces from $3.474\,\mu\text{m}$ for undeformed specimen to $2.035\,\mu\text{m}$ for the 15% pre-strained specimen and at the same time the ISE index reduces from 4.689 to 3.589 in respective specimens. Similar observation is made in case of structural steel, SCM21, where 2% and 5% pre-strained specimens are examined alongside an undeformed one. As discussed above, this can be correlated to the change in the intrinsic material length scale due to the increased initial dislocation density as can be speculated from the physical nature of the length scale being in the order of spacing between dislocations, Eq. (4.11). The spacing between dislocations is reduced due to the pre-

straining and therefore smaller material length scale and lower ISE is expected, which is confirmed by the experimental results in Figures 5.3(a-d) and 5.3(e-g).

Moreover, it can be seen from the values of h^* in Table 5.1 that when using Eq. (4.26) for fitting the micro- and nano-indentation hardness data, smaller values for the material length scale parameter are identified than that obtained by the Nix-Gao model. Therefore, it can be concluded that the Nix-Gao model overestimates the length scale parameter whereas the values from the present model are in the order of the spacing between dislocations, which is more physically sound as suggested by Eq. $(4.11)_1$.

5.3 Data from Indentation Tests with Spherical indenters

In this section, comparisons are made between the predictions of the present ISE model in Eq. (4.44) and that of Swadener et al. (2002) in Eq. (4.46) with several micro-indentation data from the literature. Unfortunately, all the spherical indentation tests reported in the available literatures have been performed in the micro-indentation level. The experimental data reported by Swadener et al. (2002) on annealed iridium, by Lim et al. (1998) on annealed and work hardened oxygen free copper and by Spary et al. (2006) on annealed nickel at different ratios of $\omega = a_p / D_p$ (or equivalently at different plastic strain levels) are utilized here to conduct this comparison. The values of D_p were not reported in these experiment, but is assumed here to be $1.1\,D$ (Swadener et al., 2002). The experimental hardness data obtained from micro-indentations are plotted in Figs. 5.5(a-m) as the hardness H versus the indentation diameter D_p at specific $\omega = a_p / D_p$ ratio. It can be seen from these figures that both the proposed model and

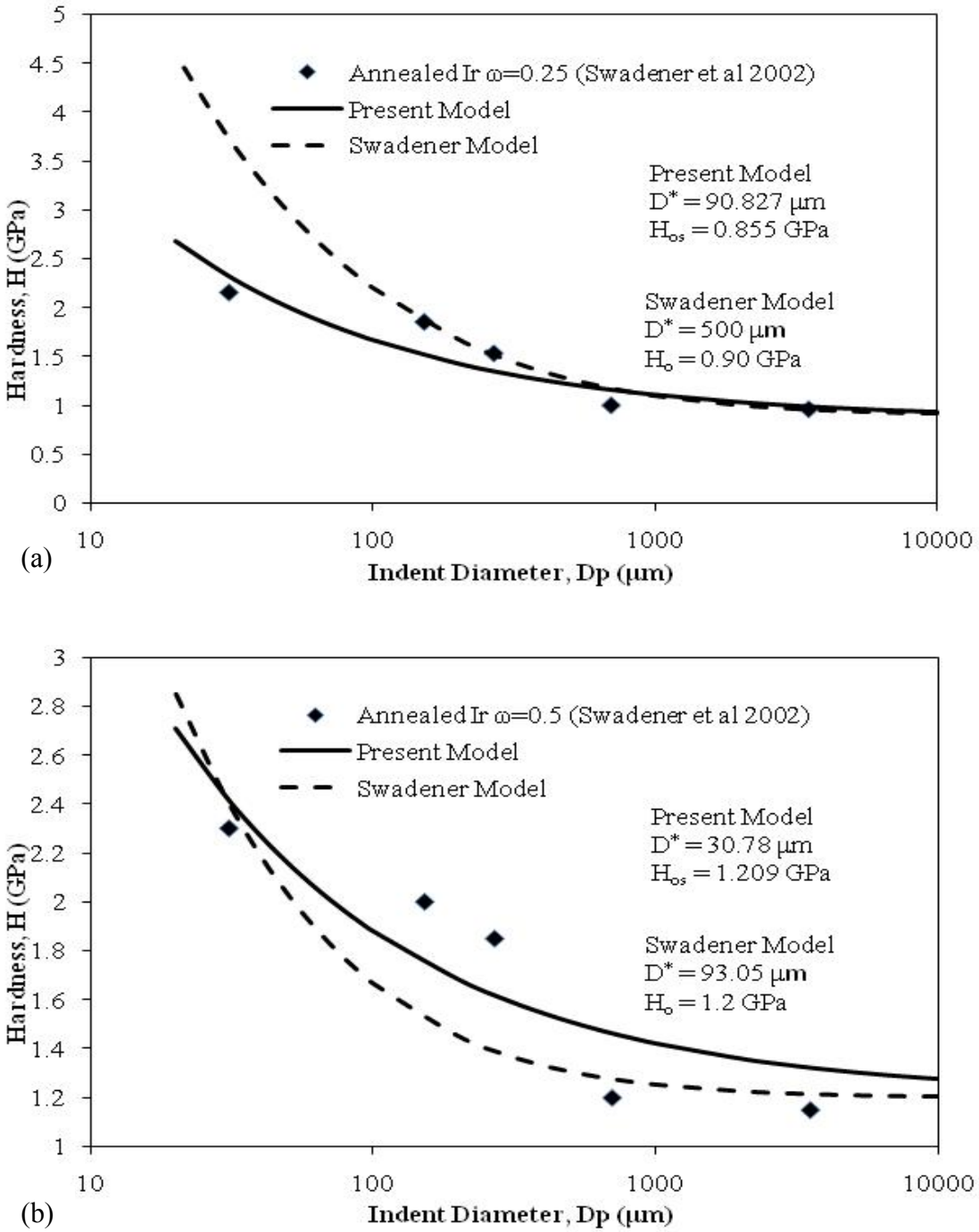

Fig. 5.5. Comparison of fit of the proposed model and Swadener et al. (2002) model to the experimental data: (a-c) Annealed Ir, (d-f) annealed Ni, (g-i) annealed OFC, (j-m) work hardened OFC at different ω values. The associated fitting parameters and ω values are listed in the figures

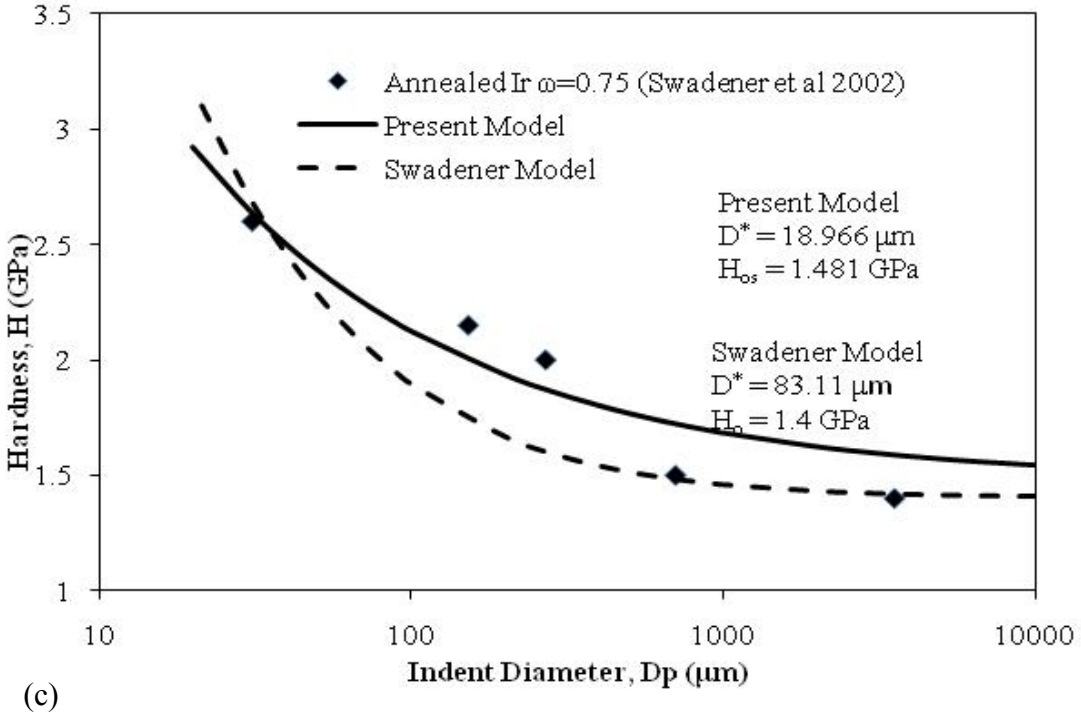

(c)

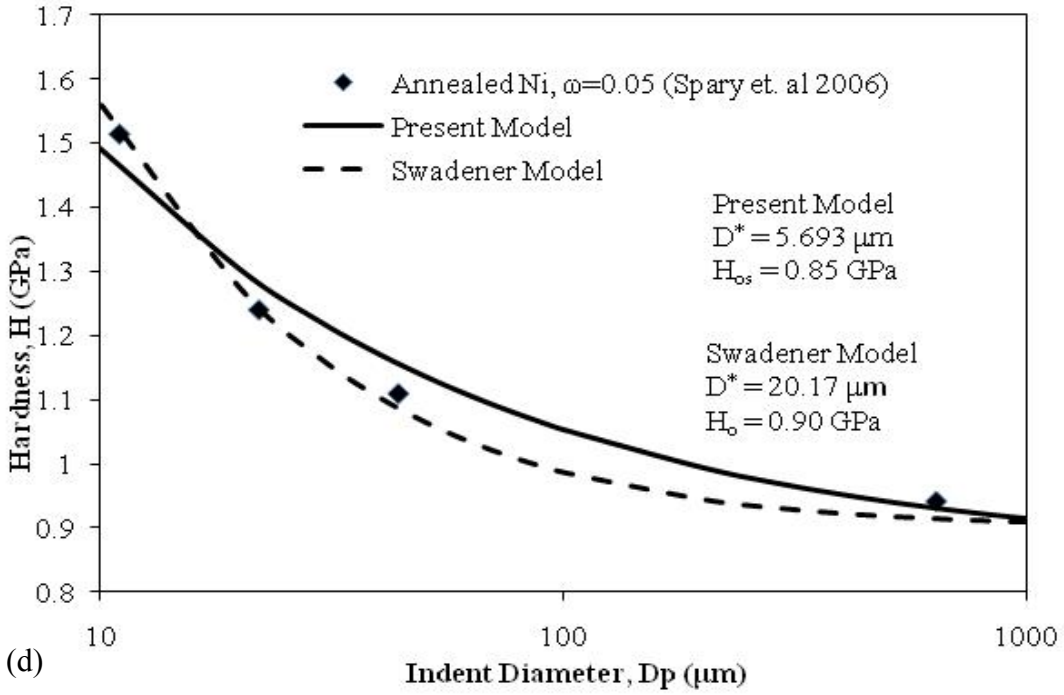

(d)

Fig. 5.5 (continued)

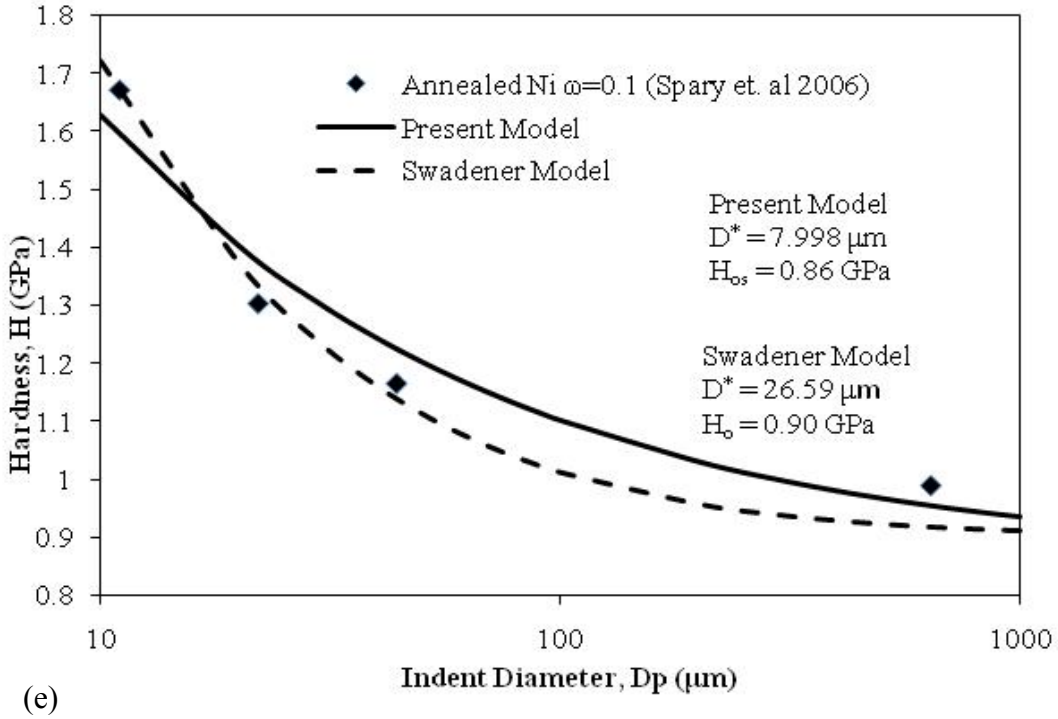

(e)

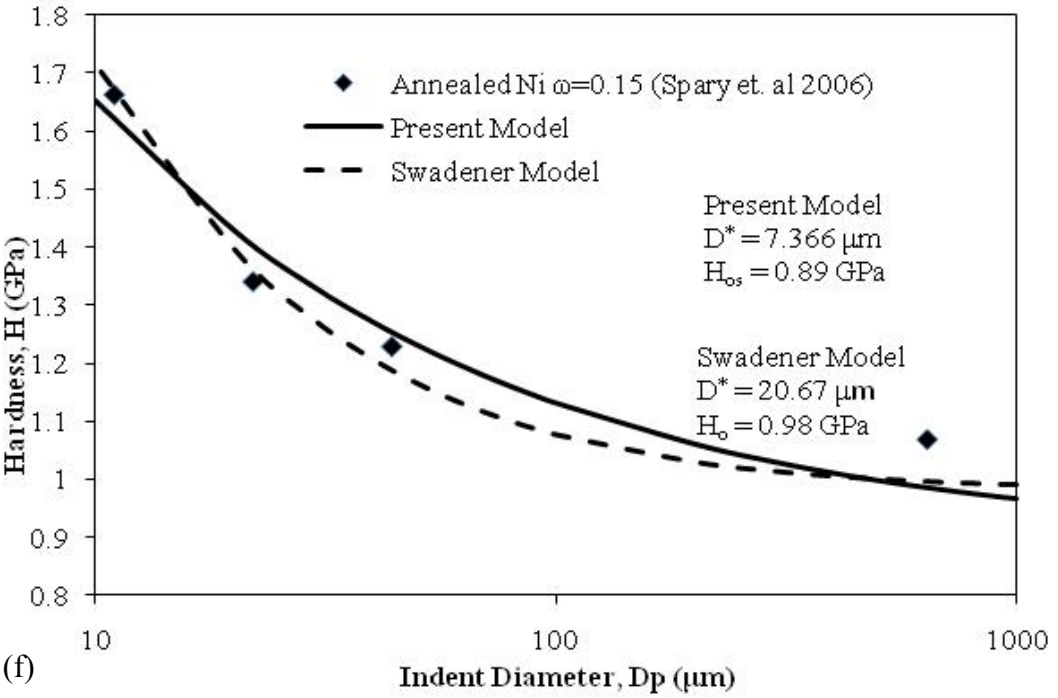

(f)

Fig. 5.5 (continued)

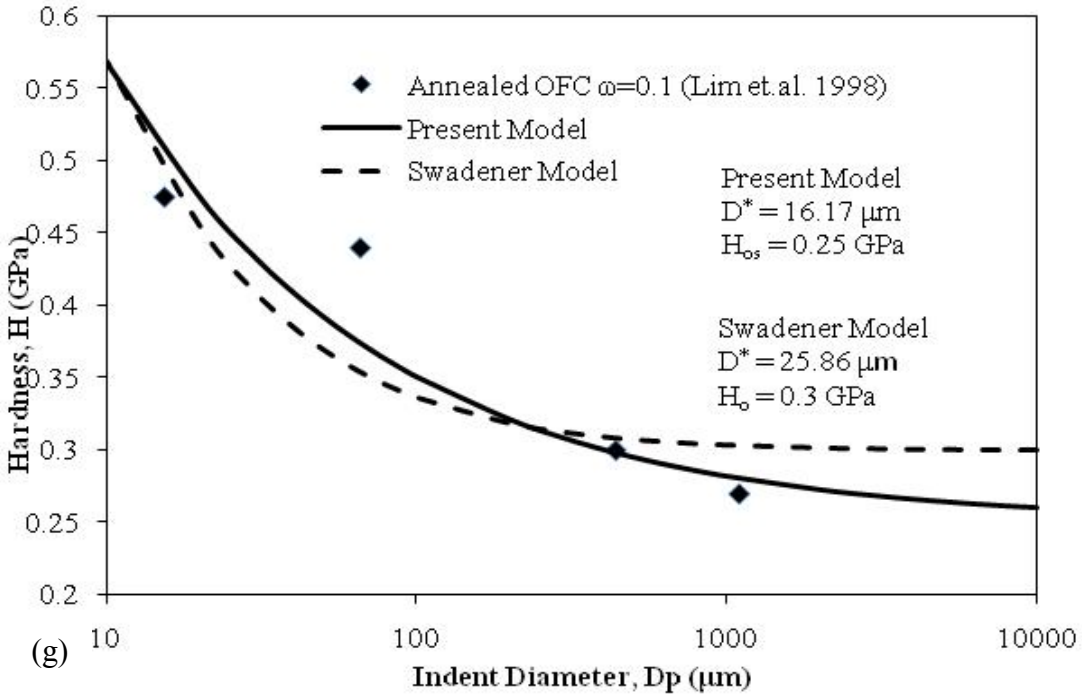

(g)

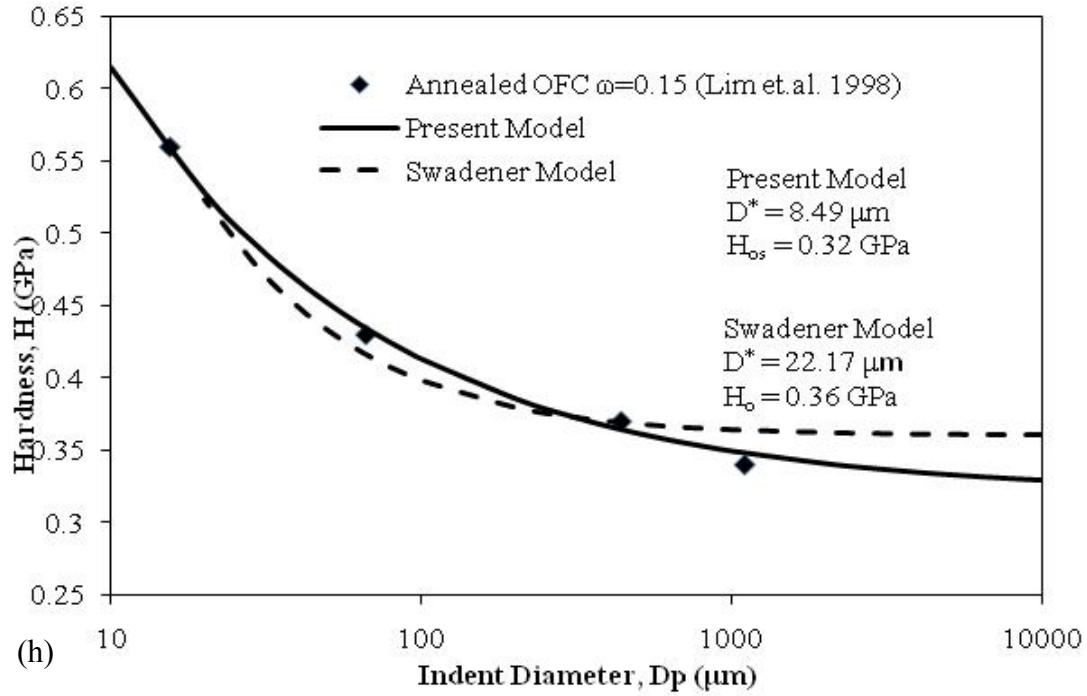

(h)

Fig. 5.5 (continued)

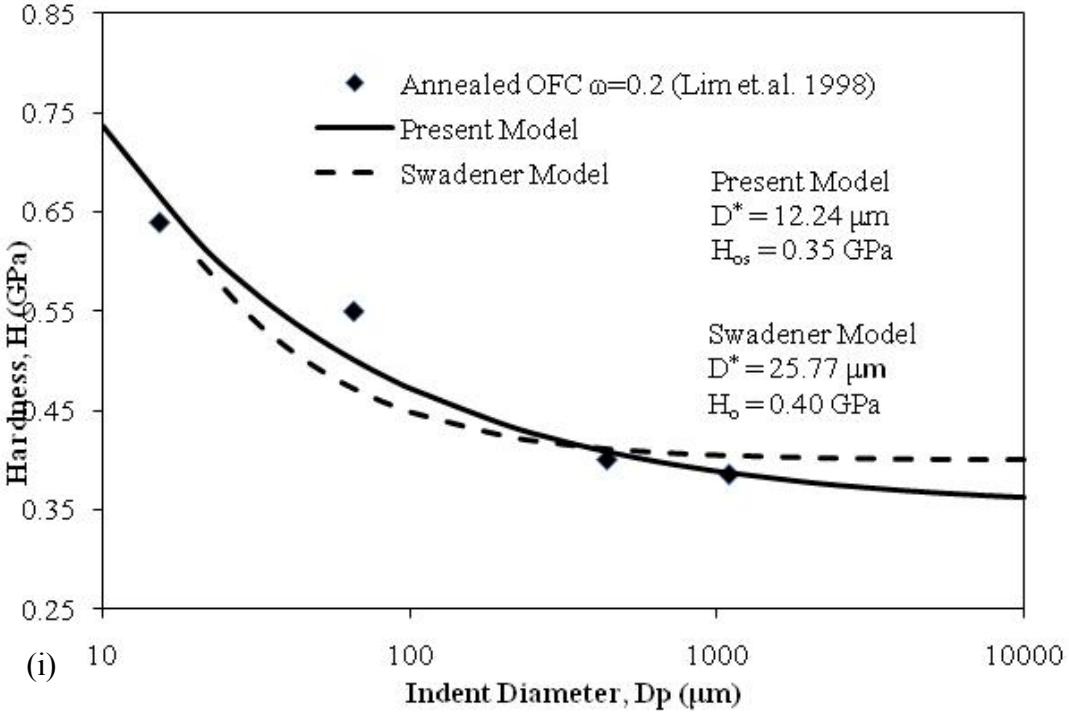

(i)

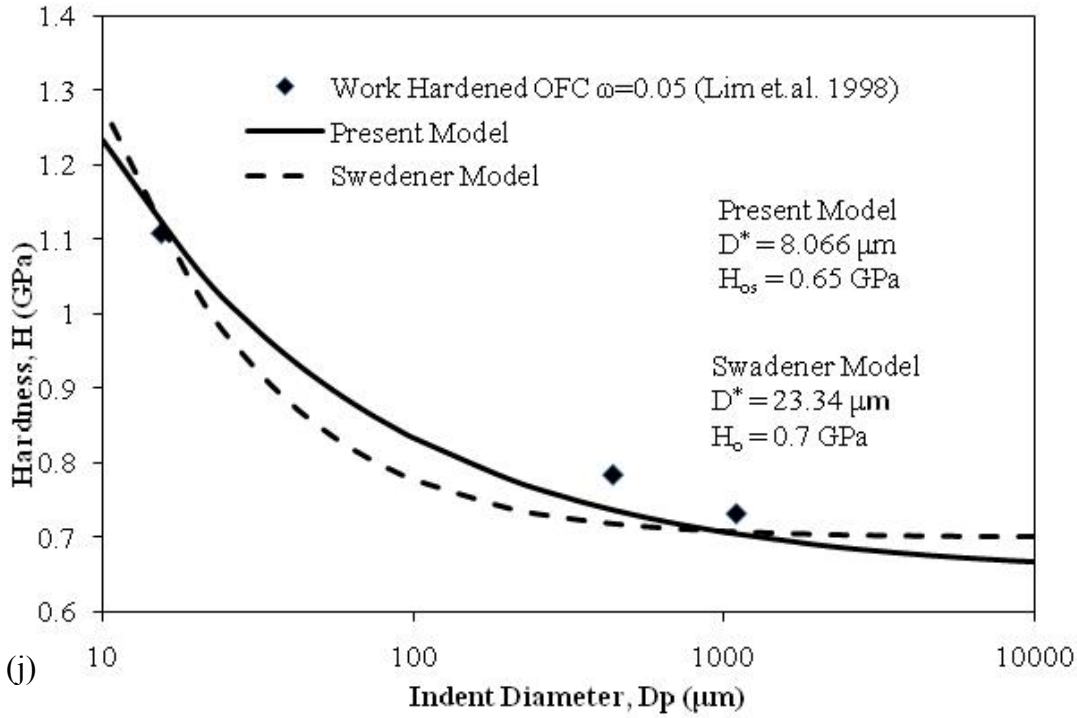

(j)

Fig. 5.5 (continued)

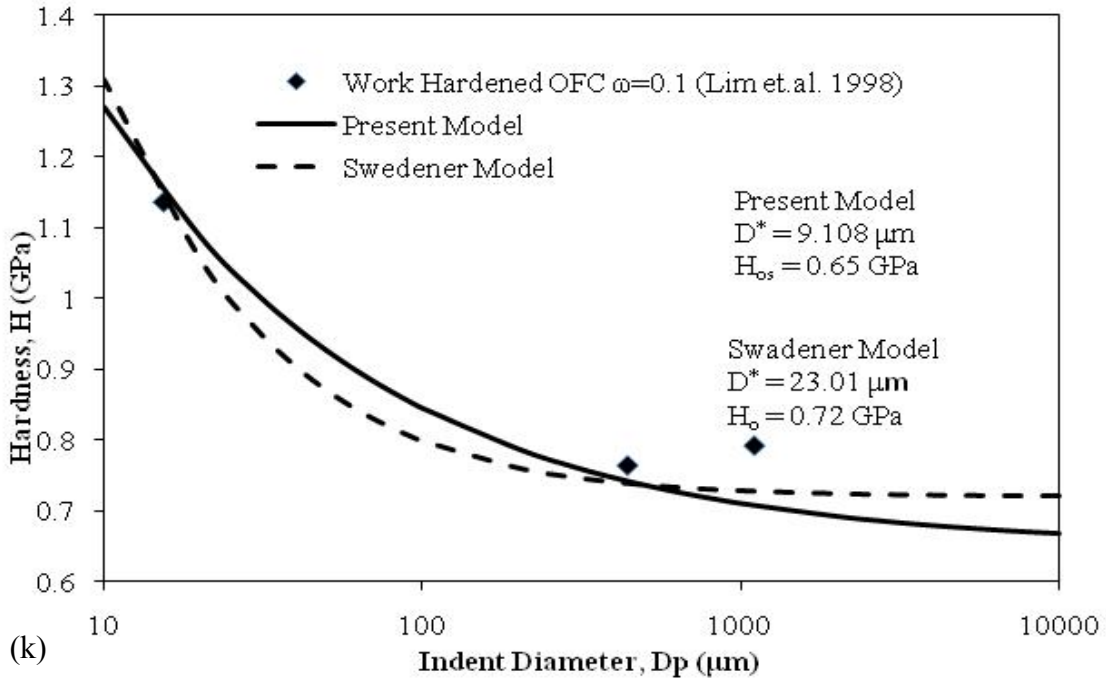

(k)

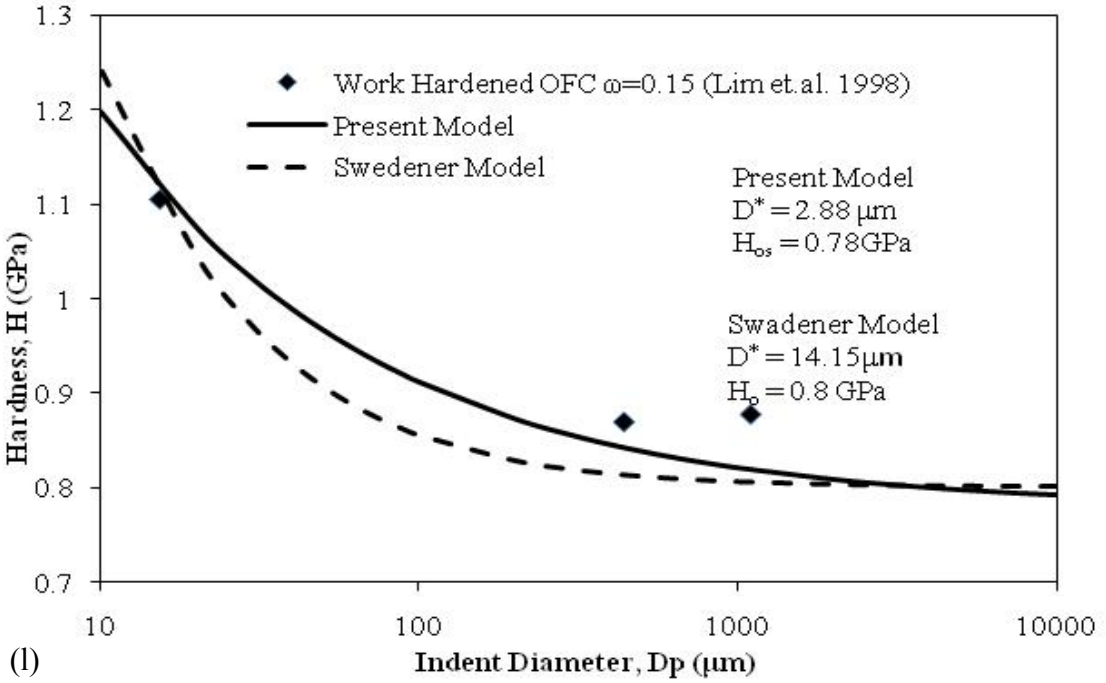

(l)

Fig. 5.5 (continued)

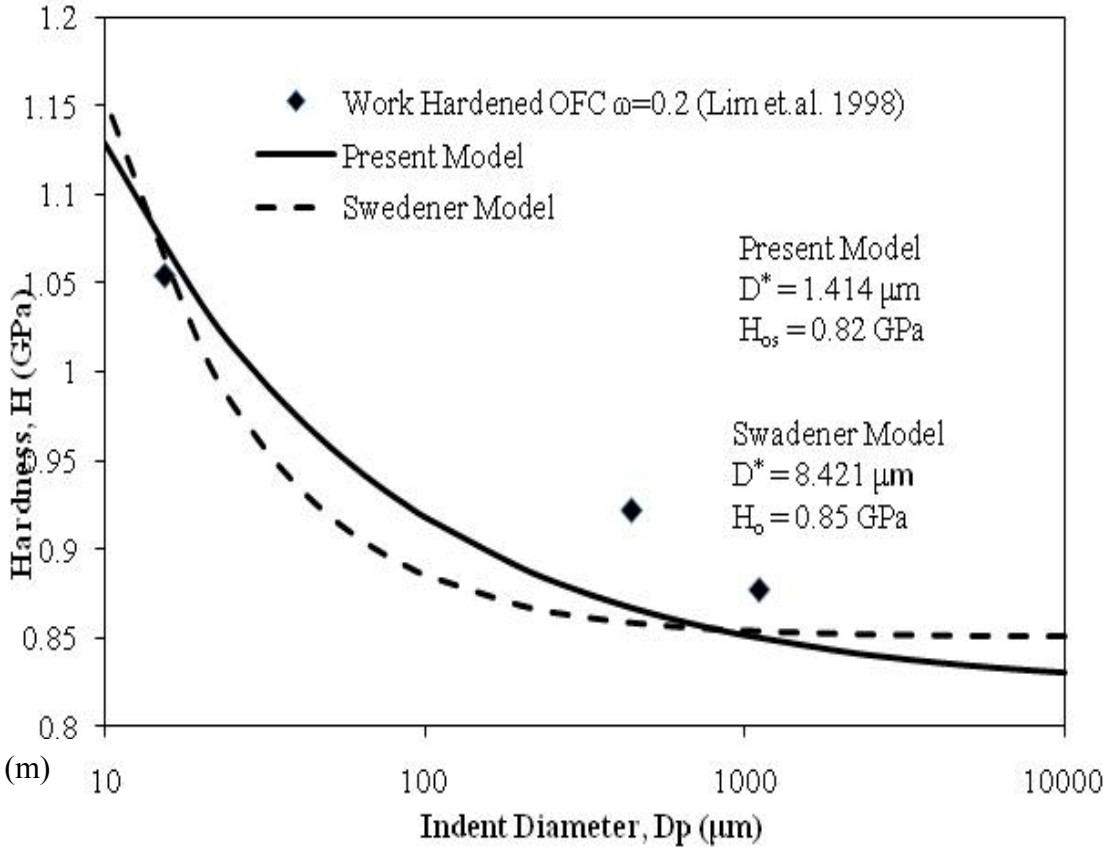

Fig. 5.5 (continued)

Swadener et al.'s model fit well the micro-indentation hardness data. However, it can be seen that Swadener et al's model tends to overestimate the hardness data at low indentation depths (i.e. as the indentation depths are getting closer to the nano range). This is most apparent in the fittings of annealed iridium data in Fig. 5.5(a), where the present model fits well the hardness data at both high and low indentations, whereas the Swadener et al.'s model overestimates the micro-hardness at low indentation diameters. Therefore, it will be interesting to compare the predictions of both models against nano-hardness data, which is the focus of a future study. Moreover, one can notice from the

comparisons in Figures 5.5(a-m) that the ISE from the present model does not progressively vanish as fast as that of Swadener et al.'s model. The characteristic form for the ISE presented by Eq. (4.44) gives a straight line when the hardness data are plotted as H/H_o versus $1/\sqrt{D_p}$, the intercept of which is 1.0 and the slope is $\sqrt{D^*}$.

Table 5.2 The parameters of the present ISE model and the calculation of the length scale parameter ℓ from the fitted hardness data.

Material	ω	H_0 (GPa)	D* (μm)	ξ	ℓ=D*/ ξ (μm)
Annealed Ir	0.025	0.855 (0.9)*	90.827 (500)*	100.197	0.906
Annealed Ir	0.05	1.209 (1.2)	30.78 (93.05)	50.198	0.613
Annealed Ir	0.075	1.481 (1.4)	18.966 (83.11)	33.53	0.566
Annealed Ni	0.05	0.85 (0.90)	5.693 (20.17)	50.198	0.113
Annealed Ni	0.10	0.86 (0.90)	7.998 (26.59)	25.198	0.317
Annealed Ni	0.15	0.89 (0.98)	7.366 (20.67)	16.87	0.437
Annealed OFC	0.10	0.25 (0.30)	16.17 (25.86)	25.198	0.642
Annealed OFC	0.15	0.32 (0.36)	8.49 (22.17)	16.87	0.503
Annealed OFC	0.20	0.35 (0.40)	12.24 (25.77)	12.60	0.971
Work hardened OFC	0.05	0.65 (0.70)	8.066 (23.34)	50.198	0.161
Work hardened OFC	0.10	0.65 (0.72)	9.108 (23.01)	25.198	0.361
Work hardened OFC	0.15	0.78 (0.80)	2.88 (14.15)	16.87	0.171
Work hardened OFC	0.20	0.82 (0.85)	1.414 (8.44)	12.60	0.112

Taking a square of the slope of this curve gives the parameter D^* from which the material length scale ℓ can be calculated using Eq. (4.45). The macroscopic hardness H_{os} is obtained when the hardness curve reaches plateau at large indentation depths. On the other hand, Swadener et al. (2002) proposed plotting their model in Eq. (4.46) as $(H/H_o)^2$ versus $1/D_p$, which should result in a straight line with slope D^*. A summary of the fitting parameters H_{os} and D^* for specific ratios of contact radius to spherical indenter diameter, ω, is presented in Table 5.2. Also, the corresponding calculated values for the material length scale parameter ℓ are presented. The dimensionless parameter ξ in Eq. $(4.45)_2$ is calculated by assuming that $c = 0.4$, the Nye factor $\bar{r} = 2$ (Arsenlis and Parks, 1999), the plastic zone ratio $f = 2.12$, $\gamma = 1$, and ω as outlined in Table 5.2. The calculation of ℓ, therefore, strongly depends on the amount of plastic deformation as characterized by $\varepsilon^p = c\omega$. Generally, one can notice from the calculated values for ℓ in Table 5.2 that as ω increases, ℓ decreases. Therefore, one can conclude that *the material length scale is not fixed or constant for a specific material but depends on the course of deformation and should be considered as an internal variable*. This agrees very well with the physical interpretation for ℓ as presented in Eq. $(4.11)_1$ which states that the material length scale in metals is related to the average spacing between dislocations or dislocations' mean free path. Indeed, as the level of plastic deformation increases, more dislocations are generated in the microstructure of the material, and the average spacing between dislocations decreases. Similar arguments have been presented in Abu Al-Rub and Voyiadjis (2004a, 2004b), Voyiadjis and Abu Al-Rub (2005), and

Abu Al-Rub (2007) who stated that the length scale parameter is not fixed but decrease as the plastic strain increases. The results in Table 5.2 confirm their conclusion. Moreover, Abu Al-Rub and Faruk (2009) have shown that the value of ℓ strongly depends on the amount of prestraining, as for work hardened materials.

Moreover, it can be seen from the identified values of D^* in Table 5.2 that when using the present model for fitting the micro-indentation hardness data, smaller values for the material length scale parameter are identified than that obtained by the Swadener et al.'s model. Therefore, it can be concluded that Swadener et al.'s model overestimates the length scale parameter whereas the values from the present model are in the order of the spacing between dislocations, which is more physically sound as suggested by Eq. $(4.11)_1$.

CHAPTER VI

SUMMARY AND CONCLUSION

6.1 Summary

Size effects or the size dependence of material properties at various length scales is a widely encountered phenomenon in Material Science that is not successfully addressed by classical plasticity/damage theories. Studies regarding this field identified the material intrinsic length scale parameter as the key term that has been missing from the classical theories. This had led to the use of higher order gradient dependent plasticity theories, incorporating length scales, in explaining size effects which was found to be quite successful. Inspired by these works, a thermodynamically consistent higher order gradient theory is developed in this current thesis and is sub-sequently used to explain some of the widely observed size effect problems. A summary of the works done in this thesis is presented in this section.

This thesis focuses on providing deeper understanding of the dependence of mechanical response on the structural size (i.e. the problem of size effects). An enhanced gradient (nonlocal) plasticity theory is developed and used to study several cases of size effects through the incorporation of length scale parameter. The thermodynamic consistency of gradient-dependent plasticity constitutive relations is discussed thoroughly in this work. Incorporation of material length scales is achieved through the development of nonlocal gradient-dependent constitutive relations. The

effect of interfacial properties (yield strength and hardening) on scale dependent behavior is considered in formulating the higher order boundary conditions.

The size effect examples considered in this thesis include elastic-plastic thin film on elastic substrate under biaxial and thermal loading respectively. Analytical model for stress and plastic strain profiles across the thickness of the film is developed in both cases. Expressions for average stress and plastic strains are also determined. These models are utilized to qualitatively analyze behavior of thin films under biaxial and thermal loading by plotting stress-strain graphs and stress and plastic strain profiles across the film thickness.

It is also emphasized that the experimental determination of the material length scale for various materials is of primary importance. This thesis provides extensive effort in this direction, where the issue of size effect and the analytical and experimental identification of the material length scale are discussed. Dislocation-based indentation size effect (ISE) models are formulated for conical and spherical tipped indenters along the lines of Nix and Gao (1998) and Swadener et al. (2002). After comparing both models with a wide range of experimental results, it is shown that the models not only successfully predict ISE from both nano- and micro-indentation tests, but also provides a means to identify the material length scale parameter.

6.2 Concluding Remarks

The gradient dependent thermodynamic framework presented in Chapter II extends the classical plasticity to higher-order gradient plasticity theory. It is found that, a non-local form of the Clausius–Duhem inequality needs to be used in deriving

gradient-dependent constitutive equations. In addition to accumulated (effective) plastic strain, its gradient, $\nabla_k \varepsilon_e^p$, is also incorporated in formulating the gradient plasticity theory to account for the accumulation of the geometrically necessary dislocations. The thermodynamic conjugate force associated to $\nabla_k \varepsilon_e^p$ introduces isotropic hardening to the formulation.

The formulation of higher-order boundary conditions is very important within strain gradient plasticity theory, especially, at interfaces, grain, or phase boundaries. These additional microscopic boundary conditions are achieved by relating the microtraction stress at interfaces to an interfacial energy that depends on the plastic strain at the interface. Furthermore, by examining linear and nonlinear expressions for this interfacial energy, it is shown that an interfacial yield condition, besides the nonlocal yield condition for the bulk, can be formulated.

In context of the analysis in Chapter III, it can be said that the higher-order gradient plasticity theory when supplemented by interfacial energy effects, can qualitatively describe many features of the size effect due to GNDs, including the strengthening, the development of boundary layers, and the strain hardening. The qualitative modeling of the strengthening is explained by the interfacial yield strength, whereas the strain hardening is described by accounting for the interfacial hardening effect.

Gradient dependent theory is used in the analytical modeling of ISE in Chapter IV. The approach followed in this work is similar to those adopted by Nix-Gao (1998) and Swadener et al. (2002); however, with one fundamental difference, which is the nature

of coupling between statistically stored dislocations (SSDs) and geometrically necessary dislocations (GNDs) in the Taylor's hardening law for metals. In formulating both these aforementioned models, a gross assumption is made such that the total dislocation density is a simple arithmetic sum of SSD and GND densities, whereas in the current model a simple arithmetic sum of the Taylor's stresses from SSD and GND densities is found to be more appropriate and give the correct order of the total dislocation density in hardening metals. This fundamental difference in derivation approach results in two new ISE models that correct the impediment of the Nix-Gao's and Swadener et al.'s models in estimating the nano-hardness data such that the present ISE models can fit better both the micro- and nano-hardness data simultaneously. Therefore, one may conclude that when using the Taylor's hardening law a simple sum of flow stresses from SSDs and GNDs is more adequate than the simple sum of SSD and GND densities.

Moreover, from dislocation-based arguments it is shown that the material length scale parameter in the strain gradient plasticity theory is not fixed or constant but changes with the course of plastic deformation such that it scales with the average spacing between dislocations. This conclusion is supported by calculating the material length scale parameter from the hardness data of undeformed and prestrained specimens. These data showed that as the prestraining level increases a smaller value for the material length scale is obtained. This suggested that the material length scale should be considered as an internal variable instead of a free parameter.

Finally, it is concluded that materials with smaller length scale are harder and require greater loads in order to create the same contact area, which dictates that the

additional amount of hardening during deformation increases as the length scale increases. Thus, the hardest materials have the smallest values of material length scale. It is also concluded that the size effect is more significant in annealed and undeformed specimens than in cold-worked or prestrained or pre-deformed specimens. This implies that weaker materials exhibit higher ISE. Therefore, the ISE is expected to be influenced by both prior dislocations and the additional work hardening that occurs during indentation.

6.3 Recommendations for Future Work

From the findings of this thesis researchers might be encouraged to work on the following directions:

- Attempts can be made to enhance the gradient theory by including a backstress associated with kinematic hardening and the higher order microstress conjugate to the gradient of the plastic strain tensor in the internal virtual power expression.
- Detailed study of the temperature dependence of interfacial hardening and the interfacial yield strength can be done.
- The developed gradient plasticity theory can be used to explain other size effect problems such as, micro bending of thin beams, micro torsion of thin wires or shear loading of thin films.
- Experimental works can be done on thin biaxially or thermally loaded thin films to validate the models developed in this thesis.
- Nano-indentation tests using spherical tipped indents can be done.

REFERENCES

Abu Al-Rub, R. K., 2007. Prediction of micro and nano-indentation size effect from conical or pyramidal indentation. Mech. Mater. 39, 787-802

Abu Al-Rub, R.K., Faruk, A.N.M., 2010. Dislocation-based model for predicting size-scale effects on the micro- and nano-indentation hardness of metallic materials. Int. J. Mater. Struct. Integ. 4, 2-3.

Abu Al-Rub, R.K., Voyiadjis, G.Z., 2004a. Analytical and experimental determination of the material intrinsic length scale of strain gradient plasticity theory from micro- and nano-indentation experiments. Int. J. Plast. 20(6), 1139- 1182.

Abu Al-Rub, R.K., Voyiadjis, G.Z., 2004b. Determination of the material intrinsic length scale of gradient plasticity theory. Int. J. Multiscale Comp. Eng. 3(3), 50-74.

Aifantis, E.C., 1984. On the mmicrostructural origin of certain inelastic models. J. Eng. Mater. Tech. 106, 326-330.

Aifantis, E.C., 1999. Strain gradient interpretation of size effects. Int. J. Fract. 95, 299-314.

Aifantis, K.E., Willis, J.R., 2005. The role of interfaces in enhancing the yield strength of composites and polycrystals. J. Mech. Phys. Solids 53, 1047–1070.

Aifantis, K.E., Willis, J.R., 2006. Scale effects induced by strain-gradient plasticity and interfacial resistance in periodic and randomly heterogeneous media. Mech. Mater. 38, 702–716.

Aifantis, K.E., Soer, W.A., De Hosson, J.Th.M., Willis, J.R., 2006. Interfaces within strain gradient plasticity: theory and experiments. Acta Mater. 54, 5077–5085.

Arsenlis, A., Parks, D.M., 1999. Crystallographic aspects of geometrically- necessary and statistically-stored dislocation density. Acta Mater. 47, 1597-1611.

Ashby, M.F., 1970. The deformation of plastically non-homogenous alloys. Philos mag. 21, 399-424.

Askes, H., Sluys, L.J., 2002. Explicit and implicit gradient series in damage mechanics. Eur. J. Mech. A/Solids 21, 379-390.

Bassani, J.L., 2001. Incompatibility and a simple gradient theory of plasticity. J. Mech. Phys. Solids 49, 1983-1996.

Bazant, Z.P., Pijaudier-Cobot, G., 1988. Nonlocal continuum damage, localization instability and convergence. J. Appl. Mech. 55, 287-293.

Begley, M.R., Hutchinson, J.W., 1998. The mechanics of size-dependent indentation. J. Mech. Phys. Solids 46, 2049-2068.

Biwa, S., Storakers, B., 1995. An analysis of fully plastic Brinell indentation. J. Mech. Phys. Solids 43, 1303-1333.

Busso, E.P., Meissonnier, F.T., O'Dowd, N.P., 2000. Gradient-dependent deformation of two-phase single crystals. J. Mech. Phys. Solids 48, 2333-2361.

Chen, S.H., Wang, T.C., 2002. A new deformation theory with strain gradient effects. Int. J. Plast. 18, 971-995.

Chiu, Y.L., Ngan, A.H.W., 2002. A TEM investigation on indentation plastic zones in Ni3Al(Cr,B) single crystals. Acta Mater. 50, 2677-2691.

de Borst, R., Muhlhaus, H.-B., 1992. Gradient dependent plasticity formulation and algorithmic aspects. Int. J. Numer. Methods Eng. 35, 521–539.

Durst, K., Backes, B., Franke, O., Goken, M., 2006. Indentation size effect in metallic materials: modeling strength from pop-in to macroscopic hardness using geometrically necessary dislocations. Acta Mater. 54, 2547-2555.

Elmustafa, A.A., Stone, D.S., 2002. Indentation size effect in polycrystalline f.c.c metals. Acta Mater., 50, 3641-3650.

Eringen, A.C., Edelen, D.G.B., 1972. On non-local elasticity. Int. J. Eng. Sci., 10, 233-248.

Feng, G., Nix, W.D., 2004. Indentation size effect in MgO. Scripta Mater, 51, 599-603.

Fleck, N.A., Muller, G.M., Ashby, M.F., Hutchinson, J.W., 1994. Strain Gradient Plasticity: Theory and Experiment. Acta Metall. Mater. 42, 475-487.

Fredriksson, P., Gudmundson, P., 2005. Size-dependent yield strength of thin films. Int. J. Plast. 21, 1834–1854.

Fredriksson, P., Gudmundson, P., 2007. Modelling of the interface between a thin film and a substrate within a strain gradient plasticity framework. J. Mech. Phys. Solids 55, 939–955.

Fremond, M., Nedjar, B., 1996. Damage, gradient of damage and principle of virtual power. Int. J. Solids Struct., 33(8), 1083-1103.

Gao, H., Huang, Y., 2003. Geometrically necessary dislocation and size-dependent plasticity. Scripta Mater. 48, 113-118.

Gao, H., Huang, Y., Nix, W.D., Hutchinson, J.W., 1999. Mechanism-based strain gradient plasticity - i. theory. J. Mech. Phys. Solids 47(6), 1239- 1263.

Gao, X.-L, 2003. Strain gradient plasticity solution for an internally pressurized thick walled spherical shell of an elastic-plastic material. Mech. Res. Comm., 30 (2003), 411–420.

Gao, X.L., 2008. Analytical solution for the stress field around a hard spherical particle in a metal matrix composite incorporating size and finite volume effects. Math. Mech. Solids 13 (2008), 357–372,.

Geers, M.G.D., Peerlings, R.H.J., Brekelmans, W.A.M., de Borst, R., 2000. Phenomenological nonlocal approaches based on implicit gradient-enhanced damage. Acta Mech. 144, 1-15.

Gerberich, W.W., Tymiak, N.I., Grunlan, J.C., Horstemeyer, M.F., Baskes, M.I., 2002. Interpretation of indentation size effects. ASME Tras., J. App. Mech. 69, 433-442.

Gomez and Basaran, 2006. Nano-indentation of Pb/Sn Solder Alloys: Experimental and Finite Element Simulation Results. Int. J. Solids Struct. 43 (2006), 1505-1527.

Green, A.E., Naghdi, P.M., 1971. Some remarks on elastic–plastic deformation at finite strain. Int. J. Eng. Sci. 9, 1219–1229.

Gudmundson, P., 2004. A unified treatment of strain gradient plasticity. J. Mech. Phys. Solids 52, 1379–1406.

Gurtin, M.E., 2000. On the plasticity of single crystals: free energy, microforces, plastic-strain gradients. J. Mech. Phys. Solids 48, 989–1036.

Gurtin, M.E., 2002. A gradient theory of single-crystal viscoplasticity that accounts for geometrically necessary dislocations. J. Mech. Phys. Solids 50 (1), 5-32.

Gurtin, M.E., 2003. On a framework for small-deformation viscoplasticity: free energy, microforces, strain gradients. Int. J. Plast. 19, 47–90.

Haque, M.A., Saif, M.T.A., 2003. Strain gradient effect in nanoscale thin films. Acta Mater. 51, 3053-3061.

Huang, Y., Zhang, F., Hwang, K.C., Nix, W.D., Pharr, G.M., Feng, G., 2006. A model of size effects in nano-indentation. J. Mech. Phys. Solids 54, 1668–1686.

Huber, N., Nix, W.D., Gao, H., 2002. Identification of elastic-plastic material parameters from pyramidal indentation of thin films. Proceedings of the Royal Society of London Series A 458(2023), 1593-1620.

Johnson, K.L., 1970. The correlation of indentation experiments. J. Mech. Phys. Solids 18, 115-126.

Kim, J.Y., Kang, S.K., Greer, J.R., Kwon, D., 2008. Evaluating plastic flow properties by characterizing indentation size effect using a sharp indenter, Acta Mater. 56, 3338-3343

Kiser, M.T., Zok, F.W., Wilkinson, D.S., 1996. Plastic flow and fracture of a particulate metal matrix composite. Acta Mater. 44, 3465-3476.

Kocks, U.F., 1966. A statistical theory of flow stress and work hardening. Phil. Mag. 13, 541.

Kramer, D., Huang, H., Kriese, M., Rohack, J., Nelson, J., Wright, A., Bahr, D., Gerberich, W.W., 1999. Yield strength predictions from the plastic zone around nanocontacts. Acta Mater. 47, 333-343.

Kroner, E., 1962. Dislocations and continuum mechanics. Appl. Mech. Rev. 15, 599-606.

Kuhl, E., Ramm, E., de Borst, R., 2000. An anistropic gradient damage model for quasi-brittle materials. Comput. Methods Appl. Mech. Eng. 183, 87-103.

Lasry, D., Belytschko, T., 1988. Localization limiters in transient problems. Int. J. Solids Struct. 24, 581–597

Lim, Y.Y., Chaudhri, Y.Y., 1999. The effect of the indenter load on the nano-hardness of ductile metals: an experimental study of polycrystalline work-hardened and annealed oxygen-free copper. Philos. Mag. A, 79(12), 2979-3000.

Lloyd, D.J., 1994. Particle reinforced aluminum and magnesium matrix composites. Int. Mater. Rev. 39, 1-23.

Ma, Q., Clarke, D.R., 1995. Size dependent hardness in silver single crystals. J. Mater. Res. 10, 853-863.

Manika, I., Maniks, J., 2006. Size effects in micro- and nanoscale indentation. Acta Mater. 54, 2049-2056.

McElhaney, K.W., Valssak, J.J., Nix, W.D., 1998. Determination of indenter tip geometry and indentation contact area for depth sensing indentation experiments. J. Mater. Res. 13, 1300-1306.

Mughrabi, H., 2001. On the role of strain gradients and long-range internal stresses in the composite model of crystal plasticity. Mater. Sci. Eng. A 317, 171-180.

Mühlhaus, H.B., Aifantis, E.C.,1991. A variational principle for gradient plasticity. Int. J. Solid Struct. 28, 845-857.

Nan, C.-W., Clarke, D.R., 1996. The influence of particle size and particle fracture on the elastic/plastic deformation of metal matrix composites. Acta Mater. 44, 3801–3811.

Needleman, A., 1988. Material rate dependent and mesh sensitivity in localization problems. Comp. Methods App. Mech. Eng. 67, 68-85.

Needleman, A., Gil Sevillano, J., 2003. Preface to the viewpoint set on: geometrically necessary dislocations and size dependent plasticity. Scripta Mater. 48(2), 109-211.

Nix, W.D., Gao, H., 1998. Indentation size effects in crystalline materials: a law for strain gradient plasticity. J. Mech. Phys. Solids, 46 (3), 411-425.

Nye, J.F., 1953. Some geometrical relations in dislocated crystals. Acta Metall. 1, 153–162.

Oka, F.,Yashima, A.,Sawada, K.,Aifantis, E.C.,2000. Instability of gradient-dependent elastoviscoplastic model for clay and strain localization analysis. Comp. Methods App. Mech. Eng. 183(1), 67-86.

Oliver, W.C., Pharr, G.M., 1992. An improved technique for determining hardness and elastic modulus using load and displacement sensing indentation experiments. J. Mater. Res. 7, 1564-1583.

Orowan, E., 1948. Discussion in symposium on internal stresses in metals and alloys. Inst. Metals, London, p. 451.

Peerlings, R.H.J., de Borst, R., Brekelmans, W.A.M., de Vree, J.H.P., 1996. Gradient enhanced damage for quasi-brittle materials. Int. J. Numer. Methods Eng., Wiley, London, 39, 3391-3403.

Pijaudier-Cabot, T.G.P. Bazant, Z.P., 1987. Nonlocal damage theory. ASCE Journal of Engineering Mechanics 113, 1512-1533.

Poole, W.J., Ashby, M.F., Fleck, N.A., 1996. Micro-hardness of annealed and work-hardened copper polycrystals. Scripta Mater. 34, 559-564.

Rhee, M., Hirth, J.P., Zabib, H.M., 1994a. A superdislocation model for the strengthening of metal matrix composites and the initiation and propagation of shear bands. Acta Metall. Mater. 42, 2645–2655.

Rhee, M., Hirth, J.P., Zbib, H.M., 1994b. On the bowed out tilt wall model of flow stress and size effects in metal matrix composites. Scripta Metall. Mater. 31, 1321– 1324.

Qiu, X., Huang, Y., Nix, W.D., Hwang, K.C., Gao, H., 2001. Effect of intrinsic lattice resistance in strain gradient plasticity. Acta Mater. 49, 3949-3958.

Qu, S., Huang, Y., Nix, W.D., Jiang, H., Zhang, F., Hwang, K.C., 2004. Indenter tip radius effect on the Nix–Gao relation in micro- and nano-indentation hardness experiments. J. Mater. Res. 19, 3423–3434.

Saczuk, J., Hackl, K., Stumpf, H., 2003. Rate theory of nonlocal gradient damage-gradient viscoinelasticity. Int. J. Plast. 19, 675-706.

Saha, R., Xue, Z., Huang, Y., Nix, W.D., 2001. Indentation of a soft metal film on a hard substrate: strain gradient hardening effects. J. Mech. Phys. Solids 49, 1997-2014.

Shrotriya, P., Allameh, S.M., Lou, J., Buchheit, T., Soboyejo, W.O., 2003. On the measurement of the plasticity length scale parameter in LIGA nickel foils. Mech. Mater. 35, 233-243.

Shu, J.Y., Barrlow, C.Y., 2000. Strain gradient effects on microscopic strain field in a metal matrix composite. Int. J. Plast. 16, 563-591.

Shu, J.Y., Fleck, N.A., 1998. The prediction of a size effect in micro-indentation. Int. J. Solids Struct. 35, 1363-1383.

Shu, J.Y., Fleck, N.A., 1999. Strain gradient crystal plasticity: size dependent deformation in bicrystals. J. Mech. Phys. Solids 47, 297-324.

Spary, I.J., Bushby, A.J., Jennett, N.M., 2006. On the indentation size effect in spherical indentation. Philos. Mag. 86, 5581-5593.

Stelmashenko, N.A., Walls, M.G., Brown, L.M., Milman, Y.V., 1993. Microindentation on W and Mo oriented single crystals: an STM study. Acta Metall. Mater. 41, 2855-2865.

Stolken, J.S. Evans, A.G.,1998. A microbend test method for measuring the plasticity length-scale. Acta Mater 46, 5109-5115.

Svedberg, T., Runesson, K., 2000. An adaptive finite element algorithm for gradient theory of plasticity with coupling to damage. Int. J. Solids Struct. 37, 7481-7499.

Swadener, J.G., George, E.P., Pharr, G.M., 2002. The correlation of the indentation size effect measured with indenters of various shapes. J. Mech. Phys. Solids 50, 681-694.

Tabor, D., 1951. The hardness of metals. Clarendon Press, Oxford.

Taylor, G.I., 1938. Plastic strain in metals. J. Inst. Metals 62, 307-324.

Tsagrakis, I., Aifantis, E.C., 2002. Recent developments in gradient plasticity-part i: formulation and size effects. ASME Trans., J. Eng. Mat. Tech. 124, 352-357.

Voyiadjis, G.Z., Abu Al-Rub, R.K., 2002. Determination of the material intrinsic length scale of gradient plasticity theory. In: The MACSI Symposium on Parameter Identification in Structural and Materials Engineering, Milano, Italy.

Voyiadjis, G.Z., Abu Al-Rub, R.K., 2005. Gradient plasticity theory with a variable length scale parameter. Int. J. Solids Struct. 42, 3998-4029.

Voyiadjis, G.Z., Abu Al-Rub, R.K., 2009. Nonlocal continuum damage and plasticity: theory and computation, World Scientific Publishing Co Pte Ltd., London, UK.

Voyiadjis, G.Z., Deliktas, B., Aifantis, E.C., 2001. Multiscale analysis of multiple damage mechanics coupled with inelastic behavior of composite materials. J. Eng. Mech. 127(7), 636-645.

Voyiadjis, G.Z., Dorgan, R.J., 2001. Gradient formulation in coupled damage- plasticity. Arc. Mech. 53(4-5), 565-597.

Wang, W.M., Askes, H., Sluys, L.J., 1998. Gradient viscoplastic modeling of material instabilities in metals. Metals Mater.—Korea 4 (3), 537–542.

Wang, W.M., Sluys, L.J., de Borst, R., 1996. Interaction between material length scale and imperfection size for localization phenomena in viscoplastic media. Eur. J. Mech. A/Solids 15(3), 447-464.

Xue, Z., Huang, Y., Hwang, K.C., Li, M., 2002. The influence of indenter tip radius on the micro-indentation hardness. ASME J. Eng. Mater. Tech. 124, 371-379

Yuan, H., Chen, J., 2001. Identification of the intrinsic material length in gradient plasticity theory from micro-indentation tests. Int. J. Solids Struct. 38, 8171-8187.

Zbib, H.M., Aifantis, E.C., 1992. On the gradient-dependent theory of plasticity and shear banding. Acta Mech. 92, 209-225.

Zhang, F., Saha, R., Huang, Y., Nix, W. D., Hwang, K.C., Qu, S., Li, M., 2005. Indentation of a hard film on a soft substrate: strain gradient hardening effects. Int. J. Plast. 23, 25-43

Zhao, M., Slaughter, W.S., Li, M., Mao, S.X., 2003. Material-length-scale-controlled nano-indentation size effects due to strain-gradient plasticity. Acta Mater. 51, 4461–4469.

Zhu, H.T., Zbib, H.M.,1995. Flow strength and size effect of an al–si–mg composite model system under multiaxial loading. Scripta Metall. Mater. 32, 1895–1902.

Zhu, H.T., Zbib, H.M., Aifantis, E.C., 1997. Strain gradients and continuum modeling of size effect in metal matrix composites. Acta Mech. 121, 165–176.

Zong, Z., Lou, J., Adewoye, O.O., Elmustafa, A.A., Hammad, F., Soboyejo, W.O., 2006. Indentation size effect in the nano- and micro-hardness of fcc single crystal metals. Metar. Sci. Eng. A 434, 178-187

VITA

Name: Abu Nayeem Md. Faruk

C/O: Dr. Rashid K. Abu Al-Rub
Department of Civil Engineering
Texas A&M University
College Station, TX-77843-3136

Email Address: nayeem.email@gmail.com

Education: B.Sc., Civil Engineering, Bangladesh University of Engineering & Technology, 2007